



**Michigan
Technological
University**

Michigan Technological University
Digital Commons @ Michigan Tech

Dissertations, Master's Theses and Master's Reports

2018

Controlling light with metadevices

Xu Zhang

Michigan Technological University, xzhang22@mtu.edu

Copyright 2018 Xu Zhang

Recommended Citation

Zhang, Xu, "Controlling light with metadevices", Open Access Dissertation, Michigan Technological University, 2018.

<https://doi.org/10.37099/mtu.dc.etr/700>

Follow this and additional works at: <https://digitalcommons.mtu.edu/etr>



Part of the [Electromagnetics and Photonics Commons](#)

CONTROLLING LIGHT WITH METADEVICES

By

Xu Zhang

A DISSERTATION

Submitted in partial fulfillment of the requirements for the degree of

DOCTOR OF PHILOSOPHY

In Electrical Engineering

MICHIGAN TECHNOLOGICAL UNIVERSITY

2018

© 2018 Xu Zhang

This dissertation has been approved in partial fulfillment of the requirements for the Degree of DOCTOR OF PHILOSOPHY in Electrical Engineering.

Department of Electrical and Computer Engineering

Dissertation Advisor: *Dr. Durdu Guney*

Committee Member: *Dr. Elena Semouchkina*

Committee Member: *Dr. Christopher T. Middlebrook*

Committee Member: *Dr. Ramy EI-Ganainy*

Department Chair: *Dr. Daniel R. Fuhrmann*

Contents

List of Figures	ix
List of Tables	xxi
Preface	xxiii
Acknowledgments	xxv
Abstract	xxvii
1 Overview	1
1.1 Background	1
1.2 Problem statement	4
1.3 Research objectives	10
2 Towards 3D bulk photonic metamaterials	17
2.1 Introduction	17
2.2 Direct laser writing technique	18
2.3 Hyperbolic metamaterial	19
2.3.1 Physical geometry	20

2.3.2	Physical mechanisms and effective parameters	21
2.3.3	Discussion	29
2.3.4	Fabrication with STED-DLW	32
2.4	Hollow waveguides with negative index metamaterial cladding . . .	32
2.4.1	Analytical analysis	35
2.4.2	Numerical analysis	46
2.5	Direct laser metal writing technique	50
2.6	Conclusion	52
3	Compensation of losses without gain media	55
3.1	Introduction	55
3.2	Procedure for the inverse filter loss compensation technique emulating the Π scheme	58
3.3	Application of the Π scheme to different loss mechanisms in the imaging system	76
3.4	Conclusion	91
4	Miniaturized RF and optical components	93
4.1	Introduction	93
4.2	Extremely sub-wavelength negative index metamaterial	94
4.2.1	Physical geometry	94
4.2.2	Effective parameters and physical mechanisms	95
4.3	Metamaterial-based beam splitter	107

4.3.1	Fishnet metamaterial	108
4.3.2	Polarizing beam splitter	110
4.3.3	Partially polarizing beam splitter	112
4.3.4	Non-polarizing beam splitter	113
4.4	Conclusion	114
5	Summary and future work	115
5.1	Summary	115
5.2	Future work	118
	References	121
	A Letters of permission	145
	B MATLAB code	149
B.1	Extending inverse filter loss compensation technique to hyperlens	149
B.2	Equipfrequency plot	156

List of Figures

1.1	“Light” in oracle bone script	2
2.1	Free-standing gold hyperbolic metamaterial unit cell structure with geometric parameters. [Reprinted/Adapted] with permission from ref [1], [Optical Society of America].	21
2.2	Schematics of three different magnetic dipoles excited inside the unit cell of the metamaterial under different incidences of light. Arrows indicate magnetic dipole loop currents induced by (a) normally incident light, (b) laterally incident TE-polarized light, and (c) laterally incident TM-polarized light. [Reprinted/Adapted] with permission from ref [1], [Optical Society of America].	23

2.3 (a) Transmittance (T), reflectance (R), and absorbance (A) spectra for normally incident light. The structure is periodic in the xy plane and has one layer along the z direction. Retrieved effective (b) refractive index, (c) permittivity, and (d) permeability. The dashed black line in (b) is the first Brillouin zone edge. (e) Current density distribution at $f = 27\text{THz}$. Colors show the y component of the current density J_y (i.e., red and blue correspond to the $+y$ and y directions, respectively). (f) The same as (e) except that colors show the z component of the current density J_z (i.e., red and blue correspond to the $+z$ and z directions, respectively). [Reprinted/Adapted] with permission from ref [1], [Optical Society of America]. 24

2.4 (a) Transmittance (T), reflectance (R), and absorbance (A) spectra for the TE-polarized laterally incident light. The structure is periodic in the yz plane and has one layer along the x direction. Retrieved effective (b) refractive index, (c) permittivity, and (d) permeability. The dashed black line in (b) is the first Brillouin zone edge. (e) Current density distribution at $f = 22\text{THz}$. Colors show the x component of the current density J_x (i.e., red and blue correspond to the $+x$ and x directions, respectively). (f) The same as (e) except for J_z . [Reprinted/Adapted] with permission from ref [1], [Optical Society of America]. 26

2.5	(a) Transmittance (T), reflectance (R), and absorbance (A) spectra for the TM-polarized laterally incident light. The structure is periodic in the yz plane and has one layer along the x direction. Retrieved effective (b) refractive index, (c) permittivity, and (d) permeability. The dashed black line in (b) is the first Brillouin zone edge. (e) Current density distribution at $f = 40\text{THz}$ for (e) J_x and (f) J_y . Arrows overlaying the surface plots in (e) and (f) indicate the complete dipole loop current. Only one of the loops is shown for clarity [see Fig. 2.2(c) for the location of other loop]. [Reprinted/Adapted] with permission from ref [1], [Optical Society of America].	27
2.6	Equipfrequency contours for the TE-polarized light propagating in the xz plane show hyperbolic dispersion. The structure is periodic in the xy plane and has five layers along the z direction. [Reprinted/Adapted] with permission from ref [1], [Optical Society of America].	28
2.7	Real parts of the effective magnetic permeability in the same graph corresponding to three different magnetic dipoles studied in Figs. 2.3 –2.5. The curves intersecting around 40THz show potential for nontrivial three-dimensionally isotropic permeability. [Reprinted/Adapted] with permission from ref [1], [Optical Society of America].	31
2.8	SEM image for hollow meandering wire template (with permission from Dr. Martin Wegener)	33

2.9	Schematic geometry of a symmetric slab waveguide	35
2.10	Left: n_{eff} versus k_0d for surface modes and waveguide modes, Center: dispersion diagrams of TE ₂ mode, and Right: attenuation of TE ₂ mode under three different cases. Solid blue line, dash green line and dot red line correspond to <i>lossless</i> , <i>less lossy</i> , and <i>lossy</i> cases, respectively.	45
2.11	Numerical result comparing with analytical result. Solid red line rep- resents analytical result, and black circle marker represents numerical result.	47
2.12	Geometry of a linearly tapered waveguide with negative index material (NIM) cladding. Purple arrow indicates the propagation direction.	48
2.13	Snapshots of the propagation of the pulse at different moments for <i>lossless</i> case, <i>less lossy</i> case and <i>lossy</i> case, respectively.	49
2.14	(a) Geometry of the designed waveguide with cladding made of practi- cal structure. (b) snapshots of the electric field distribution at different moments	50
2.15	56 μ m diameter silver rings that exhibits negative permittivity at 400 μ m wavelength. [Reprinted/Adapted] with permission from Kevin Vora.	51
2.16	36 μ m diameter silver split rings with 1 μ m gap size that exhibits neg- ative permittivity at 400 μ m wavelength. [Reprinted/Adapted] with permission from Kevin Vora.	52

3.1	Replicated hyperlens magnetic field (A/m) distribution simulation result corresponding to Fig. 2(b) from [2]. Two 50nm wide openings in a 50nm thick Cr layer are considered as the object. The center to center separation of the openings is 150nm. The working wavelength is 365nm. Image taken from ref [3], [EMW Publishing].	59
3.2	Geometry for the studied hyperlens designed in COMSOL. Cylindrical coordinate system (ρ, ϕ, z) is used in the simulation. [Reprinted/Adapted] with permission from ref [4], [Optical Society of America].	60
3.3	Calculated (a) amplitude and (b) phase of the hyperlens transfer function (blue) plotted with the corresponding compensation filter (green). Image taken from ref [3], [EMW Publishing].	78
3.4	(a) Amplitude and (b) phase Fourier spectra for the original object, raw image, and compensated image, respectively. (c) Magnetic field intensity for the original object, truncated object, raw image, and compensated image. The compensated image is clearly resolved beyond the diffraction limit. Image taken from ref [3], [EMW Publishing]. . . .	78
3.5	Magnetic field intensity for the original object, truncated object, raw image, and compensated image for (a) 328nm wavelength, and (b) 372nm wavelength	79

3.6	Comparison of the images obtained by spatial filtering (green light solid line) and the Π scheme (black solid line) using a coherent superposition of an auxiliary object and the original object as the total input (blue, dash-dotted line) for the hyperlens. Image taken from ref [3], [EMW Publishing].	80
3.7	(a) Amplitude (A/m) and (b) phase Fourier spectra for the original object, raw image, and compensated image. (c) Magnetic field intensity for the original object, raw image, and compensated image. The Π scheme accounts for the discretization and impedance mismatch losses resulting in a compensated image with a high resolution of $\lambda_0/7$. [Reprinted/Adapted] with permission from ref [4], [Optical Society of America].	83
3.8	(a) Amplitude (A/m) and (b) phase Fourier spectra for the original object, raw image, and compensated image. (c) Magnetic field intensity for the original object, raw image, and compensated image. The Π scheme accounts for impedance mismatch loss resulting in a compensated image with a high resolution of $\lambda_0/9.6$. [Reprinted/Adapted] with permission from ref [4], [Optical Society of America].	85

3.9 (a) Location where the impedance mismatch occurs. (b) The region indicated by the dashed circle in (a) is enlarged. (c) The region indicated by the dashed circle in (b) is enlarged. The two curves, which are $2nm$ away from the interface, are defined as the upper and the lower boundaries to calculate the transmission coefficient $t_{int}(m)$. See the text for the details. [Reprinted/Adapted] with permission from ref [4], [Optical Society of America]. 87

3.10 (a) Fourier spectra (A/m) for the auxiliary objects calculated by the two different methods. (b) Magnetic field intensity for the truncated object, raw image, and the image from the total input for the two different auxiliary objects. [Reprinted/Adapted] with permission from ref [4], [Optical Society of America]. 89

3.11	Image contrast and resolution of the magnifying superlens are improved with the plasmon injection inverse filter. The FWHM of the Gaussian features in the image is reduced from 77nm (red solid line) to 63nm (green solid line) with the plasmon injection inverse filter. The Gaussian features in the object has a FWHM of 61nm (blue solid line) and is separated by 130nm. The operating wavelength of the magnifying superlens is 532nm. The truncated object (black dashed line) with $m = 25$ perfectly represents the object in the filtering process. [Reprinted/Adapted] with permission from ref [4], [Optical Society of America].	90
4.1	Schematic of the (a) spiral and (b) meandering wire structure with the geometric parameters indicated. (c) Side view of a small section of the structure showing material layers. Image taken from ref [5], [EMW Publishing].	96
4.2	(a) Transmittance (T), reflectance (R), and absorbance (A) spectra. (b) Retrieved effective refractive index. (c) Effective permittivity, and (d) effective permeability. The spiral has 60 turns. Image taken from ref [5], [EMW Publishing].	97

4.3	<p>((a) Transmittance (T), reflectance (R), and absorbance (A) spectra. (b) Retrieved effective refractive index. (c) Effective permittivity, and (d) effective permeability. The number of turns in the spiral is reduced to 40 turns to blue-shift the operating frequency of the negative index metamaterial. This enables the metamaterial relatively better impedance matched to free space. Image taken from ref [5], [EMW Publishing].</p>	98
4.4	<p>(a) Magnetic field at 5.7MHz in the structure considered in Fig. 4.2. Colors show the z-component of magnetic field Hz. (b) Corresponding current density distribution. Colors show the x-component of current density J_x. (c) The same as (b) except that colors show the y-component of current density J_y. The complete loop current is indicated by black arrows overlaying the current density plots in (b) and (c). (d) The magnitude of the current density and (e) its distribution along a line extending from the center of the spiral to the edge. Image taken from ref [5], [EMW Publishing].</p>	99
4.5	<p>(Transmittance (T), reflectance (R), and absorbance (A) spectra for the metamaterial with straight continuous wire on the back side of the substrate. Image taken from ref [5], [EMW Publishing].</p>	101

4.6	(a) Current density distribution on the meandering wire at 5.7MHz. Colors show the x-component of the current density J_x . (b) The same as (a) except that colors show the y-component of current density J_y . The arrows overlaying the surface plots in (a) and (b) indicate the non-resonant current which flows along the meandering wire. (c) The magnitude of the current density. Image taken from ref [5], [EMW Publishing].	103
4.7	Graphical comparison of numerical and analytical results in Table 1 for ω'_p/ω_p . Image taken from ref [5], [EMW Publishing].	105
4.8	(a) Effective permittivity and permeability using the meandering wire parameters in Table 4.1. (b) The attainable most extreme refractive index and the corresponding FOM. The geometrical parameters for the spiral are the same as in Fig. 4.2. Image taken from ref [5], [EMW Publishing].	105
4.9	Schematic of the (a) fishnet structure with the geometric parameters indicated. (b) Side view of the structure showing material layers.	109
4.10	(a) x-component of Electric field E_x and (b) y-component of electric field E_y at $1.55\mu\text{m}$	111
4.11	Effective impedance under (a) TE-polarized and (b) TM-polarized incident light.	112

4.12 Reflectance (R), transmittance (T), and absorbance (A) spectra versus

(a) w_x , and (b) Λ_x 114

List of Tables

4.1	Numerical and analytical results for ω'_p/ω_p using different meandering wire parameters; N_o is used to enumerate the parameter sets, m is the number of periods and l is the length of horizontal parts in nm. . .	106
-----	--	-----

Preface

This dissertation presents my research work in pursuing the PhD degree at Michigan Technological University. This dissertation includes materials from previously published journal articles in Chapters 2-4.

Chapter 2 contains one previously published article in Journal of the Optical Society of America B [X. Zhang, S. Debnath, and D. Guney, “Hyperbolic metamaterial feasible for fabrication with direct laser writing processes,” J. Opt. Soc. Am. B 32, 1013 (2015)]. As the first author, I contributed to the methodology investigation, simulations, result analysis and draft writing. Sanjay Debnath gave many simulation suggestions. Dr. Durdu Guney directed me to the research topics, supervised the whole research process and revised the draft.

Chapter 3 contains two previously published article in (1) Progress In Electromagnetics Research C [X. Zhang, W. Adams, M. Sadatgol, and D. Guney, “Enhancing the resolution of hyperlens by the compensation of losses without gain media,” Prog. Electromagn. Res. C 70, 1 (2016)], (2) Journal of the Optical Society of America B [X. Zhang, W. Adams, and D. Guney, “Analytical description of inverse filter emulating the plasmon injection loss compensation scheme and implementation for ultrahigh-resolution hyperlens,” J. Opt. Soc. Am. B 34, 1310 (2017)]. As the first

author of these two articles, I contributed to the methodology investigation, analytical calculations, simulations, results analysis and draft writing. Dr. Durdu Guney directed me to the research topics, supervised the whole research process and did the final revision of the draft. Wyatt Adams, as the second author, gave suggestions about results analysis and revised the draft. Mehdi Sadatgol, as the third author of the paper published in JOSAB, also revised the draft and gave suggestions about simulations.

Chapter 4 contains one published article in Progress In Electromagnetics Research [X. Zhang, E. Usi, S. Khan, M. Sadatgol, and D. Guney, “Extremely sub-wavelength negative index metamaterial,” *Prog. Electromagn. Res.* 152, 95 (2015)]. As the first author, I contributed to the methodology investigation, simulations, results analysis and draft writing. Dr. Durdu Guney directed me to the research topics, supervised the whole research process and did the final revision of the draft. Elvis Usi and Suhail Khan, as the second and third authors, did some parts of the preliminary simulations. Mehdi Sadatgol, as the fourth author, also helped to revise the draft.

Acknowledgments

Firstly, I would like to give my sincerest gratitude to my advisor, Dr. Durdu Guney, for his guidance, support, and patience over the years. It was a great pleasure working with him, and he helped me transform from a confused PhD student to an independent professional researcher. Without him, I will not be where I am today.

Besides, I would like to thank my committee members, Dr. Semouchkina, Dr. Middlebrook, and Dr. EI-Ganainy for their valuable help, suggestions, and encouragements in different steps of my PhD study.

In addition, I am grateful for the support from National Science Foundation (ECCS-1202443) and Office of Naval Research (N00014-15-1-26).

Moreover, I also appreciate the help from Department Chair, Dr. Fuhrmann and other staffs, Joan, Lisa, Michele, and Chuck. Their smile and willingness to help make me feel welcome in the Department of Electrical and Computer Engineering.

Meanwhile, I am also grateful to our research group members, Ankit Vora, Mehdi Sadatgol, Wyatt Adams, Anindya Ghoshroy, James Davis, Sanjay Debnath, Mahfuzur Rahman, and Jiemin Zhang. I appreciate their companion and helpful discussions. Besides that, I am also thankful to all my friends who give me many unforgettable

moments and happiness.

The final and most important thanks belong to my parents. They always give me their unconditional loves and supports during my whole life. Their inspirations and encouragements help me to make this day reality. Meanwhile, I will also give my big thanks to my husband Whensheng, who always stay with me no matter I was happy or sad!

Abstract

The development of metamaterials provides a new way to manipulate electromagnetic waves by sub-wavelength artificial structures, and hence brings new properties and functionalities that cannot be found with conventional materials. This leads to the possibility of previously unthought-of applications, including perfect lenses, invisibility cloaks, and perfect absorbers. However, several critical challenges need to be addressed before transiting from intriguing scientific findings to real-world usable devices.

This dissertation deals with two challenges regarding the practical use of metamaterials. Firstly, fabrication of truly three-dimensional (3D) and large-scale metamaterials is needed to increase the degrees of freedom of the functionality for device level applications. Direct laser writing (DLW) technique is a potential choice to fabricate such materials with special design requirements. A hyperbolic metamaterial and a hollow waveguide with negative index metamaterial cladding that satisfy the vertical connectivity requirement are proposed, and hence they have the potential to be fabricated with DLW. Three different magnetic dipoles supported by the hyperbolic metamaterial are investigated and contribute to hyperbolic dispersion. In addition, the adverse effect of material absorption on the hollow waveguide with negative index cladding

is studied, which leads to the second challenge: how to avoid losses. A loss compensation technique called the plasmon injection (Π) scheme is successfully applied to an experimental hyperlens and a magnifying superlens. The extension of this Π scheme to the hyperlens is analytically described and numerically implemented. The equivalent of the spatial filter with the Π scheme is demonstrated and the resolution enhancement is obtained for both the hyperlens and the magnifying superlens.

In addition, this dissertation also provides a possible solution to meet the need for miniaturized devices. Metamaterials have potential advantages compared with conventional materials for compact design due to their sub-wavelength unit cells and arbitrary control of electromagnetic responses. An extremely sub-wavelength negative index metamaterial (NIM) working at radio frequency (RF) is proposed. The idea of improving the transparency of the metamaterial by reducing the diluted plasma frequency is investigated. Meanwhile, at optical frequencies, a metamaterial-based beam splitter is proposed and able to achieve polarizing, partially polarizing and non-polarizing properties by changing its geometry.

Chapter 1

Overview

1.1 Background

A little while after the Big Bang, the light appeared in the universe. The earthlings rely on light to conduct normal life activities. One example showing the importance of light to humans is the oracle bone script (i.e., the earliest form of Chinese characters) of “light”, shown in Figure 1.1. It depicts a person holding fire above his head, indicating a naive understanding of the originality of the light. Light was not fully understood until the 19th century. Inspired by Michael Faradays discovery of the relationship between light and electromagnetism, James Clerk Maxwell found that

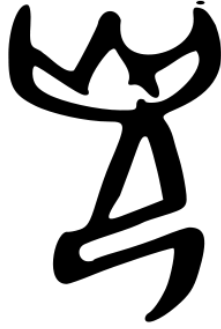


Figure 1.1: “Light” in oracle bone script

the electromagnetic waves propagate at a constant speed, which is equal to the previously measured speed of the light. Based on this observation, Maxwell concluded that light is a form of electromagnetic radiation. At the same time, he summarized the previously established experimental facts in four equations, known as Maxwell’s equations. This was a milestone in the human history of unraveling the mystery of light. We realized that from the sunrise glory, the red sunset flame, the brilliant colors of the rainbow, to the twinkling of stars in the sky, all these beautiful sceneries are the masterpiece of electromagnetic radiation.

With the advancement of the theoretical understanding of light, humans successfully controlled electromagnetic waves at new levels. A convex lens is used to produce a magnified image; a corner reflector is used to reflect the microwave and radio waves emitted by radar; and a blackbody is used to absorb all the incident electromagnetic radiation. Recently, research was focused on the interaction between light and nanoscale artificial materials. These nanoscale materials belong to a wide class of man-made materials called metamaterials, a term first coined in the late 1990s [6].

The Greek word “met” means “altered, changed” or “higher, beyond”, which indicates that the interaction between electromagnetic waves and metamaterials can lead to a response beyond nature. The chemical compositions of metamaterials are dielectrics and metals, which do not have any special effects on their own. The magic comes from the arrangement of these materials, such as special geometry and small unit cell size. The unit cell size is typically smaller than the operating wavelength. Their properties are mainly due to their microscopic structure, rather than their chemical compositions.

Metamaterials can be designed to exhibit desired permittivity and permeability, and many fascinating metamaterials are created, such as negative index metamaterials (NIM) [7], which have simultaneous negative permittivity and permeability, and hyperbolic metamaterials [8], where the permittivity or permeability have opposite signs along different directions. With these special properties, metamaterials have a variety of novel applications, such as perfect lenses [9], hyperlenses [10, 11], perfect absorbers [12, 13], compact antennas [14, 15], transformation optics [16, 17], invisibility cloaks [18], solar photovoltaics [19], and many others.

1.2 Problem statement

Challenges need to be addressed to achieve the broader impacts of metamaterials. Besides, metamaterials can be considered as the potential solutions to address the challenges of other device level applications. The following section identifies four challenges in the practical use of metamaterials, and one more opportunity provided by metamaterials.

1. Fabrication of truly three-dimensional (3D) and large-scale metamaterials

So far, most of the optical metamaterials have been fabricated by well-established two-dimensional (2D) fabrication technologies, such as standard e-beam lithography [20], focused-ion-beam lithography [21], interference lithography [22, 23], and nanoimprint lithography [24, 25]. However, these technologies only allow the stacking of several planar functional layers. Fabrication of truly 3D metamaterials is more than just making the 2D layers thicker [26], the degrees of freedom of the functionality needs to be increased [27], which means additional orientated structures are necessary. Another crucial factor is flexibility in tailoring the metamaterial's unit cell interior [28, 29].

The rapid development of 2D metamaterials, also known as metasurfaces, has occurred in recent times due to their low loss and small physical size. Metasurfaces can be used to achieve the same functionalities as metamaterials in some applications,

such as metalenses [30], small antennas [31], perfect absorbers [32] and polarization converters [33]. However, other optical devices, including hyperlenses [10, 11], perfect lenses [9, 34] and triaxial optical inclinometers [35] cannot be obtained using metasurfaces. In addition, specific metasurfaces only work with stringent requirements. For example, strong optical activity and circular dichroism can be achieved by chiral metamaterials under a normal incident light [36, 37], while by using metasurfaces, this strong chirality can only be accomplished under oblique incidence [38, 39]. It is also difficult to accurately shape the metasurfaces patterns in large areas under e-beam lithography and focused-ion-beam lithography [40]. Large-area fabrication of metasurfaces has been achieved by direct laser writing technique recently [41, 42, 43, 44]. However, these metasurfaces almost always operate at infrared frequencies. Thus, we expect that research on the fabrication of 3D and large-scale optical metamaterials will continue keeping pace with the one on metasurfaces.

2. Fully isotropic metamaterials with functionality independent of the direction of propagation and polarization of the incident light

Until now, most of the metamaterials are anisotropic materials, which means that the response of the system depends on the direction of illumination and polarization. This property limits metamaterials' practical applications. For example, perfect lenses [9] require fully isotropic NIMs operating at optical frequencies.

In the past few years, fully isotropic NIMs operating at microwave frequencies were

theoretically studied [45, 46] and experimentally demonstrated [47, 48]. However, at optical frequencies, less progress has been made compared to those at microwave frequencies. At optical frequencies, the majority of the research was based on the idea of arranging the split ring resonators (SRRs) in all three dimensions to achieve isotropic NIMs [49, 50]. However, these designs are difficult to realize due to complex fabrication processes. In 2010, an isotropic NIM that consisted of multilayers was proposed [51]. The structure achieved isotropy only under TM polarized incident light. Another research group proposed and fabricated a core-shell structure in 2016 to attain an isotropic negative index property [52], but the isotropic property was not demonstrated. To the best of my knowledge, fully isotropic NIMs operating at optical frequencies with functionality independent of the direction of propagation and polarization of the incident light has not been successfully demonstrated yet.

3. How to avoid losses

Metallic metamaterials [53], as the first experimentally implemented metamaterials [7], have achieved remarkable development in theory and fabrication. However, ohmic losses are nontrivial due to the metal components, especially at optical frequencies. These losses stop the materials from functioning and lead to a variety of undesired phenomena, such as resolution limitation of the perfect lenses [34], adverse effect of the slow light waveguides [54], and performance decrease in the metamaterial antennas [55].

Recently, all-dielectric metamaterials [56] overcome the critical issue of heat dissipation and achieved many electromagnetic responses, such as magnetic resonances [57, 58], negative refractive index [59, 60], and zero refractive index [61, 62]. A variety of their applications have been demonstrated, including perfect reflectors [63, 64], magnetic mirrors [65, 66], and Huygens sources [67, 68]. All-dielectric metasurfaces consisting of a thin layer of engineered dielectric nanostructures can achieve even higher transmission and complete control of both the polarization and the phase of electromagnetic waves [69]. These 2D surfaces can modify the wavefront of the incident waves in applications such as flat lenses [70, 71] and beam shaping [72, 73]. The field enhancements obtained in all-dielectric metamaterials and metasurfaces are from high-index materials [56]. However, the high refractive index comes at the cost of increased absorption [74], especially at optical frequencies. Meanwhile, the choice of materials also limits the applications of all-dielectric metamaterials and metasurfaces at visible frequencies.

Therefore, at optical frequencies, metallic metamaterials have more freedom to achieve functional devices compared with all-dielectric metamaterials. Thus, it is critical to address the innate loss issues in metallic metamaterials

4. Broad bandwidth and real-time tunability

Many metamaterials are highly dispersive due to their resonant structures. The desired optical parameters are usually obtained in a small frequency range. However,

a broad bandwidth will enable broad metamaterial applications, such as invisibility cloaking [16] and perfect absorbers [75]. In addition, reconfigurable metamaterials attracted much attention regarding their ability of real-time electromagnetic radiation manipulation, which expand the potential of metamaterial applications even further [76, 77, 78] and relieve the need for broad bandwidth. A variety of approaches to achieve tunability were proposed, and many of them were based on integrating metamaterials with various active materials such as semiconductors [79, 80], liquid crystals [81, 82] and graphene [83, 84, 85]. However, future development is needed, including spatial tuning of metamaterials, tunable range extension and the expansion of available tunable materials.

5. Miniaturization of RF and optical devices

In addition to the above four challenges that prevent the broader impacts of metamaterials, metamaterials provide a potential solution to the miniaturization issue.

Doing more with less is the goal of our era. The driving forces for smaller devices come from the need for miniature size in specific applications, and the need to reduce material costs. Due to the sub-wavelength property of metamaterials, they are envisioned as the next-generation materials for compact circuits.

When metamaterials work at lower frequencies, on the order of 100 MHz or lower, the

dimensions of a single unit cell can be impractically large even though it is still sub-wavelength. Given the wavelengths at such low frequencies and typical sizes of the metamaterial elements on the order of $\sim \lambda_0/10$ to $\sim \lambda_0/100$, where λ_0 is the free space wavelength, the individual elements can be as large as hundreds of meters [86], which leads to many problems. For example, the large size of metamaterial perfect absorbers makes them difficult to integrate into real radio devices for telecommunications [87]. The unit cell designs for increasing wireless power transfer (WPT) are too large to create a practical metamaterial sample combined with conventional WPT system [88].

Meanwhile, photonic integrated circuit (PIC) have made remarkable progress in the past few decades. Compared with the electronic integrated circuit, PIC provides many advantages, including broader bandwidth [89] and reduced Joule effect [90]. Therefore, PIC is promising in the fields of imaging, sensing and optical communications. At present, great attention is paid to make high-density integration and high-level functionality PIC. To achieve these goals, compact, advanced, and functional photonic devices operating at optical frequencies are required, and metamaterials have the potential to fulfill these requirements.

1.3 Research objectives

This dissertation aims to address several critical challenges mentioned in section 1.2. At the same time, the dissertation explored and demonstrated the potential to obtain miniaturized RF and optical components using metamaterials. The three specific tasks are detailed next.

1. Towards 3D bulk photonic metamaterials

Generally, the research on constructing 3D metamaterial samples has two directions. One is directly usage of 3D unit cells and the other is stacking and repeating of several functional layers. So far, most work is based on the latter method. In 2008, Liu et al. reported a photonic metamaterial consisting of four SRR arrays stacked by using a layer-by-layer technique [91]. Careful lateral alignment of different layers is required for successful stacking. This requirement would lead to long fabrication time, which makes this technique too costly for large-scale 3D metamaterials.

Two other promising large-area nano-fabrication techniques, nanoimprint lithography (NIL) and self-assembly (SA) were developed. In 2011, Chanda et al. reported a flexible 3D optical NIM fabricated by a NIL technique [92]. A multilayer structure was deposited on a soft imprinting mold using e-beam evaporation; then this patterned multilayer structure was transferred to the target substrate by contacting the mold

with the substrate. The resolution of NIL technique is related to the molds rather than the diffraction limit. In addition, the fabrication steps, including exposure and etching, can be reduced in NIL processes, and this leads to high throughput. However, NIL has some drawbacks. For example, it is hard to have the complex and fine patterns precisely carved into the molds [93, 94]. In 2011, Lodewijks and his colleagues used self-assembled nanospheres as a mask to make large-area double fishnet metamaterial structures [95]. Due to the bottom-up process [95, 96, 97], SA can fabricate complex nanostructures that cannot be realized with the top-down methods. However, the main challenge for SA is to fabricate anti-symmetric structures [98].

Moreover, many other new fabrication technologies were proposed. Jie Yao et al.[99] reported a bulk metamaterial made of nanowires by preparing a porous alumina template through electrochemical anodization and silver deposition. However, this technique has several disadvantages, including long fabrication time and toxicity [100]. Another approach to realize more complex designs is membrane projection lithography. Vertically-oriented split-ring resonators have been experimentally demonstrated [50]. Although this technology is flexible, the idea of this approach is still the stacking of layers.

Besides that, direct laser writing (DLW) technique [101] is another promising approach, since DLW has the potential to realize vertically connected arbitrary 3D

structures. For example, 3D helix structure is a popular chiral structure and can be used as broadband circular polarizer [102, 103, 104]. It is easy to fabricate with DLW but difficult with previous techniques. Moreover, the DLW technique is a low-cost and rapid prototyping approach that makes it more attractive.

Although DLW provides a way to create more complex shaped 3D structures, this technique is unable to produce vertically disconnected samples, which brings in the design challenge. Therefore, the designed structures should satisfy the vertical connectivity condition. Based on this requirement, we propose a hyperbolic metamaterial and a hollow waveguide with negative index cladding, which have the potential to be fabricated with DLW. By collaborating with Dr. Martin Wegener's research group in Germany, the hyperbolic metamaterial template was fabricated. Meanwhile, the adverse effect of losses is studied in the waveguide section, which leads to the second research objective. This work will be presented in Chapter 2.

2. Loss compensation

Losses are always an important issue in not only bulk metamaterials but also single layer metasurfaces. An obvious approach to compensate losses is to introduce gain medium. In 2010, Sebastian Wuestner et al. [105] inserted dye molecules into the dielectric host and excited them by an optical picosecond pulse. The results showed full compensation of losses in the fishnet metamaterials. Another approach using a layer of quantum dots deposited on a metamaterial array of split ring slits was

proposed [106]. By optically pumping the semiconductor quantum dots, the Joule losses in metallic metamaterial arrays were reduced. There are many concerns about using active compensation of losses by gain medium such as the short chemical time of the dye molecules, the complex configuration of pump systems, the short-time stability and gain saturation issues.

Recently, a loss compensation technique called plasmon injection (Π) scheme was proposed [107]. The original Π scheme relies on the coherent superposition of externally injected surface plasmon polaritons with the local eigenmodes of a metamaterial to provide full loss compensation. This technique does not need a traditional optical-gain providing medium, hence it eliminates its associated complexities. In the meantime, Π scheme is equivalent to applying a simple spatial filter for imaging [107]. Previously, our group successfully applied the Π scheme to a perfect lens [108]. In this dissertation, the Π scheme is extended to hyperlenses and its implementation is demonstrated by an inverse filter. This work will be presented in Chapter 3.

3. Miniaturized RF and optical components

Another task in this dissertation is to explore the metamaterials' potential to obtain miniaturized RF and optical components. At radio frequencies, the approach to miniaturize components is to use deeply sub-wavelength structure designs. Until now, the extremely sub-wavelength magnetic metamaterial has been designed with the unit cell size of about 2000 times smaller than the resonant wavelength [86]. A

deeply sub-wavelength electric metamaterial has also been shown operating at GHz frequencies with the ratio of free space wavelength to the unit cell size (i.e., λ/a) of about 70 [109].

NIMs working at RF have many potential applications. For example, NIMs can be used as a phase shifter to form an integral part of RF integrated circuit devices [110]. Moreover, NIMs can focus radio waves to improve satellite and molecular imaging [111]. Deeply sub-wavelength negative index metamaterials have been previously designed based on a lumped element with the unit cell size of only $\sim \lambda_0/75$ at 400MHz [112]. Available manufactured lumped circuit elements offer only limited and coarse values. The desired operating frequency still depends on the geometric unit cell design. Losses associated with lumped elements and the difficulties with the modeling are other challenges discussed in detail in [112]. Here, we propose an extremely sub-wavelength negative index metamaterial working at RF with λ/a ratio reaching above 1700 and the refractive index reaching around -109. This work will be presented in Chapter 4.

At optical frequencies, metamaterials in place of conventional materials have the potential to achieve compact, advanced and functional photonic devices [113, 114], because metamaterials consist of sub-wavelength unit cells and can achieve arbitrary control of electromagnetic responses. Here, we propose a metamaterial-based beam splitter which can be integrated with other optical devices for quantum manipulation

of light. This beam splitter can achieve polarizing, partially polarizing, and non-polarizing properties by manipulating the effective permittivity and permeability.

This work will also be presented in Chapter 4.

Chapter 2

Towards 3D bulk photonic metamaterials ¹

2.1 Introduction

In this chapter, we discuss the first objective mentioned in section 1.2: towards 3D and large-scale metamaterials. We first briefly introduce the DLW and STED-DLW techniques which can enable the fabrication of 3D and large-scale metamaterial samples. Then we propose a hyperbolic metamaterial and a hollow waveguide with negative index cladding that satisfy the vertical connectivity requirement for fabrication with

¹Some parts of the material contained in this chapter were previously published in J. Opt. Soc. Am. B 32, 1013 (2015). Refer Appendix A for granted permission to be published. Some parts of the material contained in this chapter will be submitted to J. Opt. Soc. Am. B in the future.

STED-DLW in section 2.3 and 2.4, respectively. Finally, we introduce a direct laser metal writing technique that can fabricate disconnected metal features.

2.2 Direct laser writing technique

DLW, based on two-photon polymerization, can enable the fabrication of truly bulk and computer-controlled arbitrarily shaped 3D complex structures [101, 104, 115] that are not possible with traditional photolithographic processes [116]. DLW has important potential in the fabrication of metamaterials, especially at frequencies ranging from mid-IR to visible, since it offers a viable route as a low-cost and rapid prototyping tool for truly 3D fabrication of nanostructures. Fabrications of large-area, complex metallic nanostructures [117] and metamaterials [104] have been demonstrated with DLW and subsequent metalization.

However, the resolution of DLW cannot go beyond the diffraction limit. So stimulated-emission-depletion-microscopy-inspired direct laser writing (STED-DLW) [118, 119, 120] was developed. The idea is to apply a second laser mode that locally and reversibly disables the resist polymerization. As a result, the effective polymerization volume will reduce below the usual diffraction-governed volume. With STED-DLW, a feature size reduction by more than a factor of two has been demonstrated [121]. Additionally, with the combination of STED-DLW and the “dip-in”

approach [122], metamaterial height can reach the level of 1mm, where one can think about constructing macroscopic metamaterials [123].

Here, inspired by the rapid progress in DLW, we propose a hyperbolic metamaterial and a hollow waveguide with negative index cladding that have the potential to fabricate with STED-DLW processes followed by electroplating of gold [104].

2.3 Hyperbolic metamaterial

Hyperbolic metamaterials [124, 125] have emerged as one of the most interesting and promising subclasses of metamaterials with practical applications ranging from sub-wavelength imaging [10, 11, 126, 127, 128, 129] to the engineering of spontaneous [130, 131, 132] and thermal emission [133].

Concerning the fabrication of optical hyperbolic metamaterials, layered metal–dielectric structures [11, 131] and nanowire arrays [130, 134] have appeared as two common approaches. The largest sample size of $1\text{cm} \times 1\text{cm} \times 51\mu\text{m}$ was achieved with nanowire arrays fabricated by electrochemical deposition of a metal on a porous alumina membrane [135]. Multilayer fishnet structures [136] and graphene metamaterials [137] with hyperbolic dispersion have been theoretically proposed. However, to fabricate truly bulk optical metamaterials, a 3D fabrication

approach is needed. Particularly, the practical realization of hyperbolic metamaterial devices such as the hyperlens [10], which is one of the most captivating manifestations of hyperbolic dispersion, demands three-dimensional volume structures.

Here, we propose the first blueprint of a hyperbolic metamaterial structure amenable to fabrication with STED-DLW processes. The structure has operating frequencies at mid-IR frequencies and the features within the resolution of state-of-the-art STED-DLW technologies.

2.3.1 Physical geometry

The unit cell of the hyperbolic metamaterial structure consists of two pairs of meandering wires with inversion symmetry (see Fig. 2.1). The dimension of the unit cell is $2513\text{nm} \times 2513\text{nm} \times 2290\text{nm}$. The wires are modeled by using experimental Drude model parameters for bulk gold with plasma frequency of $f_p = 2180\text{THz}$ and collision frequency of $f_c = 19.1\text{THz}$ as given in [104]. The simulations are performed by using the finite-integration-method-based CST Microwave Studio software package. Frequency domain solver is used to calculate the s-parameters corresponding to the complex reflection and transmission coefficients. Then, these s-parameters are used to retrieve the effective medium parameters of the metamaterial [138]. Unit cell boundary conditions are chosen to impose the periodic or quasi-periodic boundary

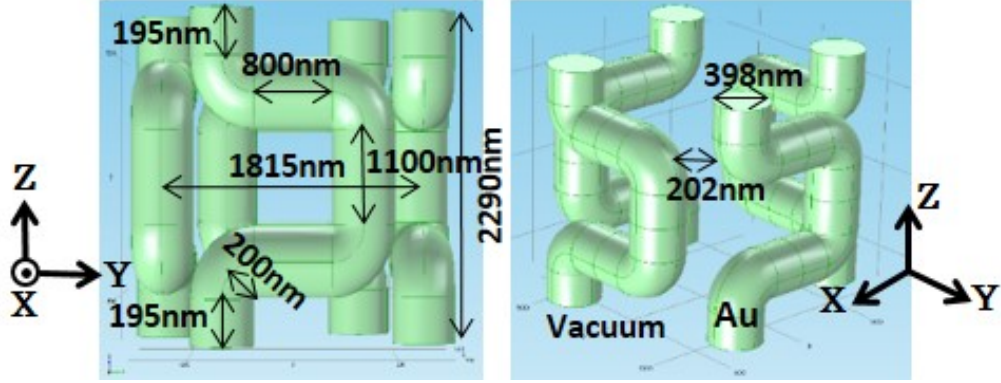


Figure 2.1: Free-standing gold hyperbolic metamaterial unit cell structure with geometric parameters. [Reprinted/Adapted] with permission from ref [1], [Optical Society of America].

conditions as necessary in the simulations. The tetrahedral meshes with the adaptive meshing method are selected to accurately represent the models to be simulated.

2.3.2 Physical mechanisms and effective parameters

Different magnetic dipoles [139] with close resonance frequencies can be excited inside the structure in Fig. 2.1 under different incidences of light. The resonances underlying the magnetic dipoles arise from the combined capacitance and inductance of the nanocircuits inside the structure similar to split-ring resonators. Figure 2.2 schematically illustrates three different magnetic dipoles that can be excited under different incidences of light. E and H stands for incident electric and magnetic field, respectively. In all the cases the metamaterial is periodic in the planes perpendicular to and finite along the incident wave vector k . Color arrows represent the current loops for the induced magnetic dipoles. The planes of these current loops are perpendicular to

the respective incident magnetic field H , since the dipoles are magnetically excited. For clarity, only the loop currents excited by H perpendicular to the plane of the loops are shown [e.g., the loop current in (a) is excited by H along the x direction]. Using symmetry considerations, current loops at different planes can be also excited [e.g., in (a) if H is chosen along the y direction], and magnetic dipoles in the $x - z$ planes are excited; thus, the structure becomes polarization independent in the $x - y$ plane for normal incidence. Below we refer to the current loops in the $y - z$ plane [see Fig. 2.2(a)] and the $x - z$ plane [see Fig. 2.2(b)] as column loops, and the current loops in the $x - y$ plane [see Fig. 2.2(c)] as the joist loops. In particular, Fig. 2.2(a) illustrates the magnetic dipoles excited by normal incidence. Here, we define the normal incidence such that the incident wave vector k is along the z direction and the structure is periodic in the $x - y$ plane. This is the simplest configuration for fabrication with DLW, where the structures are grown on the substrate parallel to the $x - y$ plane, and subsequent optical characterization. Optical response under this configuration is polarization-independent in the $x - y$ plane. On the other hand, Fig. 2.2(b) illustrates the magnetic dipoles excited by TE-polarized laterally incident light. We define the lateral incidence such that the incident k -vector lies in the $x - y$ plane parallel to the substrate and the structure is periodic in the plane perpendicular to the k -vector. In this case, the TE-polarized light is described as the electromagnetic field with fixed electric field E along the z direction. In contrast, for the TM-polarized laterally incident light electric field E is replaced with H , as shown

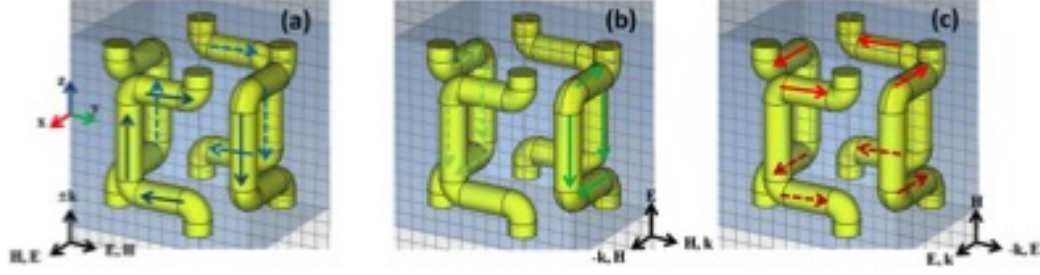


Figure 2.2: Schematics of three different magnetic dipoles excited inside the unit cell of the metamaterial under different incidences of light. Arrows indicate magnetic dipole loop currents induced by (a) normally incident light, (b) laterally incident TE-polarized light, and (c) laterally incident TM-polarized light. [Reprinted/Adapted] with permission from ref [1], [Optical Society of America].

in Fig. 2.2(c), where the corresponding magnetic dipoles are also illustrated.

A. Effective parameters and field distributions for different incidences of light

In this part, we verify the induced magnetic dipoles illustrated schematically in Fig. 2.2 based on calculated current density distributions and show the results for the retrieved effective optical parameters for single-layer metamaterial structures.

First, we consider the configuration in Fig. 2.2(a) where the structure interacts with normally incident light. Figure 2.3(a) shows the resultant transmittance (T), reflectance (R), and absorbance (A). In Fig. 2.3(b), we plot the retrieved effective refractive index, $n = n' + in''$. Retrieved effective permittivity, $\epsilon_y = \epsilon'_y + i\epsilon''_y$, and permeability, $\mu_x = \mu'_x + i\mu''_x$, are shown in Figs. 2.3(c) and 2.3(d), respectively. Notice that a magnetic resonance with a Lorentzian-like lineshape [140, 141] [see Fig. 2.3(d)]

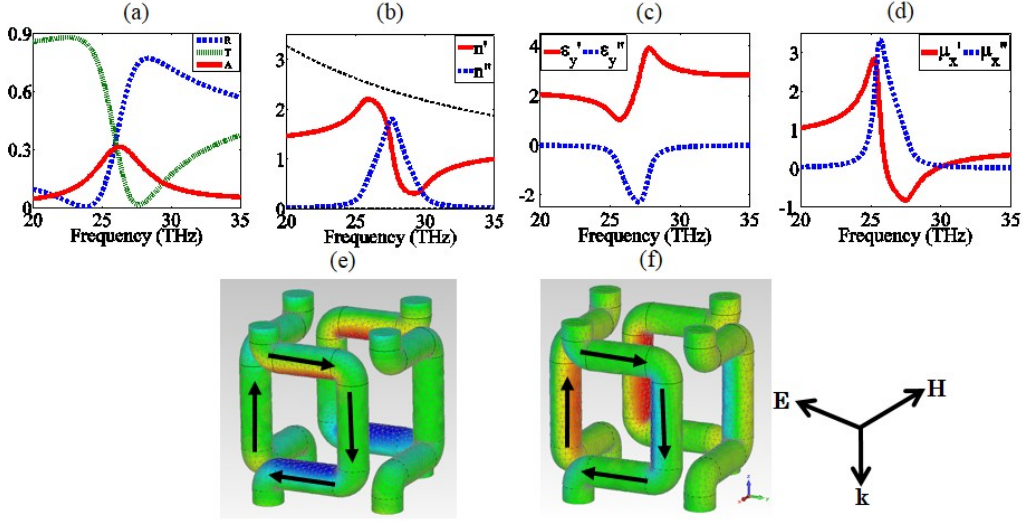


Figure 2.3: (a) Transmittance (T), reflectance (R), and absorbance (A) spectra for normally incident light. The structure is periodic in the xy plane and has one layer along the z direction. Retrieved effective (b) refractive index, (c) permittivity, and (d) permeability. The dashed black line in (b) is the first Brillouin zone edge. (e) Current density distribution at $f = 27\text{THz}$. Colors show the y component of the current density J_y (i.e., red and blue correspond to the $+y$ and y directions, respectively). (f) The same as (e) except that colors show the z component of the current density J_z (i.e., red and blue correspond to the $+z$ and z directions, respectively). [Reprinted/Adapted] with permission from ref [1], [Optical Society of America].

appears around 26THz and μ'_x is negative between 26 and 30THz . The ratio of the vacuum wavelength to unit cell size in the propagation direction (i.e., λ/a ratio) is about 5 , which is reasonably large for homogeneous effective medium approximation, near the magnetic resonance. Figures 2.3(e) and 2.3(f) show the current density distribution at $f = 27\text{THz}$ (i.e., near the magnetic resonance frequency). Arrows overlaying the surface plots in Fig. 2.3(e) and (f) indicate the complete dipole loop current. Only one of the loops is shown for clarity [see Fig. 2.2(a) for the location of other loop]. This verifies the column loops illustrated in Fig. 2.2(a).

When the structure interacts with laterally incident light such as in Figs. 2.2(b) and 2.2(c), then two other magnetic resonances originate depending on the polarization of incident light. Figure 2.4 shows the case for the TE-polarized light. There exists magnetic resonance around 22THz. In this case, the λ/a ratio is also about 5. The resultant current density distribution is shown in Figs. 2.4(e) and 2.4(f). Arrows overlaying the surface plots in (e) and (f) indicate the complete dipole loop current. Only one of the loops is shown for clarity [see Fig. 2.2(b) for the location of other loop]. Finally, Fig. 2.5 shows the results for the TM-polarized light. Particularly, Figs. 2.5(e) and 2.5(f) show the current density distribution at 40THz near the magnetic resonance, which verifies the joist loops illustrated in Fig.2.2(c). For this case, the λ/a ratio is about 3. Although the structure might not seem to be sufficiently sub-wavelength under this configuration, we should note that the results are still reliable, because (i) no discontinuities are observed in the retrieved results and (ii) the retrieved refractive index is below the first Brillouin zone edge.

B.Hyperbolic dispersion

The magnetic dipoles discussed above can be used to obtain hyperbolic dispersion. As an example we choose the magnetic dipoles in Fig. 2.3. We start with considering the TE-polarized electromagnetic waves propagating in the xz plane. The electric field is fixed along the y direction. When the incident k -vector changes its direction from the z direction to the x direction, the corresponding incident field configuration

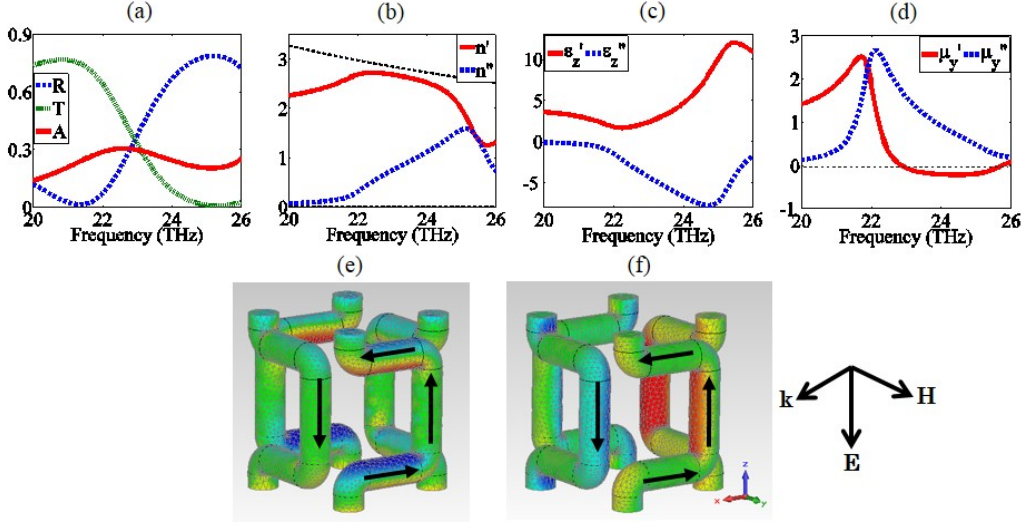


Figure 2.4: (a) Transmittance (T), reflectance (R), and absorbance (A) spectra for the TE-polarized laterally incident light. The structure is periodic in the yz plane and has one layer along the x direction. Retrieved effective (b) refractive index, (c) permittivity, and (d) permeability. The dashed black line in (b) is the first Brillouin zone edge. (e) Current density distribution at $f = 22\text{THz}$. Colors show the x component of the current density J_x (i.e., red and blue correspond to the $+x$ and x directions, respectively). (f) The same as (e) except for J_z . [Reprinted/Adapted] with permission from ref [1], [Optical Society of America].

changes from Figs. 2.3-2.5. Therefore, one might expect hyperbolic dispersion around the region where $\mu'_x < 0$ [see Fig. 2.3(d)] since $\mu'_z > 0$ in the same region. In order to demonstrate the hyperbolic dispersion relation, we calculate the tangential and normal components of the effective wave vector inside the metamaterial which are defined as k_x and k_z , respectively. The inverted Fresnel formula [138, 142] is used to obtain k_z :

$$k_z d = \pm \cos^{-1} \left(\frac{1 - r^2 + t^2}{2t} \right) + 2\pi m \quad (2.1)$$

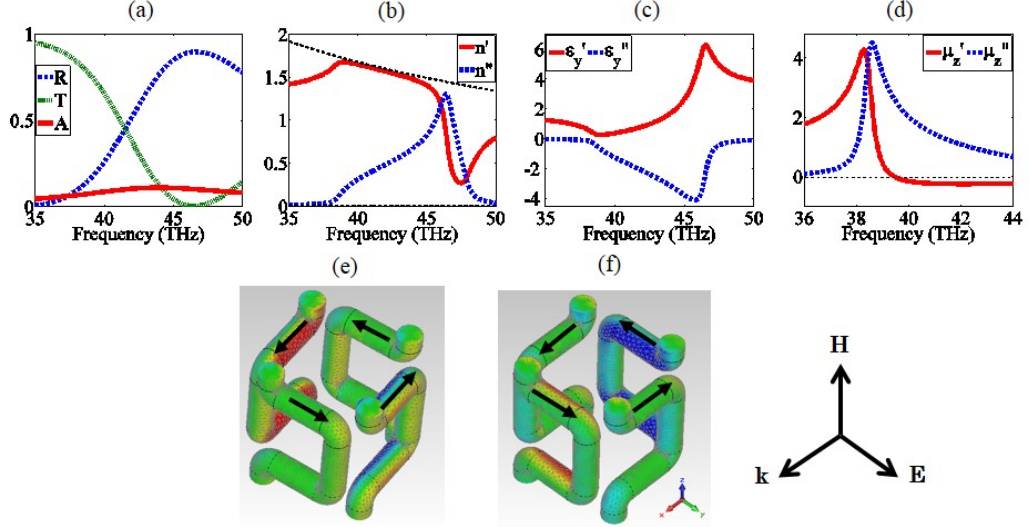


Figure 2.5: (a) Transmittance (T), reflectance (R), and absorbance (A) spectra for the TM-polarized laterally incident light. The structure is periodic in the yz plane and has one layer along the x direction. Retrieved effective (b) refractive index, (c) permittivity, and (d) permeability. The dashed black line in (b) is the first Brillouin zone edge. (e) Current density distribution at $f = 40\text{THz}$ for (e) J_x and (f) J_y . Arrows overlaying the surface plots in (e) and (f) indicate the complete dipole loop current. Only one of the loops is shown for clarity [see Fig. 2.2(c) for the location of other loop]. [Reprinted/Adapted] with permission from ref [1], [Optical Society of America].

where d is the unit cell thickness along the propagation direction. r and t are the reflection and transmission coefficients, respectively. m is the branch number. The sign is chosen to guarantee a positive imaginary part of k_z and m is selected to promise a continuous real part of k_z . On the other hand, at the vacuum-metamaterial interface the tangential components of the wave vectors are continuous. Thus, k_x can be expressed as $k_x = k_0 \sin\theta$, where k_0 is the wave number in free space and θ is the angle of incidence with respect to the surface normal. Different angles of incidence are set up in the CST simulations and corresponding reflection and transmission coefficients along with k_x values are obtained. k_z values are then calculated from

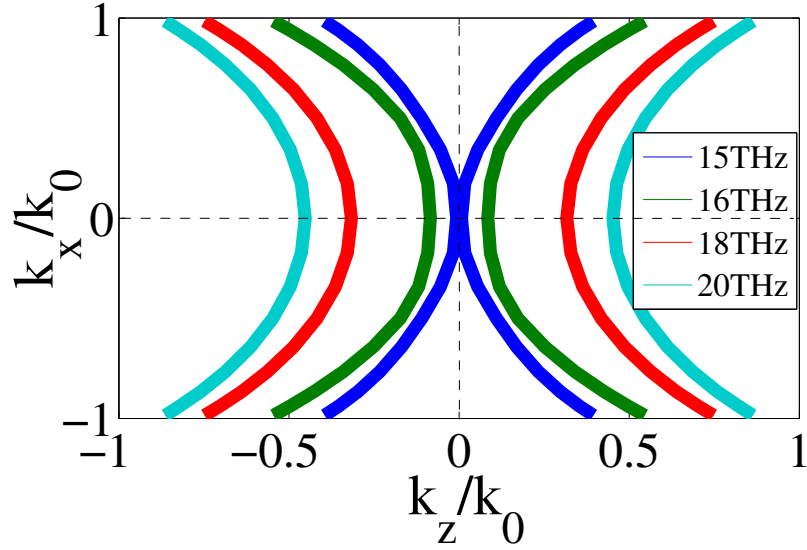


Figure 2.6: Equipfrequency contours for the TE-polarized light propagating in the xz plane show hyperbolic dispersion. The structure is periodic in the xy plane and has five layers along the z direction. [Reprinted/Adapted] with permission from ref [1], [Optical Society of America].

Eq. 2.1. Finally, based on different pairs of k_z and k_x , we obtain the equipfrequency contours describing the dispersion for the metamaterial.

The equipfrequency contours for a one-layer structure (i.e., single unit cell along the z direction and infinite in the xy plane) gives elliptical dispersion contrary to anticipated hyperbolic dispersion due to the contribution of relatively large imaginary parts of effective optical parameters. However, increasing the number of layers of the proposed metamaterial structure leads to a transition from elliptical dispersion to hyperbolic dispersion. For example, the equipfrequency contours in Fig. 2.6 correspond to the five-layer structure (i.e., five unit cells along the z direction and infinite in the xy plane) which manifests hyperbolic dispersion. The blue, green, red, and cyan lines

represent the frequencies of 15, 16, 18, and 20THz, respectively.

2.3.3 Discussion

The metamaterial structures, here, were designed specifically for fabrication with DLW processes and subsequent metalization. The functional optical metamaterials resulting from this fabrication approach are usually free-standing structures in air [104, 115, 143]. Therefore, vacuum was selected as a background material in our simulations. Direct metalization in the dielectric host media using DLW is also possible [144, 145]. However, no functional optical metamaterial with this approach has been shown.

If the meandering wires are embedded in a dielectric media with a larger refractive index than vacuum, we find that the resonances and effective material properties redshift. Therefore, it is expected that the hyperbolic dispersion should also redshift with a larger refractive index. Considering the underlying resonant magnetic dipole modes (see Fig. 2.2) the redshift in magnetic resonances in Figs. 2.3-2.5, for example, can be easily explained by a simple LC circuit model [19, 140, 146]. Effectively, the meandering wires in Figs. 2.3 and 2.4 behave similar to a two-gap split-ring resonator (SRR) and the meandering wires in Fig. 2.5 behave similar to a four-gap SRR. Embedding these SRR-like structures inside host media with a larger refractive

index than vacuum results in an increase in equivalent circuit capacitance, hence a redshift in resonance frequency.

The origin of resultant commonly observed negative imaginary parts in the retrieved constitutive parameters under the HEM approximation has been extensively investigated [147, 148]. It was shown that these negative imaginary parts near the resonances arise from the inherent periodicity of the metamaterial if the actual periodic metamaterial structure is approximated by a HEM with the same scattering parameters as the periodic structure [147, 149]. However, every inhomogeneous medium exhibits spatial dispersion (i.e., polarization and magnetization at a given location depends on the spatial distribution of the fields) [150], which is not considered in the HEM approximation. Further studies have shown that the incorporation of spatial dispersion improves the accuracy of the effective parameter retrieval procedure by removing the periodicity artifacts such as negative imaginary parts in constitutive parameters [150, 151, 152].

Finally, in Fig. 2.7 we plot in the same graph the effective permeability values corresponding to three different magnetic dipoles illustrated in Fig. 2.2 and studied in Figs. 2.3-2.5. It is worth mentioning that three effective permeability values intersect nontrivially around 40THz (i.e., convergence below 20THz is uninteresting due to asymptotic nonmagnetic response at low frequencies). This shows that the structure has potential for three-dimensionally isotropic permeability despite geometric

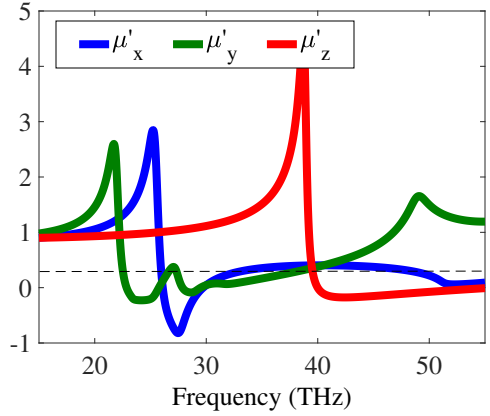


Figure 2.7: Real parts of the effective magnetic permeability in the same graph corresponding to three different magnetic dipoles studied in Figs. 2.3 –2.5. The curves intersecting around 40THz show potential for nontrivial three-dimensionally isotropic permeability. [Reprinted/Adapted] with permission from ref [1], [Optical Society of America].

anisotropy.

Despite operating at a single frequency, considering the difficulty of making isotropic metamaterials at optical frequencies, this result is still interesting. Moreover, the structure may be optimized to operate over a wider band gap. Tunability with the incorporation of, for example, liquid crystals [153, 154] can also be utilized to mitigate the bandwidth issue.

2.3.4 Fabrication with STED-DLW

The whole process to fabricate this hyperbolic metamaterial is expressed in ref [155]. Firstly, by using STED-DLW, an array of hollow meandering wires in a block of polymer is obtained. The next step is to infill this template by electrochemical deposition of gold. After removing the polymer by plasma etching, an array of free-standing 3D meandering wires is realized. The hollow meandering wire template has been fabricated by Dr. Martin Wegener's research group in Germany shown in Fig. 2.8. The parameters of template are close to the ones shown in Fig. 2.1 except the gap size between two adjacent meandering wires, which is 202nm in Fig. 2.1. 202nm is quite close to the fabrication limitations, which leads to current fabrication challenge.

2.4 Hollow waveguides with negative index metamaterial cladding

The ability to delay or stop the light pulse could open the door to a range of new applications in optical buffering [156] and quantum information processing [157, 158, 159, 160, 161]. There are various methods to achieve slow and even stopped light, including electromagnetically induced transparency [162, 163], photonic crystal

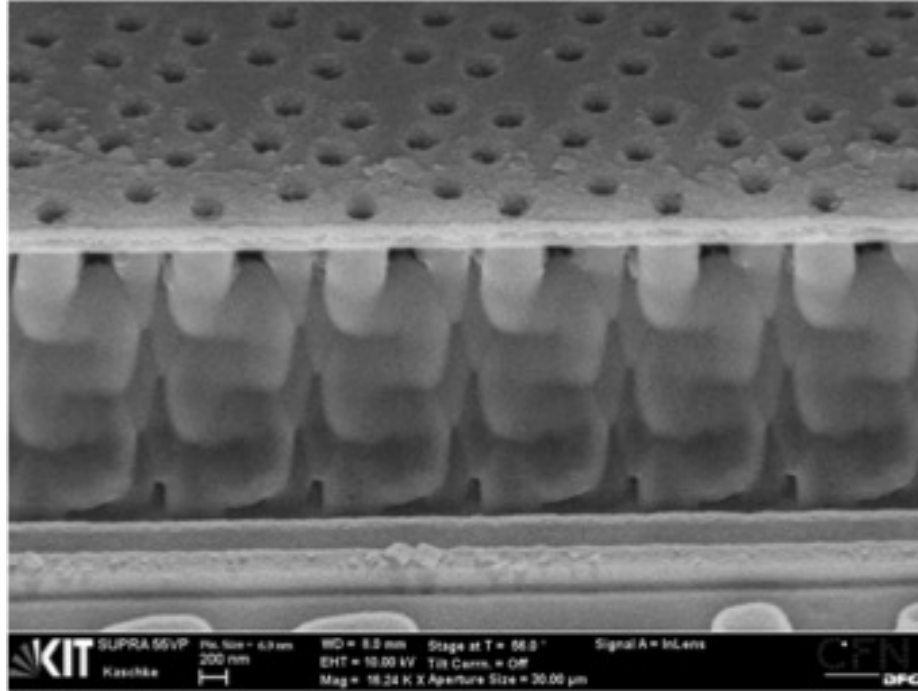


Figure 2.8: SEM image for hollow meandering wire template (with permission from Dr. Martin Wegener)

waveguides [164, 165], coherent population oscillations [166], atomic double resonances [167], and stimulated Brillouin scattering in optical fibers [168]. However, in many of these methods, the issues of optical device integration and/or room temperature operation need to be addressed.

With the advances in metamaterial design and fabrication, the possibility of unusual wave propagation phenomena including simultaneously negative group and phase velocity [169, 170, 171] and especially slow and stopped light under room temperature received much attention [172, 173, 174, 175, 176]. In 2007, Tsakmakidis et al. proposed a tapered waveguide with negative index core and positive index cladding to stop different frequency components of a pulse at different waveguide thickness,

resulting in so-called "trapped rainbow" effect [174]. The electromagnetic waves, which experience negative Goos-Hanchen shift at the core-cladding interface [177], lead to slow group velocity. When the waveguide thickness decreases to the critical thickness, the group velocity eventually becomes 0, and thus the waves are trapped inside the waveguide. However in Tsakmakidis et al. [174] and other theoretical studies [172, 173, 175, 176, 178], lossless metamaterials are assumed. The material loss in the realistic optical metamaterials can be detrimental for the guided modes [54], which attenuate along the waveguide axis and eventually disappear. Thus, the stopped light may be difficult to observe in practical metamaterial waveguides at optical wavelengths. Nevertheless, the stopped light is experimentally demonstrated at microwave frequency [179, 180], where the absorption loss is much smaller compared to optical frequencies. The experimentally demonstrated stopped light working at an optical frequency is hardly found in the literature. Interestingly, a hyperbolic metamaterial waveguide made of lossy materials has been proposed and numerically validated at optical frequencies [181]. However, the effective permittivities for the designed hyperbolic metamaterial are $\epsilon_x = -25 + i0.25$ and $\epsilon_z = 5 + i0.05$. The figure of merit (FOM), defined as $|\epsilon'/\epsilon''|$, for this metamaterial is 100, which is not easy for practical realization. Prime and double prime indicate real and imaginary parts, respectively.

In this section, we consider one negative index structure [182], which is relatively feasible for fabrication using direct laser writing technique, as an example and show

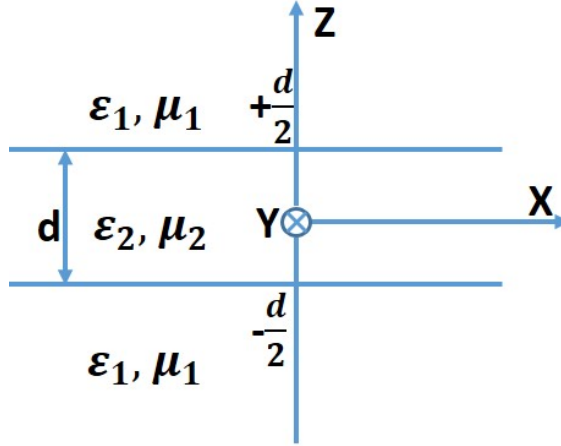


Figure 2.9: Schematic geometry of a symmetric slab waveguide

that with realistic losses in the metamaterials, the stopped light effect is hard to achieve. The remaining part of the section is organized as follows. In section 2.4.1, first the analytical dispersion equations for the hollow waveguide with the negative index cladding will be derived. Then, by importing the effective optical parameters of the negative index structure in [182], the dispersion relation and the group velocity will be obtained. In section 2.4.2, we will verify the analytical results with the finite element and finite-difference-time-domain methods using COMSOL and Lumerical commercial software packages.

2.4.1 Analytical analysis

A. Mode analysis

A three-layer slab waveguide is shown in Fig. 2.9. The claddings are negative index

metamaterials with relative permittivity ϵ_1 and relative permeability μ_1 . The core layer is air with $\epsilon_2 = 1$, $\mu_2 = 1$, and the layer thickness is d . Here we assume transverse electric (TE) polarization (i.e., field components E_y , H_x , and H_z). The results for transverse magnetic polarization can be easily obtained from the duality principle. The time-harmonic form of Maxwell's equations $\vec{\nabla} \times \vec{E} = -j\omega \vec{B}$ and $\vec{\nabla} \times \vec{H} = j\omega \vec{D}$ can be written as:

$$\vec{\nabla} \times \vec{E} = \begin{vmatrix} \hat{x} & \hat{y} & \hat{z} \\ \frac{\partial}{\partial x} & \frac{\partial}{\partial y} & \frac{\partial}{\partial z} \\ 0 & E_y & 0 \end{vmatrix} = -\frac{\partial E_y}{\partial z} \hat{x} + \frac{\partial E_y}{\partial x} \hat{z} \quad (2.2)$$

$$\vec{\nabla} \times \vec{H} = \begin{vmatrix} \hat{x} & \hat{y} & \hat{z} \\ \frac{\partial}{\partial x} & \frac{\partial}{\partial y} & \frac{\partial}{\partial z} \\ H_x & 0 & H_z \end{vmatrix} = \frac{\partial H_z}{\partial y} \hat{x} + \left(\frac{\partial H_x}{\partial z} - \frac{\partial H_z}{\partial x} \right) \hat{y} - \frac{\partial H_x}{\partial y} \hat{z} \quad (2.3)$$

$$j\omega \vec{D} = j\omega \epsilon_0 \epsilon_r E_y \hat{y} \quad (2.4)$$

$$j\omega \vec{B} = j\omega \mu_0 \mu_r (H_x \hat{x} + H_z \hat{z}) \quad (2.5)$$

Then we obtain three coupled equations corresponding to x , y , z components, respectively:

$$\begin{cases} j\omega\mu_0\mu_r H_x = \frac{\partial E_y}{\partial z} \\ j\omega\mu_0\mu_r H_z = \frac{\partial E_y}{\partial x} = j\beta E_y \\ j\omega\epsilon_0\epsilon_r E_y = \frac{\partial H_x}{\partial z} - \frac{\partial H_z}{\partial x} = \frac{\partial H_x}{\partial z} - j\beta H_z \end{cases} \quad (2.6)$$

Where β is the propagation constant along the x direction. Eliminating H_x and H_z in Eq. 2.6, and using the free space relations $c_0 = 1/\sqrt{\epsilon_0\mu_0}$, $k_0 = 2\pi/\lambda_0 = 2\pi/(c_0/f) = \omega/c_0$, we obtain

$$\frac{\partial^2 E_y}{\partial z^2} + (k_0^2\epsilon_r\mu_r - \beta^2)E_y = 0 \quad (2.7)$$

which only contains the E_y component. Then, the solution of Eq. 2.7 for the symmetric waveguide has the form,

$$E_y = \begin{cases} Ae^{jk_{z1}(z-\frac{d}{2})}, z \geq \frac{d}{2} \\ Be^{jk_{z2}z} + Ce^{-jk_{z2}z}, |z| \leq \frac{d}{2} \\ De^{-jk_{z1}(z+\frac{d}{2})}, z \leq -\frac{d}{2} \end{cases} \quad (2.8)$$

Where k_{z1} and k_{z2} are transverse wave numbers in cladding and core, respectively.

They satisfy the dispersion relation:

$$\begin{cases} k_{z1}^2 + \beta^2 = k_0^2 \epsilon_1 \mu_1 \\ k_{z2}^2 + \beta^2 = k_0^2 \epsilon_2 \mu_2 \end{cases} \quad (2.9)$$

Based on Eq. 2.6, H_x can be expressed as:

$$H_x = \begin{cases} \frac{jk_{z1}}{j\omega\mu_0\mu_1} A e^{jk_{z1}(z-\frac{d}{2})}, z \geq \frac{d}{2} \\ \frac{jk_{z2}}{j\omega\mu_0\mu_2} (B e^{jk_{z2}z} - C e^{-jk_{z2}z}), |z| \leq \frac{d}{2} \\ \frac{-jk_{z1}}{j\omega\mu_0\mu_1} D e^{-jk_{z1}(z+\frac{d}{2})}, z \leq -\frac{d}{2} \end{cases} \quad (2.10)$$

E_y and H_x should be continuous at $z = \pm\frac{d}{2}$ to satisfy the boundary conditions resulting in

$$\begin{cases} A = B e^{jk_{z2}\frac{d}{2}} + C e^{-jk_{z2}\frac{d}{2}} \\ D = B e^{-jk_{z2}\frac{d}{2}} + C e^{jk_{z2}\frac{d}{2}} \end{cases} \quad (2.11)$$

$$\begin{cases} \frac{k_{z1}}{\mu_1} A = \frac{k_{z2}}{\mu_2} B e^{jk_{z2} \frac{d}{2}} - \frac{k_{z2}}{\mu_2} C e^{-jk_{z2} \frac{d}{2}} \\ \frac{-k_{z1}}{\mu_1} D = \frac{k_{z2}}{\mu_2} B e^{-jk_{z2} \frac{d}{2}} - \frac{k_{z2}}{\mu_2} C e^{jk_{z2} \frac{d}{2}} \end{cases} \quad (2.12)$$

For the TE even modes $A = D$, hence $B = C$. Then, based on Eqs. 2.11 and 2.12, we obtain $\cos(\frac{k_{z2}d}{2}) = \frac{A}{2B}$, and $\sin(\frac{k_{z2}d}{2}) = -\frac{j\mu_2 k_{z1}}{\mu_1 k_{z2}} \frac{A}{2B}$. On the other hand, for the TE odd modes, $A = -D$, hence $B = -C$. Then, we obtain $\sin(\frac{k_{z2}d}{2}) = -\frac{jA}{2B}$, and $\cos(\frac{k_{z2}d}{2}) = \frac{\mu_2 k_{z1}}{\mu_1 k_{z2}} \frac{A}{2B}$. As a result, we obtain the dispersion equations

$$\begin{cases} \tan(\frac{k_{z2}d}{2}) = -\frac{j\mu_2 k_{z1}}{\mu_1 k_{z2}} \text{ for even mode} \\ \cot(\frac{k_{z2}d}{2}) = \frac{j\mu_2 k_{z1}}{\mu_1 k_{z2}} \text{ for odd mode} \end{cases} \quad (2.13)$$

which can be expressed in more compact form as

$$\frac{k_{z2}d}{2} + \frac{m\pi}{2} = \arctan\left(-\frac{j\mu_2 k_{z1}}{\mu_1 k_{z2}}\right) \quad (2.14)$$

where $m = 0, 1, 2, 3, \dots$

Since the cladding is a negative refractive index structure, there will be not only waveguide modes confined to the waveguide core, but also surface modes residing at the core-cladding interfaces of the waveguide. Next, we will investigate these two

types of modes.

A. 1. Waveguide modes confined to the core

Similar to the regular dielectric waveguide, the modes confined to the waveguide core have the following characteristics. Electromagnetic waves along the z direction form standing waves inside the core while attenuate inside the cladding. Here, we use the notation β_w , $k_{z1,w}$, and $k_{z2,w}$ to describe the propagation constant, transverse wavenumbers in the cladding and core, respectively. Since the absorption loss is considered in the structure, all the wavenumbers are complex. From Eq. 2.9, the transverse wavenumbers satisfy the equations $k_{z1,w} = \pm j\sqrt{\beta_w^2 - k_0^2\epsilon_1\mu_1}$, $k_{z2,w} = \pm\sqrt{k_0^2\epsilon_2\mu_2 - \beta_w^2}$. That the imaginary parts of the wavenumbers are positive for passive materials fixes the sign. Then by using the effective refractive index for the waveguide mode $n_{eff,w} = \beta_w/k_0$, $k_{z1,w}$ and $k_{z2,w}$ can be written as

$$\begin{cases} k_{z1,w} = \pm jk_0\sqrt{n_{eff,w}^2 - \epsilon_1\mu_1} \\ k_{z2,w} = \pm k_0\sqrt{\epsilon_2\mu_2 - n_{eff,w}^2} \end{cases} \quad (2.15)$$

Eq. 2.15 can be substituted into Eq. 2.14 to express the dispersion relation in terms of $n_{eff,w}$ and k_0d .

A. 2. Surface modes confined to the core-cladding interface

The surface plasmon polaritons (SPP) appear at the interface between positive and negative index materials [183]. The surface mode has an evanescent behavior in both core and cladding. Here, we use the notation β_s , $k_{z1,s}$ and $k_{z2,s}$ to describe the propagation constant, transverse wavenumbers in the cladding and core, respectively. From Eq. 2.9, $k_{z1,s} = \pm j\sqrt{\beta_s^2 - k_0^2\epsilon_1\mu_1}$, and $k_{z2,s} = \pm j\sqrt{\beta_s^2 - k_0^2\epsilon_2\mu_2}$. By using the effective refractive index for the surface mode $n_{eff,s} = \beta_s/k_0$, we obtain

$$\begin{cases} k_{z1,s} = \pm jk_0\sqrt{n_{eff,s}^2 - \epsilon_1\mu_1} \\ k_{z2,s} = \pm jk_0\sqrt{n_{eff,s}^2 - \epsilon_2\mu_2} \end{cases} \quad (2.16)$$

Similar to the waveguide modes in the previous section, the dispersion relation for the surface modes can be also expressed in terms of $n_{eff,s}$ and k_0d using Eq. 2.14 and Eq. 2.16.

B. Slow and stopped light in the hollow waveguide with a negative index cladding

Having derived the dispersion equations for waveguide and surface modes above, we select the negative index structure in [182] as the cladding. The structure consists of two pairs of meandering wires with inversion symmetry. The simultaneously negative ϵ and μ are determined by the effective plasma frequency and the magnetic resonance of the wires, respectively. Retaining bulk optical properties, the structure

is particularly suitable for carving into a volume metadvice such as a waveguide here. The vertical connectivity between of the structure offers important potential for possible realization with direct laser writing processes, a low-cost and rapid prototyping approach for truly 3D fabrication. The lattice constant for the square lattice of the structure is $364nm$. All the other geometric parameters can be found in [182]. The negative refractive index appears in the region between $140THz$ and $180THz$. Since the core is air, the total internal reflection condition requires $|Re(n_1)| < n_2$, where $n_2 = 1$ is the refractive index of air. To simplify the calculations, we first considered the cladding as a non-dispersive material with $\epsilon_1 = -0.419 + i0.062$, $\mu_1 = -0.914 + i0.256$, and $n_1 = -0.370 + i0.128$, which indeed correspond to the effective optical parameters of the negative index structure at a specific frequency of $172THz$.

We start with analyzing three different cases: (1) *lossy* case using the above effective parameters for ϵ_1 and μ_1 , (2) *less lossy* case where the imaginary parts of ϵ_1 and μ_1 are reduced by 10%, i.e., $\epsilon_1 = -0.419 + i0.0062$, $\mu_1 = -0.914 + i0.0256$, and (3) *lossless* case where the imaginary parts are completely removed, i.e., $\epsilon_1 = -0.149$, $\mu_1 = -0.914$. Using Eqs. 2.14-2.16, we plot in the left column of Fig. 2.10 the real part of the effective refractive index n'_{eff} versus the reduced slab thickness k_0d , for both surface modes and waveguide modes, respectively. An iterative process was used to generate the plots. Since n_{eff} is in general a complex number, for a particular mode m , we first fixed the value of n'_{eff} and determined the corresponding n''_{eff} . The correct

value of n''_{eff} was found after several iterations at the point where the imaginary part of k_0d approached to 0 since k_0 is real. It was assumed that $0 \leq n''_{eff} \leq n'_{eff}$. The process was repeated with different incremented values of n'_{eff} until the complete plot in Fig. 2.10 was obtained. The figure shows the first three waveguide modes, TE_1 , TE_2 , TE_3 and two surface modes SPP_0 , SPP_1 . In contrast with regular planar dielectric waveguides, here we notice that $m = 0$ mode is not supported in this waveguide with the negative index cladding. Also the TE_1 mode tends to have a finite bandwidth.

The dispersion diagrams in the *less lossy* case with 10% reduced imaginary parts are very close or almost identical to the *lossless* case. However, greater difference in dispersion diagrams is observed between the *lossy* case and *lossless* case. In a lossy medium, the group velocity v_g is defined as

$$v_g = \frac{d\omega}{d\beta'} = c_0 \frac{dk_0}{d(k_0 n'_{eff})} = \frac{c_0}{n'_{eff} + k_0 d \left[\frac{d(n'_{eff})}{d(k_0 d)} \right]} \quad (2.17)$$

The stopped light appears at $v_g = 0$, which means that it can be obtained at the point where the dispersion diagram has an infinite slope. Therefore, TE_2 and TE_3 modes have potential to stop in the waveguide.

Now, we choose a particular mode TE_2 to study the stopped light behavior in the

presence of losses. In the *lossless* and *less lossy* case, from Fig. 2.10 the stopped light is expected at the reduced slab thickness $k_0 d = 6.32$. Thus, at $172THz$ the light will be trapped at the critical waveguide thickness $d = 1.76\mu m$. However, the scenario for the *lossy* case is less obvious. Using Eq. 2.17 with $d = 1.76\mu m$, we obtain the plots in center column of Fig. 2.10 for the three different cases. The top panel depicts the real part of propagation constant β'_w versus frequency, while the bottom panel illustrates the normalized group velocity v_g/c_0 versus frequency. In the *lossless* and *less lossy* cases above $172THz$, two TE_2 modes with different propagation constants and group velocities can exist. One mode has positive group velocity, while the other one has negative. This indicates that above $172THz$, while one mode is forward propagating, the other mode is backward propagating. At $172Thz$, the two modes merge into a single mode which is ultimately trapped inside the waveguide. Based on the group velocity plots, it is clear that the light stops at $f = 172THz$ in both *lossless* and *less lossy* cases. However, in the *lossy* case, only one propagating mode exists in the waveguide with the positive group velocity which approaches to 0 at $171.3THz$. The absence of the mode with negative group velocity hints at the difficulty of stopping the light in the *lossy* case.

The right column of Fig. 2.10 plots the attenuation coefficient $\alpha = 2\beta'' = 2n''_{eff}k_0$. In the *less lossy* case, $0.04 < \alpha < 0.08$, which is different for forward and backward modes. Away from the stopped light frequency, the attenuation for the backward mode is larger than the forward mode, while in the *lossy* case, $0.25 < \alpha < 0.50$,

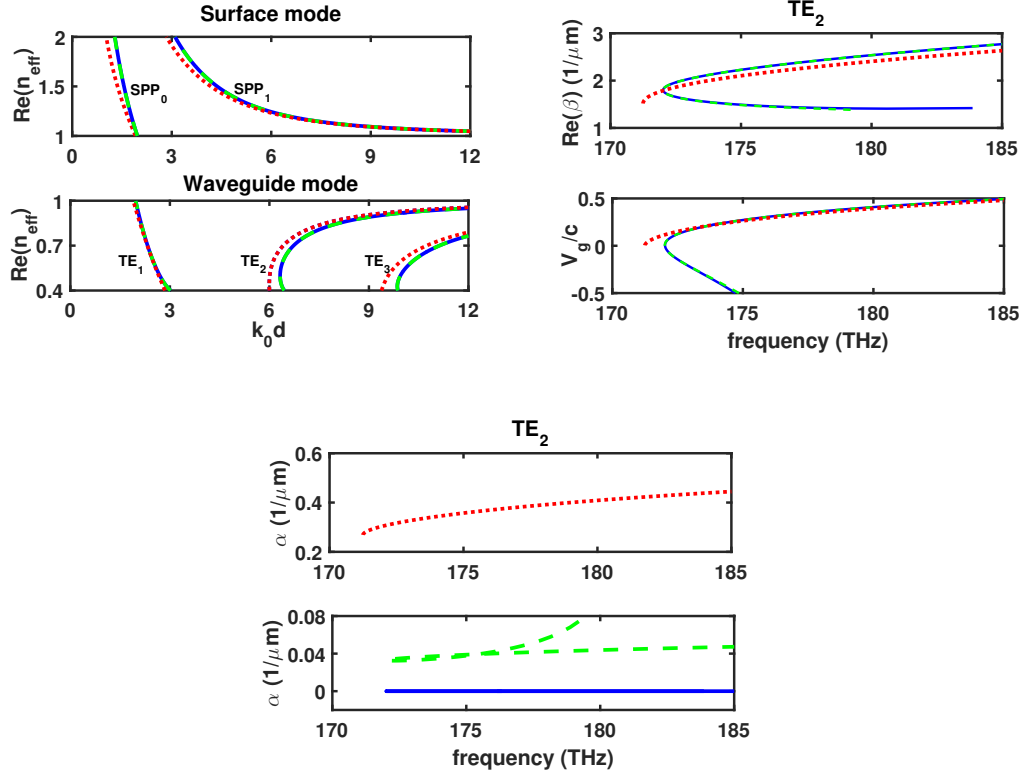


Figure 2.10: Left: n_{eff} versus k_0d for surface modes and waveguide modes, Center: dispersion diagrams of TE_2 mode, and Right: attenuation of TE_2 mode under three different cases. Solid blue line, dash green line and dot red line correspond to *lossless*, *less lossy*, and *lossy* cases, respectively.

which is much larger compared to *less lossy* case. Since the attenuation for the backward mode is higher than the forward mode in the *lesslossy* case, it should not be surprising why the backward mode disappears in the dispersion diagram of the *lossy* case. As we will investigate in the next section, if the attenuation in the *lossy* case is faster than the light compression, it becomes difficult to observe the stopped light inside the waveguide.

2.4.2 Numerical analysis

A. Frequency domain simulations for the dispersion diagram

To verify the analytical calculations of the dispersion relations, we performed eigenmode simulations using COMSOL Multiphysics software package to obtain the dispersion diagrams for the hollow waveguide. Here, we considered the *lossy* case with the same non-dispersive homogeneous waveguide cladding as above. The eigenmode solver calculates the mode effective refractive index n_{eff} at different frequencies. By inspecting the field distribution, we distinguish n_{eff} , hence the propagation constant from $\beta = n_{eff}k_0$ for the waveguide and surface modes. Fig. 2.11 compares the analytical and numerical dispersion relations for both surface SPP₁ and the waveguide TE₂ modes. The left column corresponds to β' versus frequency and the right one corresponds to the attenuation coefficient α versus frequency. It is clear that the numerical results agree very well with the analytical results for both the surface and waveguide modes.

B. Time domain simulations for the slow and stopped light

We designed a linearly tapered waveguide to further investigate the slow and stopped light phenomena. The geometry of the tapered waveguide is shown in Fig. 2.12. We used the FDTD Solutions module of the Lumerical software package in this section

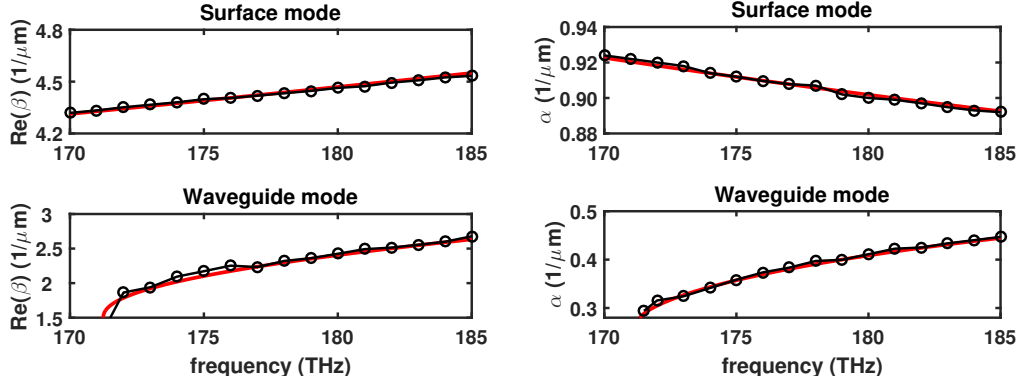


Figure 2.11: Numerical result comparing with analytical result. Solid red line represents analytical result, and black circle marker represents numerical result.

to simulate the light propagating in the waveguide. Perfect matched layer (PML) boundary conditions were applied to the boundaries of the computational domain perpendicular to the x and z directions. Periodic boundary conditions (PBCs) were used in the y direction. The light enters the waveguide from the wide input port with $2.8\mu m$ air core thickness, which is reduced down to $0.8\mu m$ at the exit. The total length of the waveguide is $80\mu m$. Having calculated the eigenmodes supported by the waveguide, the TE_2 mode was injected into the waveguide. Firstly, we design the cladding as a homogeneous structure with the center frequency of $172THz$ and the bandwidth of $2.2THz$. To investigate the influence of losses, we first assumed that the cladding is a homogeneous non-dispersive material similar to the analytical calculations above and considered again the three cases, i.e., *lossless*, *less lossy*, and *lossy*.

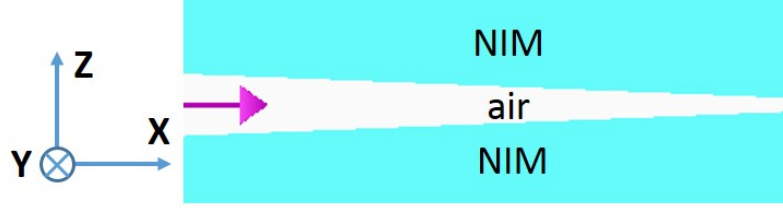


Figure 2.12: Geometry of a linearly tapered waveguide with negative index material (NIM) cladding. Purple arrow indicates the propagation direction.

Fig. 2.13 shows the snapshots of the electric fields E_y in the waveguide at different times. When the waveguide mode propagates along the tapered waveguide, the group velocity continuously decreases [see the dispersion curve for the TE_2 mode in Fig. 2.10]. Therefore, the rear part of the light pulse travels faster than the front part, and as a result, the pulse experiences a spatial compression along the propagation direction. This occurs in all the three cases. In the *lossless* and *less lossy* cases, when the group velocity decreases to 0 at the critical thickness $1.75\mu m$ (close to analytical thickness $1.76\mu m$), the pulse is extremely compressed into a small region and stopped. However, the stopped light cannot survive at the critical thickness for a long time mainly due to the backward scattering. For the *lossy* case, the mode attenuation occurs much faster than the mode compression. Thus, we cannot trap the light inside the waveguide. This is not surprising given the attenuation coefficients shown in the top and bottom panels of Fig. 2.10.

Next, instead of the homogeneous non-dispersive cladding, we directly simulated the waveguide with the inhomogeneous dispersive negative index structure in [182] as the cladding to compare the results. The designed waveguide geometry is shown in

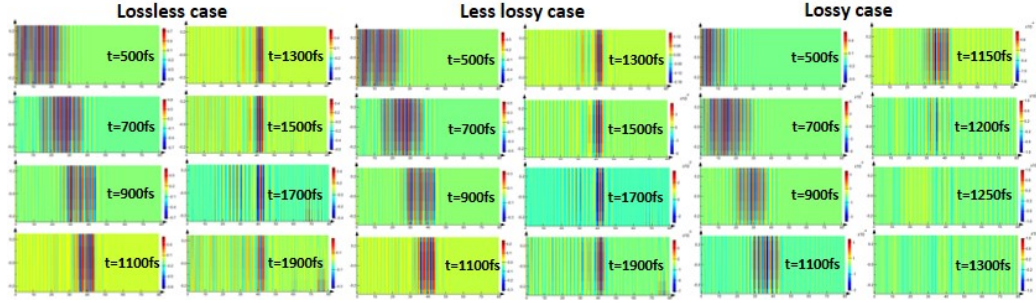


Figure 2.13: Snapshots of the propagation of the pulse at different moments for *lossless* case, *less lossy* case and *lossy* case, respectively.

Fig. 2.14(a). There are 20 periods of unit cells in the x direction, and 3 periods in the z direction on each side in the cladding. The inset depicts the top view of the waveguide. The input port of the waveguide is $1.9\mu\text{m}$ thick and the exit port is $1.6\mu\text{m}$ thick. The PBCs were applied along the y direction, and PML boundary conditions were applied in the x and z directions. Again, the TE_2 pulse was injected into the tapered waveguide in Fig. 2.14(a) and the electric field distribution $|E_y|$ at different times were plotted in Fig. 2.14(b). Similar to the waveguide with the non-dispersive homogeneous cladding in the *lossy* case, when the pulse enters the waveguide, it rapidly attenuates before a significant compression. Thus, the light is dissipated due to the losses before it is trapped. Note that the pulse propagation behavior with the inhomogeneous and dispersive cladding material (see Fig. 2.14) is similar to the homogeneous and non-dispersive cladding material (see Figs. 2.12 and 2.13), because the latter has no appreciate change in the effective material parameters within the assumed pulse bandwidth. Since the FOM of the inhomogeneous negative index structure [182] is comparable to (or even higher at $n'_{eff} = -1$ than) many optical negative index metamaterial structures, the results here hints that it may be difficult

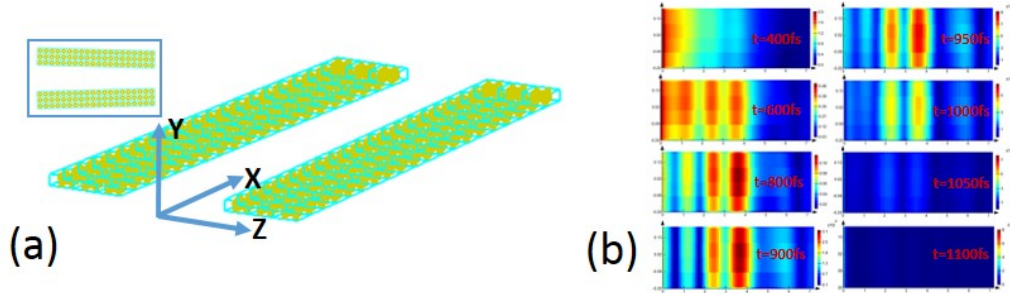


Figure 2.14: (a) Geometry of the designed waveguide with cladding made of practical structure. (b) snapshots of the electric field distribution at different moments

to observe stopped light behavior inside an optical waveguide with negative index cladding. This is true even if the mode confinement or trapping is inside the lossless core region, i.e., air. Furthermore, consistent with [54] these results strongly contrast with and challenge the originally proposed "trapped rainbow" idea [174] where the confinement was assumed inside a hypothetical lossless negative index metamaterial.

2.5 Direct laser metal writing technique

Although DLW provides an opportunity to create arbitrarily 3D structures, the technique is unable to produce vertically disconnected 3D structures, such as a volumetric array of metal dots. The disconnected metal dot [184] or metal rod [185] can create bulk optical metamaterial resonators. An option to fabricate disconnected metal features is direct laser metal writing technique [144]. When the laser comes to the

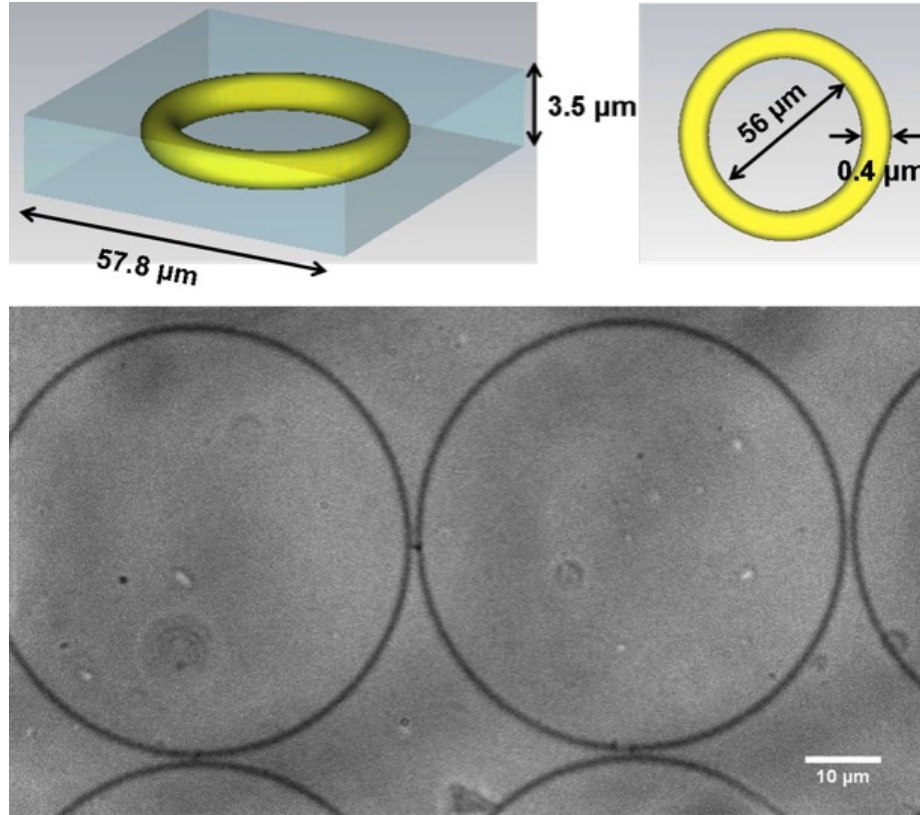


Figure 2.15: $56\mu\text{m}$ diameter silver rings that exhibits negative permittivity at $400\mu\text{m}$ wavelength. [Reprinted/Adapted] with permission from Kevin Vora.

focus, nonlinear light-matter interaction induces the metal-ion photoreduction process in a volume smaller than the diffraction limited focal spot, which initiates the metal nanoparticles growth. We designed two silver rings inside gelatin operating in the THz region, and obtained electric resonance in the ring and split ring, respectively. Kevin Vora of Dr. Eric Mazur's group at Harvard University fabricated these two structures. The results are shown in Fig. 2.15 and 2.16, which are reprinted from Kevin Vora's PhD dissertation [186] with permission from him. The designs are shown on the top line and the optical images of the fabricated structures are shown on the bottom line.

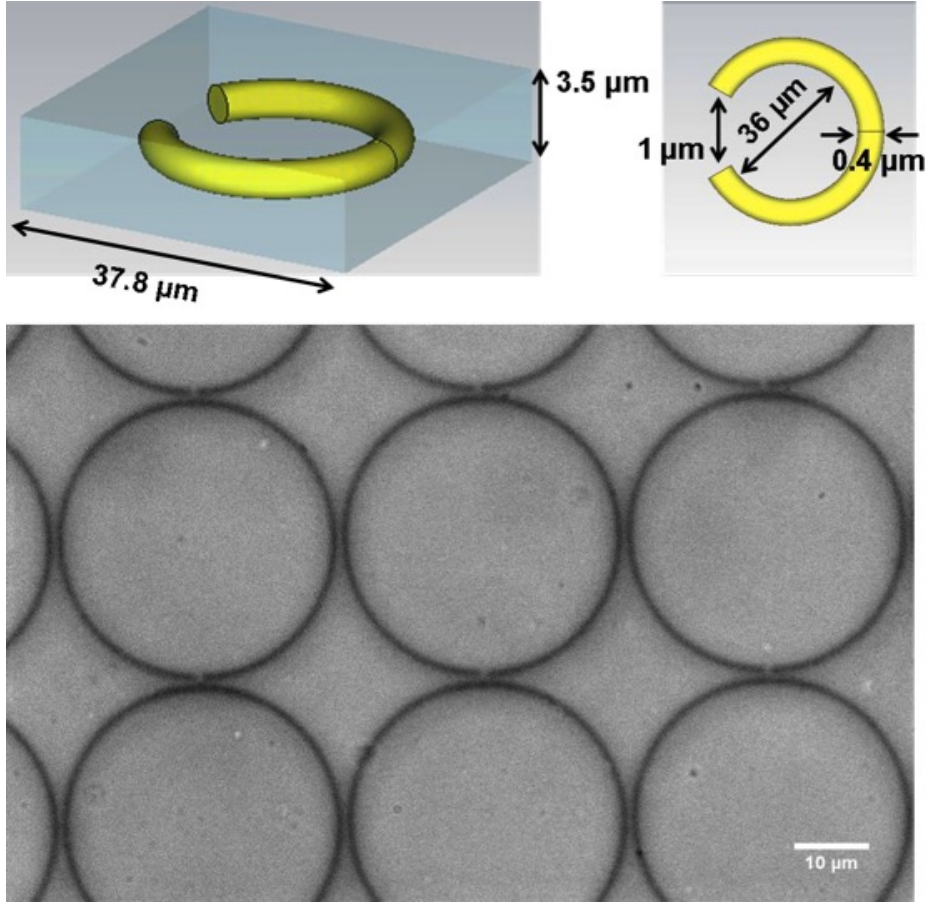


Figure 2.16: $36\mu\text{m}$ diameter silver split rings with $1\mu\text{m}$ gap size that exhibits negative permittivity at $400\mu\text{m}$ wavelength. [Reprinted/Adapted] with permission from Kevin Vora.

2.6 Conclusion

In summary, based on the vertical connectivity requirement, we propose a hyperbolic metamaterial and a hollow waveguide with negative index cladding operating at optical frequencies. These structures have the potential to fabricate using combined state-of-the-art STED-DLW technologies and subsequent electroplating of gold. For the hyperbolic metamaterial, the structure supports three different magnetic dipoles,

which cannot only contribute to hyperbolic dispersion but also provide an opportunity to design 3D isotropic effective permeability. For the waveguide, by studying negative index waveguide analytically and numerically under three different loss cases, we discover that material absorption plays an important role in the waveguide performance. These losses will reduce the opportunity for trapping light inside the waveguide. The way to compensate losses will be studied in the next chapter. Finally, we show that direct laser metal writing has the potential to fabricate disconnected metal features.

Chapter 3

Compensation of losses without gain media ¹

3.1 Introduction

Abbe's diffraction limit generally restricts the resolution of conventional optical systems [187]. Sub-wavelength features, which correspond to rapid spatial variance of electromagnetic waves, are decayed exponentially and are consequently too weak to contribute to the image in the far field. The smallest feature size that conventional optical systems can resolve is about one half of the light wavelength. Perfect lenses

¹The material contained in this chapter was previously published in Prog. Electromagn. Res. C 70, 1 (2016) and J. Opt. Soc. Am. B 34, 1310 (2017). Refer Appendix A for granted permission to be published.

[7, 9, 34], superlenses [188, 189, 190], flat lenses [191, 192], and hyperlenses, including magnifying superlenses [2, 10, 11, 126, 127, 128, 129, 193, 194] based on metamaterials have been proposed or experimentally demonstrated. These lenses provide the possibility to break the diffraction limit. The ability for converting evanescent waves to propagating waves and hence allowing for image processing with conventional optical components has made hyperlenses receive much attention along with alternative approaches, such as super-resolution imaging with microsphere lenses [195, 196]. So far, the proposed and fabricated hyperlenses mainly consist of pairs of metal and dielectric layers. These structures are highly anisotropic metamaterials with generally opposite signs of permittivity tensor elements to give hyperbolic dispersion.

Unfortunately, different types of loss mechanisms exist that constrain the hyperlens resolution. These loss mechanisms include absorptive loss, such as in metal components [140], discretization loss (i.e., periodicity artifacts [147]) arising from the invalidity of the homogeneous effective medium approximation, and impedance mismatch loss that appears at the interface between the hyperlens and the substrate [197].

Recently, we proposed a novel loss compensation technique called the plasmon injection scheme (or referred to as Π scheme) [107]. The Π scheme is realized by a coherent superposition of two electromagnetic fields in a lossy medium, such as a metamaterial. One of the fields constitutes the signal and is excited in the metamaterial by an

external input field, such as an object field to be imaged. The other field is the pump and is excited in the metamaterial by an external auxiliary field. The pump field is used to compensate the photon loss in the signal. Although the original Π scheme was based on surface plasmon polariton (SPP) modes in plasmonic metamaterials, hence the name, the concept is equally applicable to any type of electromagnetic mode. This technique does not need traditional optical-gain providing medium, hence eliminates its associated complexities, and is more importantly equivalent to applying a simple spatial filter for imaging.

In this chapter, we used the design of one experimentally realized cylindrical hyperlens as an example to demonstrate the applicability of this technique to hyperlensing for higher resolution imaging. We showed the mathematical details of the entire procedure of the Π scheme loss compensation technique as an equivalent inverse filter post-processing scheme and implement it for a hyperlens imaging system to demonstrate that this technique can compensate losses originating from different types of physical mechanisms, not only absorption but also discretization and impedance mismatch.

3.2 Procedure for the inverse filter loss compensation technique emulating the Π scheme

The hyperlens that we studied here is from [2]. To begin the procedure, the simulation result from [2] is replicated using the commercial finite element solver COMSOL Multiphysics. Fig. 3.1 shows the simulated magnetic field distribution. The hyperlens consists of 8 pairs of concentric Ag/Al₂O₃ layers, with the surrounding material being quartz. The thickness of the Ag and Al₂O₃ layers is 35nm. At $\lambda_0 = 365\text{nm}$ working wavelength, the permittivities of Ag, Al₂O₃ and quartz are $\epsilon_m = -2.4012 + i0.2488$, $\epsilon_d = 3.217$, and $\epsilon_{qtz} = 2.174$, respectively. This layered structure can be considered as a homogeneous anisotropic structure with the effective permittivity satisfying the following equations:

$$\epsilon_\rho = \frac{\epsilon_m \epsilon_d}{(1-p)\epsilon_m + p\epsilon_d} \quad (3.1)$$

$$\epsilon_\phi = p\epsilon_m + (1-p)\epsilon_d \quad (3.2)$$

where p is the filling ratio of the metal. In this designed structure, $p = 0.5$, and then

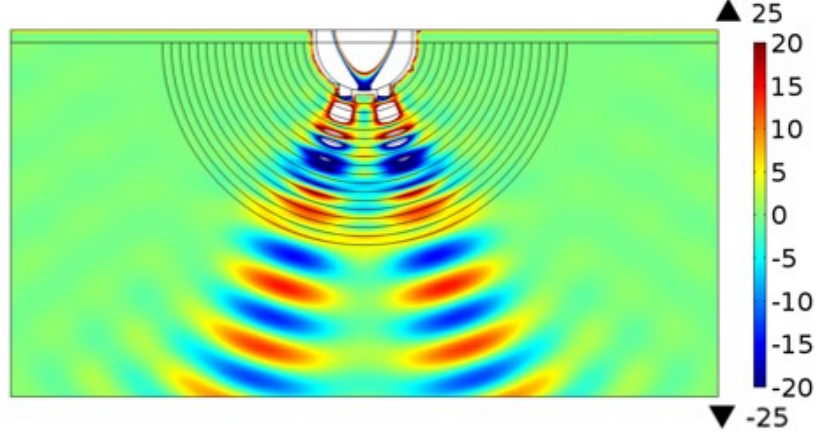


Figure 3.1: Replicated hyperlens magnetic field (A/m) distribution simulation result corresponding to Fig. 2(b) from [2]. Two 50nm wide openings in a 50nm thick Cr layer are considered as the object. The center to center separation of the openings is 150nm. The working wavelength is 365nm. Image taken from ref [3], [EMW Publishing].

$\epsilon_\rho = -16.7786 + i7.0793$ and $\epsilon_\phi = 0.4079 + i0.1244$. The hyperlens is illuminated by a transverse-magnetic(TM) polarized plane wave (i.e., magnetic field is along the axis of the cylindrical hyperlens) using a port backed by perfectly matched layers (PML) to absorb outgoing waves. The result is in agreement with Fig. 2(b) from [2].

After verifying the simulation result, the imaging process can begin as described here. First, the raw image is obtained by the hyperlens. Due to absorptive loss in the hyperlens, the high spatial frequency components of the object are attenuated on the image plane. Then, a filter is applied to compensate this attenuation. After this post processing, a high resolution image will be obtained. The compensation filter applied here is the inverse of the hyperlens transfer function, which is calculated by simulation. Interestingly, this corresponds to recently proposed Π scheme loss compensation technique for imaging [107]. In the Π scheme, the total incident field

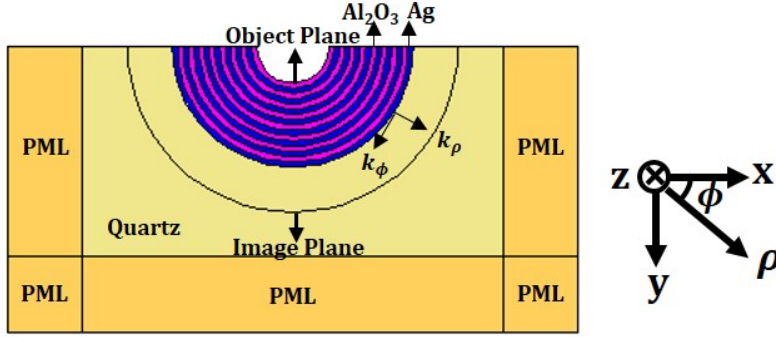


Figure 3.2: Geometry for the studied hyperlens designed in COMSOL. Cylindrical coordinate system (ρ, ϕ, z) is used in the simulation. [Reprinted/Adapted] with permission from ref [4], [Optical Society of America].

in the object plane is a coherent superposition of the main object to be imaged and some auxiliary object. The auxiliary object coherently excites the underlying modes of the system, resulting in a compensation of the attenuation in the main object. This scheme is equivalent to applying a filter in the Fourier domain to amplify the high spatial frequency components. Although inverse filtering is well-known for propagating modes in the field of image processing, application to evanescent modes and intimate relation with loss compensation distinguish the work presented here from traditional inverse filtering. In the following parts, we will show the steps of the loss compensation technique in detail.

3.2.1 Mode solution in hyperlens

Figure 3.2 shows the geometry of the studied hyperlens. Here we assume TM polarization (i.e., field components E_ρ , E_ϕ , and H_z) and the permittivity tensor

$\vec{\epsilon}_r = \begin{bmatrix} \epsilon_\rho & 0 & 0 \\ 0 & \epsilon_\phi & 0 \\ 0 & 0 & \epsilon_z \end{bmatrix}$. In cylindrical coordinates, the time-harmonic form of Maxwell equations $\vec{\nabla} \times \vec{H} = -j\omega \vec{D}$ and $\vec{\nabla} \times \vec{E} = j\omega \vec{B}$ can be written as:

$$\vec{\nabla} \times \vec{H} = \frac{1}{\rho} \begin{vmatrix} \hat{\rho} & \rho \hat{\phi} & \hat{z} \\ \frac{\partial}{\partial \rho} & \frac{\partial}{\partial \phi} & 0 \\ 0 & 0 & H_z \end{vmatrix} = \frac{1}{\rho} \left[\frac{\partial H_z}{\partial \phi} \hat{\rho} - \frac{\partial H_z}{\partial \rho} \hat{\phi} \right] \quad (3.3)$$

$$\vec{\nabla} \times \vec{E} = \frac{1}{\rho} \begin{vmatrix} \hat{\rho} & \rho \hat{\phi} & \hat{z} \\ \frac{\partial}{\partial \rho} & \frac{\partial}{\partial \phi} & 0 \\ E_\rho & \rho E_\phi & 0 \end{vmatrix} = \frac{1}{\rho} \left[\frac{\partial(\rho E_\phi)}{\partial \rho} - \frac{\partial E_\rho}{\partial \phi} \right] \hat{z} \quad (3.4)$$

$$j\omega \vec{D} = j\omega \epsilon_0 \vec{\epsilon}_r \vec{E} = j\omega \epsilon_0 \begin{bmatrix} \epsilon_\rho & 0 & 0 \\ 0 & \epsilon_\phi & 0 \\ 0 & 0 & \epsilon_z \end{bmatrix} \begin{bmatrix} E_\rho \\ E_\phi \\ 0 \end{bmatrix} = j\omega \epsilon_0 (\epsilon_\rho E_\rho \hat{\rho} + \epsilon_\phi E_\phi \hat{\phi}) \quad (3.5)$$

$$j\omega \vec{B} = j\omega \mu_0 \mu_r \vec{H} = j\omega \mu_0 H_z \hat{z} \quad (3.6)$$

Thus, we obtain three coupled equations corresponding to ρ , ϕ and z components,

respectively:

$$\begin{cases} j\omega\epsilon_0\epsilon_r h_o E_\rho = -\frac{1}{\rho} \frac{\partial H_z}{\partial \phi} \\ j\omega\epsilon_0\epsilon_p h_i E_\phi = \frac{\partial H_z}{\partial \rho} \\ \frac{1}{\rho} \left[\frac{\partial(\rho E_\phi)}{\partial \rho} - \frac{\partial E_\rho}{\partial \phi} \right] = j\omega\mu_0 H_z \end{cases} \quad (3.7)$$

Eliminating E_ρ and E_ϕ in Eq. 3.7 and using the free-space relations $c = 1/\sqrt{\epsilon_0\mu_0}$, $k_0 = 2\pi/\lambda_0 = 2\pi/(c/f) = \omega/c$, we obtain the following Eq. 3.8, which only contains the H_z component:

$$\frac{\rho}{\epsilon_\phi} \frac{\partial}{\partial \rho} \left(\rho \frac{\partial H_z}{\partial \rho} \right) + \frac{1}{\epsilon_\rho} \frac{\partial^2 H_z}{\partial \phi^2} = -k_0^2 \rho^2 H_z \quad (3.8)$$

Using the separation-of-variables method [198], the solution can be written in the form of

$$H_z = R(\rho)\Phi(\phi) \quad (3.9)$$

Substituting Eq. 3.9 into Eq. 3.8, we obtain

$$\frac{1}{\epsilon_\phi} \frac{\rho}{R(\rho)} \frac{d}{d\rho} \left(\rho \frac{dR(\rho)}{d\rho} \right) + \frac{1}{\epsilon_\rho} \frac{1}{\Phi(\phi)} \frac{d^2\Phi(\phi)}{d\phi^2} = -k_0^2 \rho^2 \quad (3.10)$$

Since the second term in Eq. 3.10 is a function of only ϕ component, it can be set equal to a constant:

$$\frac{1}{\Phi(\phi)} \frac{d^2\Phi(\phi)}{d\phi^2} = -m^2 \quad (3.11)$$

The valid solution for $\Phi(\phi)$ is

$$\Phi(\phi) \propto e^{im\phi} \quad (3.12)$$

Substituting Eq. 3.11 into Eq. 3.10, for the ρ component, $R(\rho)$ satisfies

$$\rho^2 \frac{d^2 R(\rho)}{d\rho^2} + \rho \frac{dR(\rho)}{d\rho} + \left(\rho^2 k_0^2 \epsilon_\phi - \frac{\epsilon_\phi}{\epsilon_\rho} m^2 \right) R(\rho) = 0 \quad (3.13)$$

Equation 3.13 is a generalized Bessel equation, and the solution has the form

$$R(\rho) \propto J_{m\sqrt{\frac{\epsilon_\phi}{\epsilon_\rho}}} (k_0 \sqrt{\epsilon_\phi} \rho) \quad (3.14)$$

Therefore, the final solution can be written as a product of $R(\rho)$ and $\Phi(\phi)$:

$$H_z(\rho, \phi) \propto J_{m\sqrt{\frac{\epsilon_\phi}{\epsilon_\rho}}}(k_0\sqrt{\epsilon_\phi}\rho)e^{im\phi} \quad (3.15)$$

Here m is the angular momentum mode number of the cylindrical wave. Due to the angular momentum conservation, the tangential component of the wave vector k_ϕ satisfies the equation $m = k_\phi\rho$, where ρ is the distance from center.

Since the real parts of ϵ_ϕ and ϵ_ρ have opposite signs and are considerably larger in magnitude than the imaginary parts, the hyperlens has hyperbolic dispersion relation, which has approximately the form [1, 10]

$$\frac{k_\rho^2}{\epsilon_\phi} - \frac{k_\phi^2}{|\epsilon_\rho|} = \left(\frac{\omega}{c}\right)^2 \quad (3.16)$$

With the wave propagating away from the center, k_ϕ is decreased as a result of increasing ρ . Meanwhile, the image is magnified by approximately a factor of (r_2/r_1) , where r_1 and r_2 are the radii of the object and image planes, respectively.

3.2.2 Selection of the object and image plane

Due to the cylindrical coordinate system, the object and image surfaces are curved,

as shown in Fig. 3.2. We prefer to call these surfaces in the rest of the chapter as the object plane and image plane, respectively, since the object and image are still confined to quasi-planar edges of the hyperlens in most experiments [11, 127, 128, 129, 193]. The object plane is selected as the inner surface of the hyperlens. The radius of the object plane is $r_1 = 240\text{nm}$. Imaging with the hyperlens differs from the negative index flat lens [108], in that the distance between the image plane and the object plane for the flat lens is equal to twice the lens thickness, resulting in an automatic phase compensation at the image plane [9]. However, in the hyperlens, for different values of spatial frequency k_ϕ , the phase is restored at different positions. Since there is no unique image plane to realize the phase compensation, we can arbitrarily choose the image plane location. This means that the compensation scheme should then account for both the amplitude and phase. The radius of the image plane we choose here is $r_2 = 1100\text{nm}$. As a result, the image has around 4.5 times magnification.

3.2.3 Cylindrical wave expansion of an arbitrary electromagnetic field

A. Expansion at the object plane

An object here can be represented by a TM-polarized arbitrary magnetic field $O_z(\rho, \phi)$, which can be expanded in a basis of cylindrical waves obtained in Section 3.2.1:

$$O_z(\rho, \phi) = \int_0^{+\infty} \sum_{m=0}^{+\infty} A(k_\rho, m) \cdot J_{m\sqrt{\frac{\epsilon_\phi}{\epsilon_\rho}}}(k_0\sqrt{\epsilon_\phi}\rho) e^{im\phi} k_\rho dk_\rho \quad (3.17)$$

where

$$A(k_\rho, m) = \tilde{F}(O_z(\rho, \phi)) = \int_0^{+\infty} \int_0^{2\pi} O_z(\rho, \phi) [J_{m\sqrt{\frac{\epsilon_\phi}{\epsilon_\rho}}}(k_0\sqrt{\epsilon_\phi}\rho)]^* \times e^{-im\phi} \rho d\rho d\phi \quad (3.18)$$

The object is defined at the object plane $\rho = r_1$, and k_ρ is related to m by Eq. 3.16.

Thus, Eq. 3.17 can be written as

$$\begin{aligned} O_z(\rho = r_1, \phi) &= \sum_{m=0}^{+\infty} A(k_\rho(m, \rho = r_1), m) \cdot J_{m\sqrt{\frac{\epsilon_\phi}{\epsilon_\rho}}}(k_0\sqrt{\epsilon_\phi}r_1) e^{im\phi} k_\rho(m, \rho = r_1) \\ &= \sum_{m=0}^{+\infty} A(k_{\rho_1}(m), m) B(m) k_{\rho_1}(m) e^{im\phi} \end{aligned} \quad (3.19)$$

where we define

$$J_{m\sqrt{\frac{\epsilon_\phi}{\epsilon_\rho}}}(k_0\sqrt{\epsilon_\phi}r_1) = B(m) \quad (3.20)$$

Then Eq. 3.18 changes to

$$\begin{aligned}
A(k_{\rho 1}(m), m) &= \tilde{F}(O_z(\rho = r_1, \phi)) = \tilde{O}(m) \\
&= \sum_{n=0}^{+\infty} O_z(\rho = r_1, \phi_n) \cdot [J_{m\sqrt{\frac{\epsilon_\phi}{\epsilon_\rho}}}(k_0\sqrt{\epsilon_\phi}r_1)]^* \times e^{-im\phi_n} r_1 \\
&= B^*(m)r_1 \sum_{n=0}^{+\infty} O_z(\rho = r_1, \phi_n) e^{-im\phi_n}
\end{aligned} \tag{3.21}$$

Then we obtain

$$\tilde{F}(O_z(\rho = r_1, \phi)) = \tilde{F}_p(O_z(\rho = r_1, \phi)) \tilde{F}_\phi(O_z(\rho = r_1, \phi)) \tag{3.22}$$

The ρ part $\tilde{F}_p(O_z(\rho = r_1, \phi)) = B^*(m)r_1$ is constant for different values of m and can be easily calculated. On the other hand, the ϕ part can be calculated in MATLAB:

$$\tilde{O}'(m) = \tilde{F}_\phi(O_z(\rho = r_1, \phi)) = \sum_{n=0}^{+\infty} O_z(\rho = r_1, \phi_n) e^{-im\phi_n} \tag{3.23}$$

and then

$$\tilde{O}(m) = B^*(m)r_1\tilde{O}'(m) \quad (3.24)$$

B. Expansion at the image plane

Similar to the object, the raw image $I_z(\rho, \phi)$ obtained at the image plane $\rho = r_2$ satisfies the following equations:

$$I_z(\rho = r_2, \phi) = \sum_{m=0}^{+\infty} C(k_{\rho 2}(m), m)D(m)k_{\rho 2}(m)e^{im\phi} \quad (3.25)$$

$$J_{m\sqrt{\frac{\epsilon_\phi}{\epsilon_\rho}}}(k_0\sqrt{\epsilon_\phi}r_2) = D(m) \quad (3.26)$$

$$C(k_{\rho 2}(m), m) = \tilde{I}(m) = D^*(m)r_2 \sum_{n=0}^{+\infty} I_z(\rho = r_2, \phi_n)e^{-im\phi_n} \quad (3.27)$$

$$\tilde{I}'(m) = \sum_{n=0}^{+\infty} I_z(\rho = r_2, \phi_n)e^{-im\phi_n} \quad (3.28)$$

$$\tilde{I}(m) = D^*(m)r_2\tilde{I}'(m) \quad (3.29)$$

$\tilde{I}(m)$ and $\tilde{O}(m)$ are related by the transfer function $T(m)$ as

$$\tilde{I}(m) = \tilde{O}(m)T(m) \quad (3.30)$$

C. Increasing the lengths of the object and image planes

The method used in MATLAB to calculate the discrete Fourier transform is the fast Fourier transform. Using the raw image, for example, Eq. 3.28 is changed to

$$\tilde{I}'(m) = \sum_{n=1}^N I_z(\rho = r_2, \phi_n) e^{\frac{i2\pi(m-1)(n-1)}{N}} \quad (3.31)$$

Comparing Eq. 3.31 with Eq. 3.28, it can be seen that ϕ_n satisfies

$$\phi_n = \frac{2\pi(n-1)}{N} \quad (3.32)$$

Equation 3.32 requires that the arc length of the image plane should be $2\pi r_2$. In the simulation, we can only define ϕ from 0 to π due to the actual geometry of the fabricated structure. Therefore, a window function is applied to define the fields in the ranges $\pi < \phi \leq 1.5\pi$ and $-0.5\pi \leq \phi < 0$. Since the object is always defined at the central part of the object plane, the corresponding image is also obtained in the

center. Hence, we choose a simple rectangular window function $u(0 \leq \phi \leq \pi) = 1$, and $u(-0.5\pi \leq \phi < 0) = u(\pi < \phi \leq 1.5\pi) = 0$. As a result, the electromagnetic fields outside the computational domain are set to 0.

3.2.4 Transfer function calculation

In the simulation, we define cylindrical waves as the input with the form $e^{im\phi}$ at the object plane $\rho = r_1$, where different values of m correspond to different spatial frequencies. At the image plane, $\rho = r_2$, the complex field information of the image is obtained. We collect the complex magnetic field $h_o(m)$ at point $P_1(r_1, \phi_0)$ on the object plane and $h_i(m)$ at point $P_2(r_2, \phi_0)$ on the image plane. The angle ϕ_0 is arbitrary and chosen as $\pi/2$ for convenience. Then we obtain complex $T'(m)$ as

$$T'(m) = h_i(m)/h_o(m) \quad (3.33)$$

Here, we should note that $T'(m)$ is not equal to the transfer function $T(m)$ in Eq. 3.30. Even in the absence of losses, the cylindrical wave amplitude changes as the wave propagates. $T'(m)$ is calculated by the division of the fields at the two points. Thus, $T'(m)$ accounts for only the amplitude change between the object plane and image plane for individual cylindrical waves. In contrast, $T(m)$ in Eq. 3.30 results from all the points and waves contributing to the object and image. For example, in the

lossless case, $T(m) = 1$. Therefore, $T(m)$ and $T'(m)$ can be related by

$$T(m) = \frac{T'(m)}{t(m)} \quad (3.34)$$

where $t(m)$ corrects the amplitude change between the image plane and the object plane. For a particular m , every radial frequency k_ρ along the curve contributes to the cylindrical wave amplitude. Thus, $t(m)$ satisfies

$$t(m) = \frac{\int_0^{+\infty} J_{m\sqrt{\frac{\epsilon_\phi}{\epsilon_\rho}}}(k_0\sqrt{\epsilon_\phi\rho})e^{im\phi}k_\rho dk_\rho \Big|_{\rho=r_2}}{\int_0^{+\infty} J_{m\sqrt{\frac{\epsilon_\phi}{\epsilon_\rho}}}(k_0\sqrt{\epsilon_\phi\rho})e^{im\phi}k_\rho dk_\rho \Big|_{\rho=r_1}} = \frac{D(m)k_{\rho 2}(m)}{B(m)k_{\rho 1}(m)} \quad (3.35)$$

which will be used in the following part calculation.

3.2.5 Loss compensation procedure

Due to losses during the imaging process, the high-spatial frequency components of the object that correspond to large m value are decayed rapidly such that they become too weak to contribute to the image resolution. Therefore, the compensation filter $F(m) = 1/T(m)$ is used to amplify those frequency components, and the Fourier spectrum of the compensated image $\tilde{I}_c(m)$ satisfies

$$\tilde{I}_c(m) = \tilde{I}(m)F(m) = \frac{\tilde{O}(m)T(m)}{T(m)} = \tilde{O}(m) \quad (3.36)$$

3.2.6 Simplification of the post-processing procedure for the loss compensation

Since ρ is fixed at the object and image planes, the Fourier spectrum of the ρ components is always constant with a fixed m value. Thus, it can be shown that in order to simplify the post-processing for the loss compensation, we do not need to consider the ρ components in the calculation. To achieve our goal, first, we will derive two equations below. In Section 3.2.4, we define the object to be $e^{im\phi}$, which can be expanded using Eqs. 3.19 and 3.21:

$$e^{im\phi} = \sum_{m'=0}^{+\infty} A(k_{\rho 1}(m'), m')B(m')k_{\rho 1}(m')e^{im'\phi} \quad (3.37)$$

$$A(k_{\rho 1}(m'), m') = B^*(m')r_1 \sum_{n=0}^{+\infty} e^{im\phi_n} e^{-im'\phi_n} = B^*(m')r_1 \delta(m - m') \quad (3.38)$$

Substituting $A(k_{\rho 1}(m'), m')$ into Eq. 3.37, we obtain

$$e^{im\phi} = r_1 k_{\rho 1}(m) |B(m)|^2 e^{im\phi} \quad (3.39)$$

Hence, this gives the first equation:

$$r_1 k_{\rho 1}(m) |B(m)|^2 = 1 \quad (3.40)$$

Similar to the object plane, at the image plane $\rho = r_2$, we can derive another equation:

$$r_2 k_{\rho 2}(m) |D(m)|^2 = 1 \quad (3.41)$$

Then we define a new compensation filter $F'(m) = 1/T'(m)$, which is different from $F(m) = 1/T(m)$. Applying $F'(m)$ directly to $\tilde{I}'(m)$ we obtain $\tilde{I}'_c(m)$, which is the ϕ component of the Fourier spectrum for the compensated image:

$$\tilde{I}'_c(m) = \tilde{I}'(m) F'(m) = \frac{\tilde{I}'(m)}{T'(m)} \quad (3.42)$$

Using Eqs. 3.24, 3.29, 3.30, 3.34, 3.35, 3.40 and 3.41, we obtain

$$\begin{aligned}
\tilde{I}'_c(m) &= \frac{\tilde{I}'(m)}{T(m)t_m} = \frac{\tilde{I}'(m)}{\left(\frac{\tilde{I}(m)}{\tilde{O}(m)}\right)\left(\frac{D(m)k_{\rho 2}(m)}{B(m)k_{\rho 1}(m)}\right)} \\
&= \frac{\tilde{I}(m)}{D^*(m)r_2} \frac{\tilde{O}(m)}{\tilde{I}(m)} \frac{B(m)k_{\rho 1}(m)}{D(m)k_{\rho 2}(m)} \\
&= \frac{\tilde{O}(m)}{B^*(m)r_1} \frac{1}{r_2 k_{\rho 2}(m) |D(m)|^2} \\
&= \tilde{O}'(m)
\end{aligned} \tag{3.43}$$

Thus, the ϕ component of the Fourier spectrum is fully compensated. At the image plane $\rho = r_2$, based on Eq. 3.29, the ρ component of the Fourier spectrum is equal to $D^*(m)r_2$. Then, $\tilde{I}_c(m)$ is given by

$$\tilde{I}_c(m) = D^*(m)r_2\tilde{I}'_c(m) \tag{3.44}$$

Taking the inverse Fourier transform,

$$\begin{aligned}
I_c(\rho = r_2, \phi) &= \tilde{F}^{-1}(\tilde{I}_c(m)) = \sum_{m=0}^{+\infty} \tilde{I}_c(m) D(m) k_{\rho 2}(m) e^{im\phi} \\
&= \sum_{m=0}^{+\infty} D^*(m) r_2 \tilde{I}'_c(m) D(m) k_{\rho 2}(m) e^{im\phi} \\
&= \sum_{m=0}^{+\infty} \tilde{I}'_c(m) e^{im\phi} \tag{3.45}
\end{aligned}$$

Equation 3.45 shows that the inverse Fourier transform of the ϕ component of the compensated image spectrum $\tilde{I}'_c(m)$ is equal to the inverse Fourier transform of the total compensated image spectrum $\tilde{I}_c(m)$. Therefore, it is sufficient to take the inverse Fourier transform of only the ϕ component. Then, the resultant compensated image is a function of ϕ with $\rho = r_2$. This simplifies the loss compensation by reducing the post-processing to the calculation of only the ϕ component.

3.2.7 Selection of the cutoff frequency for the transfer function

According to Eqs. 3.36 and 3.43, in the ideal case, the compensated image will recover all the information of the object. However, we acquire the transfer function and the image from finite element simulations. Noise corresponding to numerical error will be produced during the simulation because of the imperfect mesh size and solver settings in COMSOL. Due to the losses in the imaging process, the amplitude of high-spatial-frequency components becomes comparable or less than the noise at the image plane.

This marks the cutoff frequency. Here we define a variable γ as

$$\gamma = \max(A_i)/\min(A_i) \tag{3.46}$$

where A_i is the amplitude of the cylindrical wave at the image plane for the i th spatial frequency. The condition for the cutoff frequency is determined by $\gamma = 3\text{dB}$ below unless otherwise stated. This means that we consider only the spatial frequency components less than the cutoff frequency, for which $\min(A_i) \geq 0.5\max(A_i)$. We refer to the resultant object, which excludes high spatial frequencies above cutoff, as the truncated object. In signal processing, 3dB attenuation commonly defines the cutoff frequency for filters.

3.3 Application of the Π scheme to different loss mechanisms in the imaging system

3.3.1 Results for applying the loss compensation technique to the experiment hyperlens

Based on procedure in Section 3.2, the transfer function and corresponding compensation filter for amplitude and phase are shown in Fig. 3.3. Since m is an integer, the

transfer function is a discrete function of m .

To demonstrate the imaging procedure, a magnetic field with four Gaussian features is defined at the object plane as an example. Note that this procedure can be performed with any arbitrary features at the object plane. The field is defined so that the smallest separation between two peaks is 50nm. To begin, the raw image is obtained through the hyperlens at the image plane. Then in the spatial frequency domain, the Fourier transform of the raw image is multiplied by the compensation filter. The amplitude and phase compensation results are shown in Figs. 3.4(a) and (b), respectively. After transformation back to the spatial domain, the compensated image is obtained in Fig. 3.4(c). The image is magnified because of the hyperlens dispersion and geometry. Therefore, in order to clearly show the result, θ is used as the horizontal axis in Fig. 3.4(c). It is clearly seen that the sub-diffraction-limited features of the object can be reconstructed with a resolution of $\lambda_0/7$ after applying the loss compensation filter, while the raw image obtained by the hyperlens alone cannot be resolved.

We should note that according to section 3.2.7, the filter was truncated at $m = 36$. The resultant truncated object, which maintains the major sub-diffraction-limited features of the original object, is also shown in 3.4(c). The loss compensation filter almost perfectly reconstructs the truncated object.

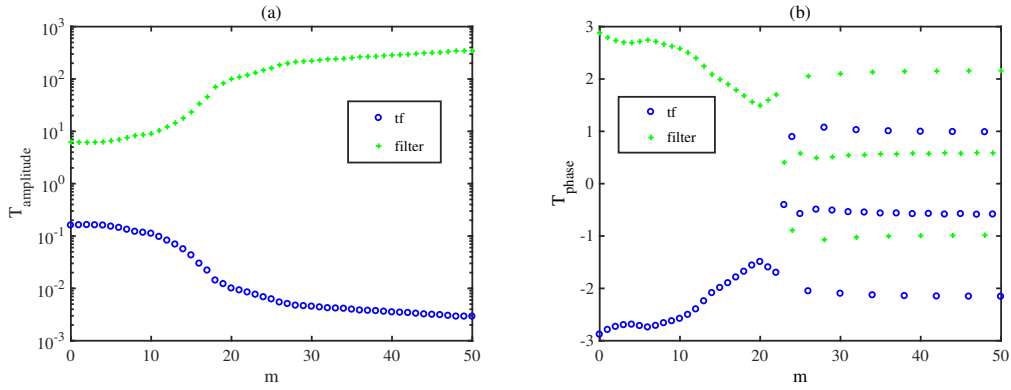


Figure 3.3: Calculated (a) amplitude and (b) phase of the hyperlens transfer function (blue) plotted with the corresponding compensation filter (green). Image taken from ref [3], [EMW Publishing].

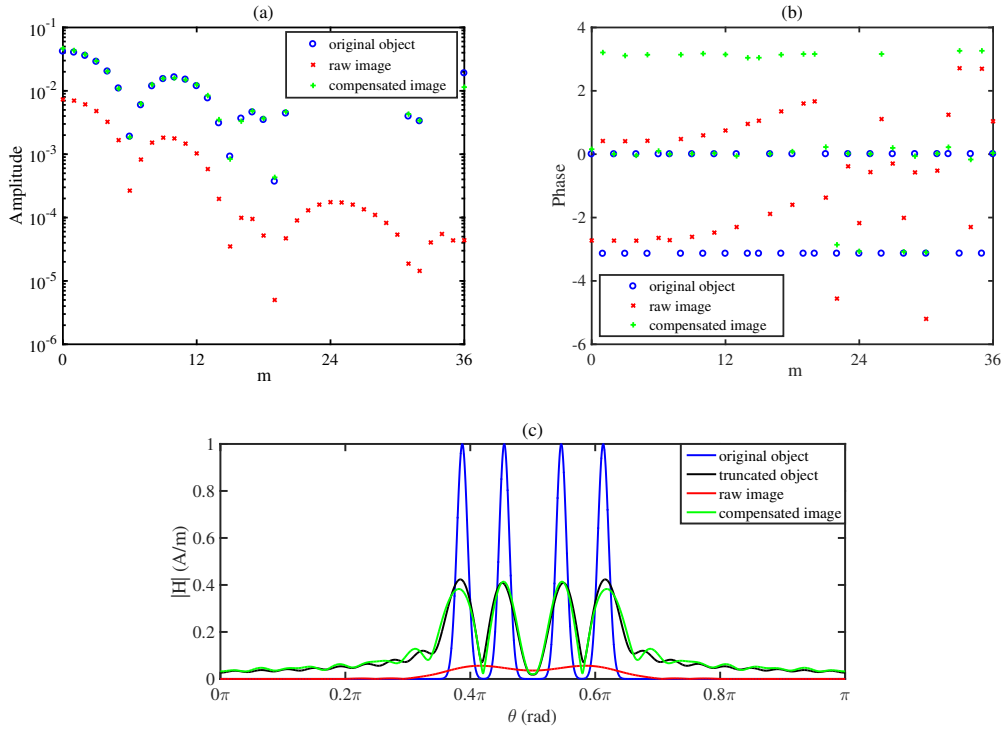


Figure 3.4: (a) Amplitude and (b) phase Fourier spectra for the original object, raw image, and compensated image, respectively. (c) Magnetic field intensity for the original object, truncated object, raw image, and compensated image. The compensated image is clearly resolved beyond the diffraction limit. Image taken from ref [3], [EMW Publishing].

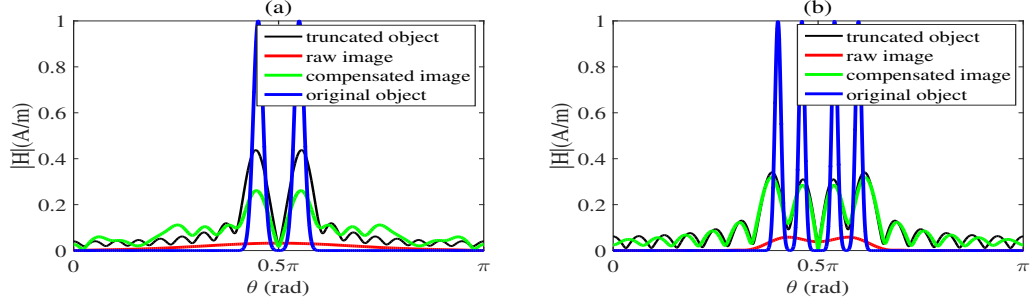


Figure 3.5: Magnetic field intensity for the original object, truncated object, raw image, and compensated image for (a) 328nm wavelength, and (b) 372nm wavelength

In general, the present compensation method can be applied to any part of the electromagnetic spectrum. Here, using the permittivity data in [199] and [200] for Ag and Al_2O_3 , respectively, we found that the structure in Fig. 3.2 maintains hyperbolic dispersion over a wavelength range from 328nm (915THz) to 372nm (806THz). When the compensation method is applied to this entire wavelength range, according to our simulations the obtained resolutions are $\lambda_0/4.4$ at 328nm and $\lambda_0/8.5$ at 372nm with the resolution enhancement factors of 4.4 and 1.6, respectively. The results are shown in Figure 3.5. It is important to note that at 328nm in particular, the resolution of the hyperlens without the loss compensation method is only λ_0 (i.e., twice worse than the diffraction limit). This shows that the effective operating bandwidth of the hyperlens is also increased by the present compensation method. On the other hand, the effective spatial frequency range, which ultimately determines the image resolution achievable by this compensation method at a given wavelength, is limited by the noise floor.

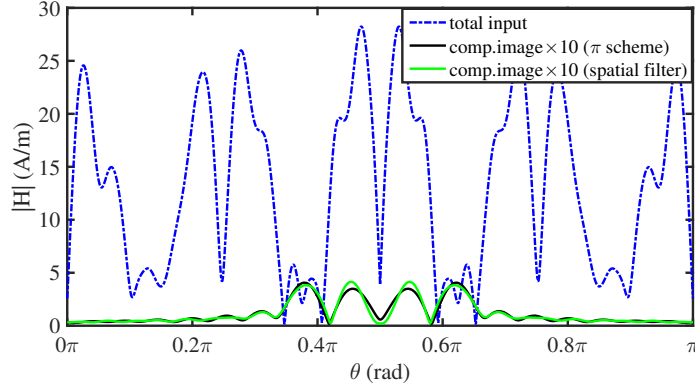


Figure 3.6: Comparison of the images obtained by spatial filtering (green light solid line) and the Π scheme (black solid line) using a coherent superposition of an auxiliary object and the original object as the total input (blue, dash-dotted line) for the hyperlens. Image taken from ref [3], [EMW Publishing].

To illustrate the equivalent of the above spatial filtering process with the Π scheme [107], we simulate directly the coherent superposition of an auxiliary object and the original object as an input to the hyperlens and find the resultant image instead of simulating the original object alone and then performing the spatial filtering (see Fig. 3.6). The superposed total input is calculated from the compensated image spectrum in Fig. 3.4 using the transfer function in Fig. 3.3. The auxiliary object (not shown) is the difference between the total input and the original object due to the linearity of the system. It is clearly seen in Fig. 3.6 that the image obtained through the direct simulation of the total input strongly agrees with the image obtained through the spatial filtering. This suggests that the Π scheme in which a part of the total input (i.e., auxiliary object) physically compensates the losses in the hyperlens to leave the original object intact is equivalent to applying mathematically a compensating spatial filter to the raw image.

3.3.2 Study of different loss mechanisms

The major loss mechanisms responsible for deterioration of the hyperlens image resolution include absorption, inherently discretized unit cells, and impedance mismatch. In our previous work, it has been already shown that the Π scheme is capable of compensating the absorption loss in a homogeneous impedance matched negative index flat lens [108]. In contrast, the hyperlens studied in this chapter was absorbing, consisting of discretized unit cells and impedance mismatched. Using the Π scheme, we enhanced the resolution of such hyperlens from $\lambda_0/4.5$ to $\lambda_0/7$ (i.e., a factor of about 1.6 enhancement in the resolution). However, we did not distinguish what types of losses were compensated in the process. In the following part, we will explicitly show that all of the above losses are accounted by the Π scheme.

A. Absorption loss

To achieve our goal, we start from an absorbing, inhomogeneous, and impedance mismatched experimental hyperlens studied in detail in Section 3.3.1 and redescrbed in Fig. 3.2. It is trivial to prove the compensation of the absorption loss with the Π scheme. When we remove the absorption loss from the hyperlens by defining the silver with $\epsilon_m = -2.4012$ in the simulation, this immediately improves the resolution of the uncompensated hyperlens from $\lambda_0/4.5$ to $\lambda_0/5.4$, indicating that the part of the compensation achieved initially in Section 3.3.1 was indeed for the absorption loss, which is not surprising as the original hyperlens was absorptive due to the nonzero

imaginary part existing in the metal permittivity.

B. Discretization loss

Since the hyperlens is a layered structure, the discretization can also lead to losses. We can consider a layered structure as an effective homogeneous medium under the assumption that the layer thickness is much smaller than one effective wavelength λ_ρ along the radial direction. Based on Eq. 3.16, when the spatial frequency k_ϕ is small (i.e., small m value), such that k_ρ is close to k_0 , the regime where $\lambda_\rho \sim \lambda_0$ is reached. However, in the case that the image contains small sub-wavelength features, which correspond to large k_ϕ , k_ρ is much larger than k_0 . As a result, $\lambda_\rho \ll \lambda_0$ and this leads to λ_ρ being comparable with the layer thickness. Thus, the effective medium assumption is no longer valid. The loss of information due to this process is identified as the discretization loss. Having eliminated the absorption loss by setting the imaginary part of the metal permittivity to zero and applying the compensation procedure in Section 3.2, the results are shown in Fig. 3.7. Figures 3.7 (a) and (b) show, respectively, the amplitude and phase information of the Fourier spectra of the original object [see Eq. 3.23], the raw image [see Eq. 3.31], and the compensated image [see Eq. 3.42]. After the transformation into the spatial domain, the compensated image, which corresponds to the green line, is obtained in Fig. 3.7(c) [see Eq. 3.45]. It is clearly seen that the compensated image coincides with the truncated object (i.e., the object that excludes the high spatial frequencies beyond cutoff) and reasonably well

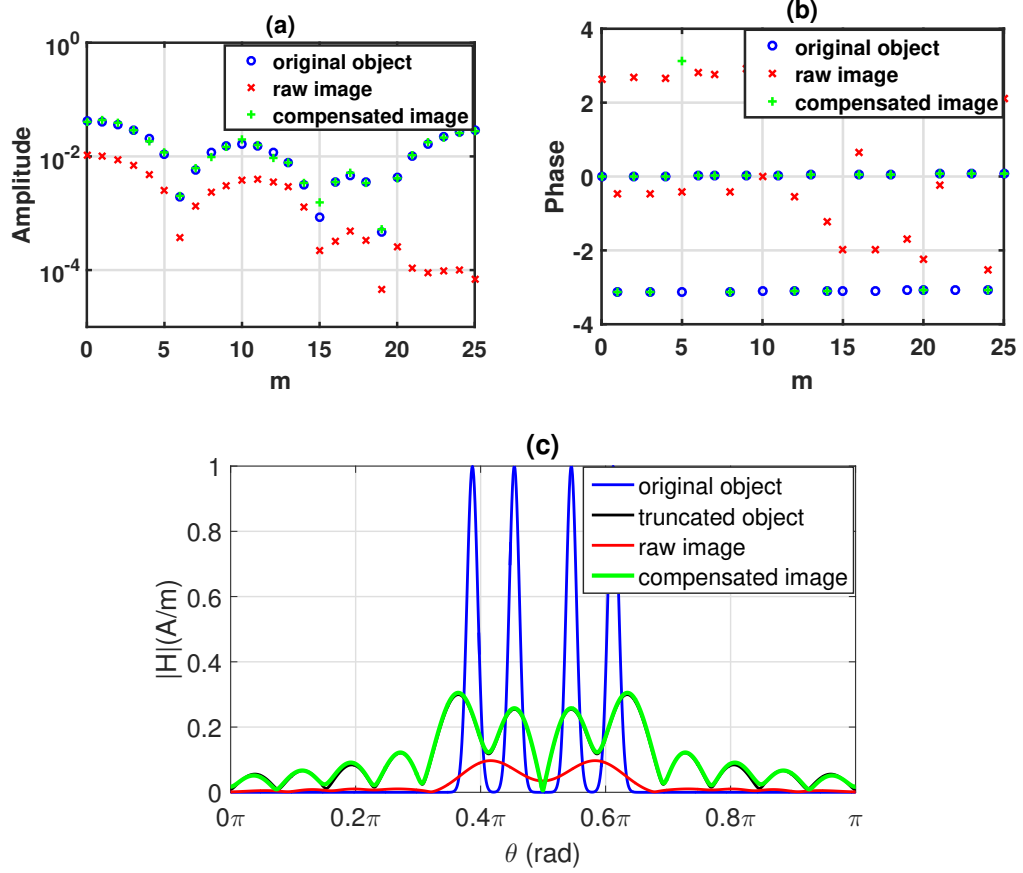


Figure 3.7: (a) Amplitude (A/m) and (b) phase Fourier spectra for the original object, raw image, and compensated image. (c) Magnetic field intensity for the original object, raw image, and compensated image. The Π scheme accounts for the discretization and impedance mismatch losses resulting in a compensated image with a high resolution of $\lambda_0/7$. [Reprinted/Adapted] with permission from ref [4], [Optical Society of America].

represents the original object with small sub-wavelength features separated by $\lambda_0/7$.

This result indicates that the Π scheme compensates losses beyond the absorption loss.

C. Impedance mismatch loss

Even though the enhancement factor due to the loss compensation in Fig. 3.7 and the

direct removal of absorption and discretization above is the same (i.e., $\lambda_0/7$ resolution is obtained in both), this does not mean all the compensation in Fig. 3.7 are from the discretization. As we will show below, the impedance mismatch loss is another major loss mechanism and requires a definition of an object with a higher resolution in our analysis for a proof.

Therefore, to show the effect of loss compensation on the impedance mismatch, we reduced the object feature size to $\lambda_0/9.6$, so that the object cannot be resolved by the nonabsorbing impedance mismatched hyperlens with 10nm layer thickness. Then, following the loss compensation procedure described in detail in Section 3.2, we again applied the compensation filter to the raw image and obtained the loss-compensated high-resolution image, which is otherwise not possible without compensation. It should be noted that the smaller the feature size is, the larger the spatial frequency needed to reconstruct the object. If we still use $\gamma = 3\text{dB}$ to determine the cutoff frequency, which corresponds to $m = 26$, the truncated object cannot well represent the four peaks in the original object, although the compensated image agrees well with the truncated object. Therefore, we increased the cutoff to $m = 30$, which corresponds to $\gamma = 5\text{dB}$. The results are shown in Fig. 3.8. Figures 3.8(a) and (b) are the results in the Fourier domain and Fig. 3.8(c) is the result in the spatial domain. It is clear that the Π scheme continues to compensate some other losses in the system despite negligible discretization loss and no absorption in the system.

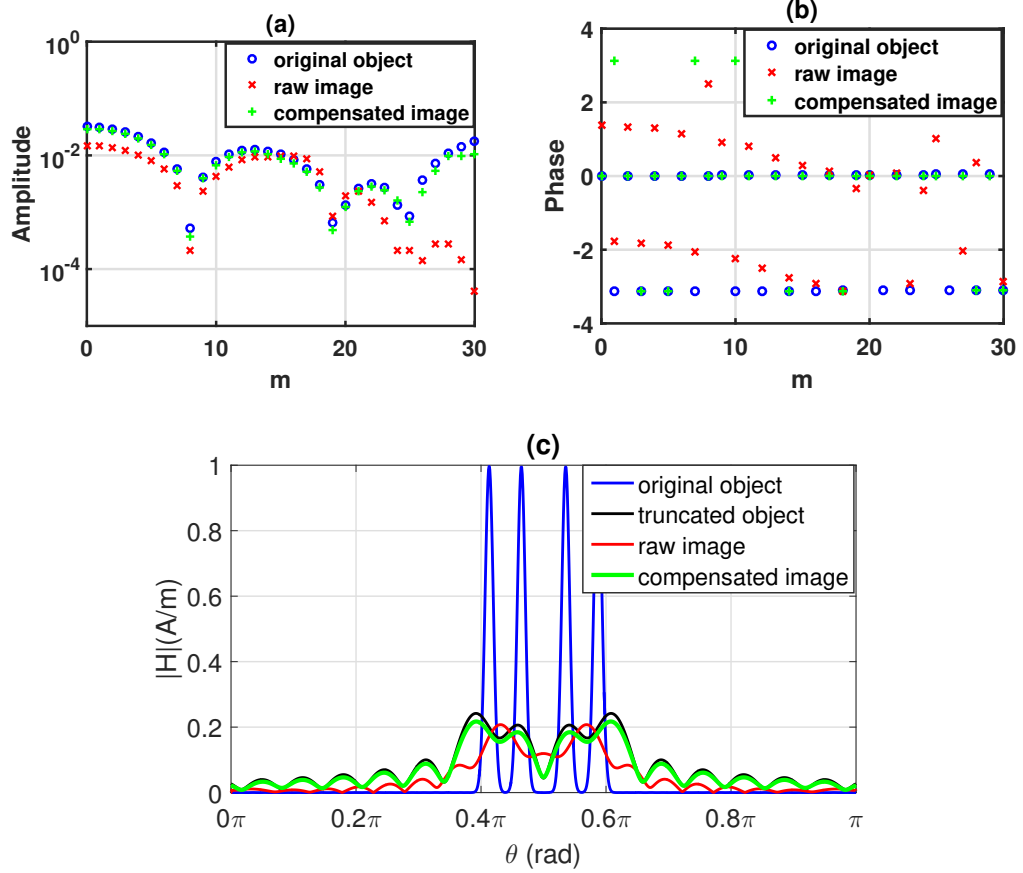


Figure 3.8: (a) Amplitude (A/m) and (b) phase Fourier spectra for the original object, raw image, and compensated image. (c) Magnetic field intensity for the original object, raw image, and compensated image. The Π scheme accounts for impedance mismatch loss resulting in a compensated image with a high resolution of $\lambda_0/9.6$. [Reprinted/Adapted] with permission from ref [4], [Optical Society of America].

When the electromagnetic waves impinge on the outer interface between the hyperlens and the quartz substrate, the impedance inside the hyperlens is not matched with the impedance of the substrate (see Fig. 3.2). Note that since the objects are defined on the inner interface of the hyperlens, there is no impedance mismatch on the inner interface. We will show below that the impedance mismatch is another major loss mechanism, which is largely responsible from the remaining losses and the

one compensated in Fig. 3.8.

The physical implementation of the Π scheme requires applying an auxiliary object coherently superimposed on the original object as the total object to obtain the resultant loss-compensated high-resolution image. Considering this principle, first we calculate the equivalent auxiliary object from the Π scheme directly and then compare it with the auxiliary object calculated from impedance mismatch. If these two auxiliary objects are close to each other, it means the loss compensated in Fig. 3.8 mainly originates from impedance mismatch.

1. Auxiliary object calculation from the Π scheme directly

In the Fourier domain, the compensated image $\tilde{I}_c(m)$ and the total object $\tilde{O}_{total}(m)$ are related by the transfer function $T(m)$ as

$$\tilde{I}_c(m) = \tilde{O}_{total}(m)T(m) \quad (3.47)$$

The auxiliary object $\tilde{O}_{aux}(m)$ satisfies the equation

$$\tilde{O}_{aux}(m) = \tilde{O}_{total}(m) - \tilde{O}(m) \quad (3.48)$$

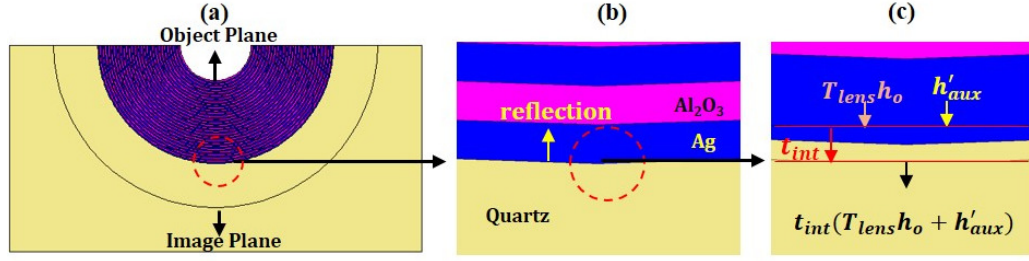


Figure 3.9: (a) Location where the impedance mismatch occurs. (b) The region indicated by the dashed circle in (a) is enlarged. (c) The region indicated by the dashed circle in (b) is enlarged. The two curves, which are $2nm$ away from the interface, are defined as the upper and the lower boundaries to calculate the transmission coefficient $t_{int}(m)$. See the text for the details. [Reprinted/Adapted] with permission from ref [4], [Optical Society of America].

Then, $\tilde{O}_{aux}(m)$ can be calculated by the equation

$$\tilde{O}_{aux}(m) = \frac{\tilde{I}_c(m)}{T(m)} - \tilde{O}(m) \quad (3.49)$$

2. Auxiliary object calculation from the impedance mismatch

The impedance mismatch appears at the interface between the hyperlens and the quartz substrate. As a result, some of the incident waves will reflect at the interface. The auxiliary object $h'_{aux}(m)$ added at the interface will make the transmitted electromagnetic wave equal to the original incident wave. Figure 3.9 shows the schematic for the calculation of the auxiliary object.

$h'_{aux}(m)$ satisfies the equation

$$T_{lens}(m)h_o(m) = t_{int}(m)(T_{lens}(m) \cdot h_o(m) + h'_{aux}(m)) \quad (3.50)$$

where $T_{lens}(m)$ is the transfer function from the object plane to the upper boundary, $h_o(m)$ is the complex field described in Section 3.2.4, and $t_{int}(m)$ is the transmission coefficient at the interface. $T_{lens}(m)$ and $t_{int}(m)$ can be obtained by the similar calculations in Section 3.2.4. After $h'_{aux}(m)$ is obtained, the auxiliary object $h_{aux}(m)$ that needs to be added at the object plane is equal to

$$h_{aux}(m) = h'_{aux}(m)/T_{lens}(m) \quad (3.51)$$

3. Comparison of the two auxiliary objects

$\tilde{O}_{aux}(m)$ and $h_{aux}(m)$ calculated from Eqs. 3.49 and 3.51, respectively, are shown in Fig. 3.10. Fig. 3.10(a) shows the Fourier spectra for the two auxiliary objects. After superimposing the auxiliary object on the original object, the corresponding image is obtained from the total input, as shown in Fig. 3.10(b). The blue curve in Figs. 3.10(a) and (b) is obtained by using the auxiliary object calculated from the Π scheme directly as described in Section 3.3.2.C.1, and the green curve is obtained from the impedance mismatch calculation as described in Section 3.3.2.C.2. The results clearly show that the two auxiliary objects are quite close to each other. Therefore,

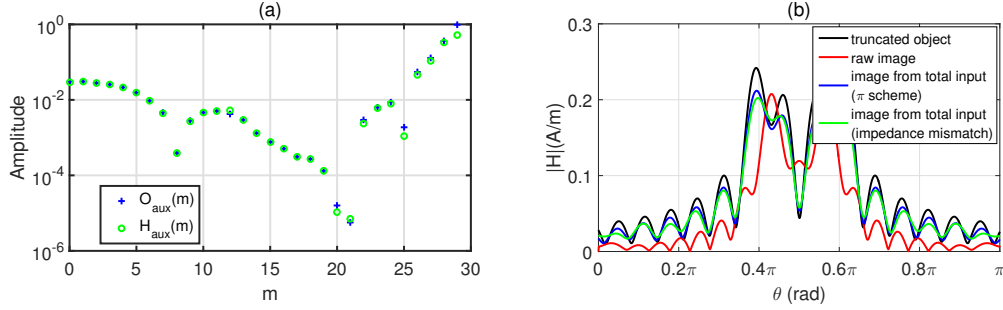


Figure 3.10: (a) Fourier spectra (A/m) for the auxiliary objects calculated by the two different methods. (b) Magnetic field intensity for the truncated object, raw image, and the image from the total input for the two different auxiliary objects. [Reprinted/Adapted] with permission from ref [4], [Optical Society of America].

we can safely conclude that the origin of the losses compensated in Fig. 3.8 is mostly the impedance mismatch. Meanwhile, the results also indicate that the Π scheme is equivalent to mathematically applying a compensating inverse filter, which emulates the physical implementation of the scheme.

3.3.3 Comparison with the magnifying superlens

It is interesting to compare the plasmon injection results for the hyperlens analyzed above in this chapter and the magnifying superlens considered in Refs [193, 194]. The latter consists of alternating layers of effective negative and positive refractive indices resulting from the SPP modes residing at the gold/polymethyl methacrylate and gold/vacuum interfaces, respectively. The plasmonic illumination is achieved by a phase-matching structure. The individual layer thicknesses inside the lens are adjusted such that the phase after propagation through each functional layer is restored to allow for ideal construction of the images. Such a magnifying superlens

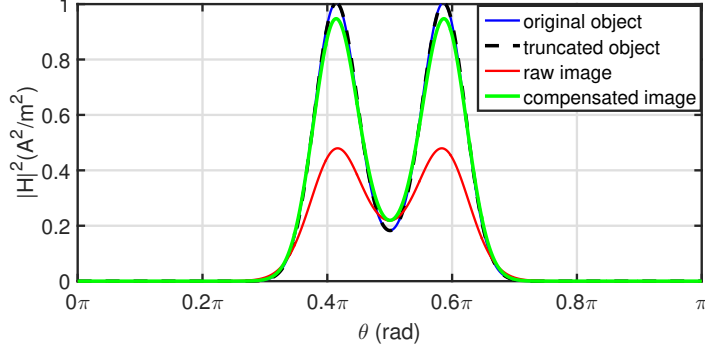


Figure 3.11: Image contrast and resolution of the magnifying superlens are improved with the plasmon injection inverse filter. The FWHM of the Gaussian features in the image is reduced from 77nm (red solid line) to 63nm (green solid line) with the plasmon injection inverse filter. The Gaussian features in the object has a FWHM of 61nm (blue solid line) and is separated by 130nm. The operating wavelength of the magnifying superlens is 532nm. The truncated object (black dashed line) with $m = 25$ perfectly represents the object in the filtering process. [Reprinted/Adapted] with permission from ref [4], [Optical Society of America].

has shown to resolve features of at least $\lambda_0/7$, which is comparable to that of the loss-compensated hyperlens analyzed in detail in this chapter. However, we found that even the resolution of a magnifying superlens can be further improved with the Π scheme. To verify this, we performed simulations for the magnifying superlens and then applied a plasmon injection inverse filter for possible enhancement in the image resolution. An object with Gaussian features that has an intensity full width half-maximum (FWHM) of 61nm was used in the simulations similar to the experiments [193, 194]. The intensity FWHM for the Gaussian features in the resultant image was 77nm, which was very close to the experimental results. With the plasmon injection inverse filter, the image contrast was improved and the FWHM was reduced by approximately 18%, hence resulting in improved resolution (see Fig. 3.11). The enhancement in resolution though was not as remarkable as in the hyperlens imaging

system studied in detail above because the magnifying superlens has not much room for improvement due to lesser losses and already sufficient performance for the given feature size. However, we noticed that the Π scheme becomes more effective for enhancing the resolution of the magnifying superlens if smaller objects are imaged since those objects contain higher spatial frequencies that cannot be easily restored by the superlens alone anymore.

3.4 Conclusion

To sum up, the way to extend this Π scheme to hyperlens is presented, and Π scheme implementation by an inverse filter is demonstrated. The entire process of the inverse filter technique is described analytically in detail and implemented numerically using MATLAB and the finite-element-based COMSOL Multiphysics software package. It has been shown that the angular Fourier spectrum for the images obtained by the hyperlens is adequate for the mathematical implementation of the Π scheme. A strategy for determining the cutoff frequency of the transfer function is discussed. Three major loss mechanisms responsible from the deterioration of the image resolution, including absorption loss, discretization loss, and impedance mismatch loss, are identified and studied separately. The results demonstrate that all of these loss mechanisms existing in the imaging process can be compensated by the Π scheme and its inverse filter analog. Finally, it should be noted that the possibility of compensating the discretization

loss raises the hopes for overcoming the unit cell size limitation, which determines the ultimate quality of the metamaterials (e.g., resolution of a metamaterial lens). This could relax the fabrication constraints by allowing for larger unit cell structures at a fixed operating wavelength.

Chapter 4

Miniaturized RF and optical components¹

4.1 Introduction

To achieve a compact design, we propose an extremely sub-wavelength negative index metamaterial working at RF with refractive index -109, surprisingly the previously recorded most extreme refractive index of only 38.6 [201]. Meanwhile, at optical frequencies, we propose a metamaterial-based beam splitter and realize polarizing, partially polarizing and non-polarizing properties, respectively.

¹The material contained in this chapter was previously published in Prog. Electromagn. Res. 152, 95 (2015). Refer Appendix A for granted permission to be published.

4.2 Extremely sub-wavelength negative index metamaterial

It is difficult to achieve extremely sub-wavelength negative index metamaterial due to the lack of extremely sub-wavelength metamaterial electric resonators. Here, we alleviate this problem by using an important strategy to reduce the effective plasma frequency of the metamaterial. This enables the metamaterial better impedance matched to free space. Such a strategy has not been applied to metamaterials before to achieve extremely sub-wavelength operation and an extreme refractive index.

4.2.1 Physical geometry

The unit cell of the sub-wavelength negative index metamaterial structure consists of three layers. The front side and the back side of a dielectric slab are a planar spiral and a planar meandering wire, respectively (see Fig. 4.1). The square spiral design has 60 turns, line width $w_1 = 200\mu\text{m}$, line spacing $g = 20\mu\text{m}$, center spacing $s = 2\text{mm}$, and the thickness of the spiral is $35\mu\text{m}$. The meandering wire design has 128 periods, line width $w_2 = 50\mu\text{m}$, meandering length $l = 29\text{mm}$, $h = 120\mu\text{m}$, and the thickness of the wire is $35\mu\text{m}$. The dielectric slab is $203\mu\text{m}$ thick and is modeled with a permittivity of $\epsilon = 2.6 + i0.04$. The square spiral and the meandering wire are made of copper

with a conductivity of $\sigma = 5.8 \times 10^7 \text{S/m}$. The dimension of the unit cell size is $30\text{mm} \times 30\text{mm} \times 20\text{mm}$. We used finite integration method based CST Microwave Studio software package to perform the simulation. The s-parameters corresponding to the complex reflection and transmission coefficients were calculated by using a frequency domain solver. Then the effective medium parameters of the metamaterial structure were retrieved by using the s-parameters [138]. Perfect electric conductor and perfect magnetic conductor boundary conditions were used in the simulations for the $x - z$ plane and the $x - y$ plane, respectively. We verified using periodic boundary conditions that the electromagnetic field cannot distinguish the lack of mirror symmetry in this specific structure [182]. We defined the incident electric field (E) along the y -axis to excite the parallel electric current oscillations in the meandering wire. Magnetic field (H) was along the z -axis to excite the magnetic resonant mode of the square spiral, and the propagation direction (k) was along the x -axis. We selected the tetrahedral meshes with an adaptive meshing method to accurately represent the model to be simulated.

4.2.2 Effective parameters and physical mechanisms

In this section, we show the results for the retrieved effective parameters of the metamaterial structure and explain the origins of magnetic and electric response of the proposed extremely sub-wavelength negative index metamaterial.

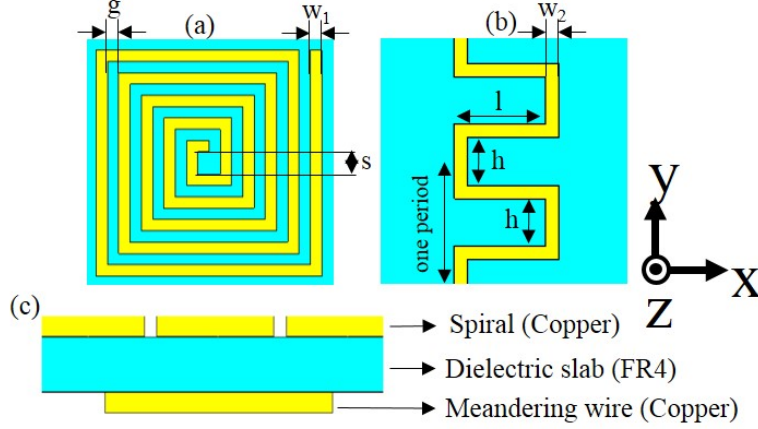


Figure 4.1: Schematic of the (a) spiral and (b) meandering wire structure with the geometric parameters indicated. (c) Side view of a small section of the structure showing material layers. Image taken from ref [5], [EMW Publishing].

A. Effective parameters

Figure 4.2(a) shows the resultant transmittance (T), reflectance (R), and absorbance (A). The spiral in the extremely sub-wavelength negative index metamaterial has 60 turns. In Fig. 4.2(b), we plot the retrieved effective refractive index, $n = n' + in''$. The negative refractive index bandwidth is 1.7MHz (ranging from 5.6MHz to 7.3MHz). At 5.8MHz, the real part of the refractive index reaches a record low of 108.6. Retrieved effective permittivity, $\epsilon = \epsilon' + i\epsilon''$, and permeability, $\mu = \mu' + i\mu''$, are shown in Figs. 4.2(c) and (d), respectively. Notice that around 5.7MHz, there is a magnetic resonance with a Lorentzian-like line-shape [141, 202]. The transmittance around resonance frequency is about 5%, the corresponding refractive index is 92, and the λ_0/a ratio is 1733. In the negative refractive index band, the transmittance is ranging from 4.5% to 7%, and the λ_0/a ratio is ranging between 1370 and 1782.

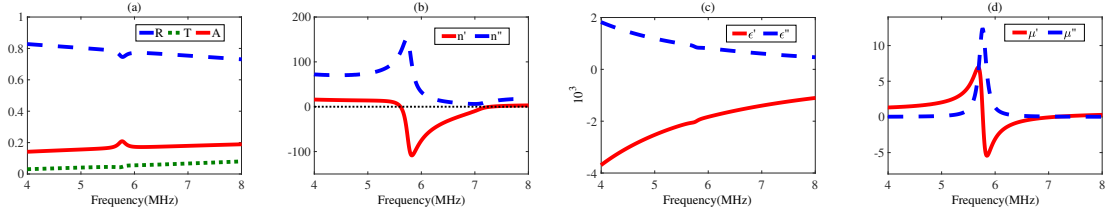


Figure 4.2: (a) Transmittance (T), reflectance (R), and absorbance (A) spectra. (b) Retrieved effective refractive index. (c) Effective permittivity, and (d) effective permeability. The spiral has 60 turns. Image taken from ref [5], [EMW Publishing].

The maximum figure of merit (FOM, defined as $-n'/n''$) is about 3 and more than 1 at $n' = -109$. These values are comparable with the low-loss (i.e., low absorption loss) metamaterials [135]. We should note that relatively poor impedance match here is a natural consequence of a large negative refractive index.

Figure 4.3 shows that both the impedance matching and the FOM can be further optimized by trading λ_0/a ratio and refractive index with improved transmittance resulting in an increase in the transmittance from 5% to 15% and a maximum FOM of about 4. The calculated absorption loss is about 1dB/cm, which is on the same order as [112]. The final structure retains the record values of λ_0/a ratio of about 1000 and $n' = -56$.

B. Magnetic response

The magnetic response arises from the planar square spiral. The spiral can be considered as an LC resonator with the resonance frequency $\omega_0 = 1/\sqrt{LC}$, where L is the

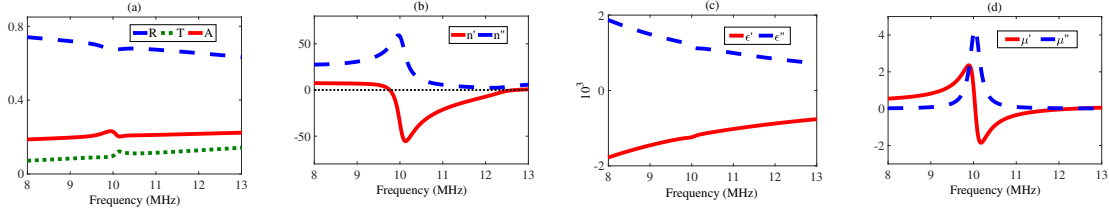


Figure 4.3: ((a) Transmittance (T), reflectance (R), and absorbance (A) spectra. (b) Retrieved effective refractive index. (c) Effective permittivity, and (d) effective permeability. The number of turns in the spiral is reduced to 40 turns to blue-shift the operating frequency of the negative index metamaterial. This enables the metamaterial relatively better impedance matched to free space. Image taken from ref [5], [EMW Publishing].

inductance due to the winding wires and C is the capacitance resulting from adjacent metallic windings [86]. Extremely sub-wavelength negative index metamaterials require sufficiently small magnetic resonance frequency. Therefore, L and C should be sufficiently large. By winding the significant length of wire into a small area, L is substantially increased. Additionally, decreasing the distance between the adjacent wires makes C increased. As shown in Fig. 4.2(d), the magnetic resonance frequency can be reduced down to around 5.7MHz, while the unit cell size along the propagation direction is only 30mm. This underlies the obtained large λ_0/a ratio.

Magnetic field and current density distributions near the magnetic resonance frequency for the structure considered in Fig. 4.2 are shown in Fig. 4.4. Fig. 4.4(a) shows the z component of magnetic field. The induced magnetic field is in the opposite direction with the incident magnetic field. In the central part of the spiral, the induced magnetic field is large enough to cancel the incident magnetic field. Therefore, the direction of the total magnetic field is dominated by the induced magnetic field.

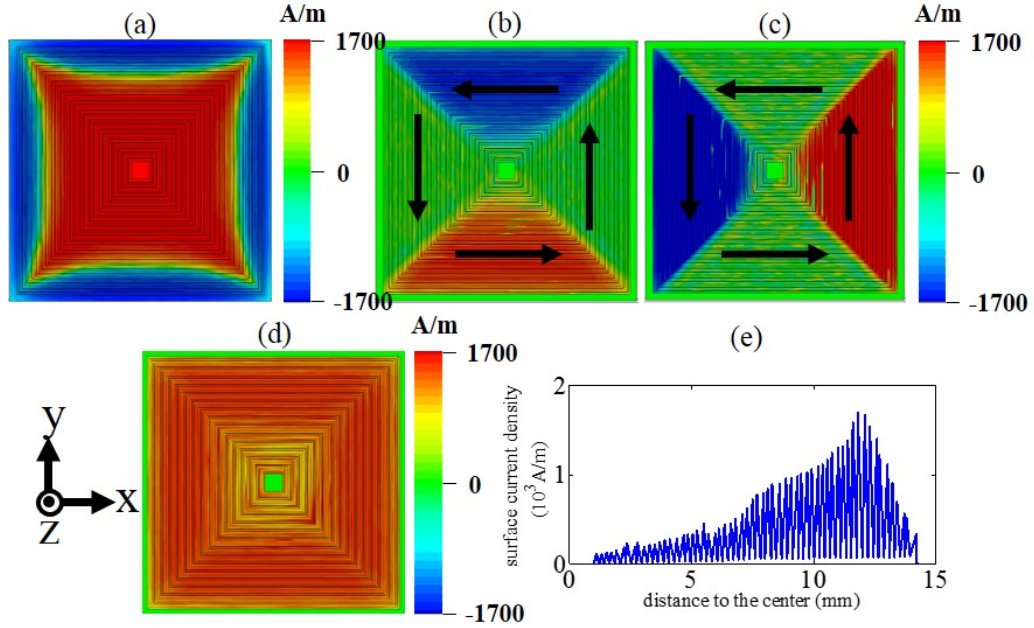


Figure 4.4: (a) Magnetic field at 5.7MHz in the structure considered in Fig. 4.2. Colors show the z-component of magnetic field H_z . (b) Corresponding current density distribution. Colors show the x-component of current density J_x . (c) The same as (b) except that colors show the y-component of current density J_y . The complete loop current is indicated by black arrows overlaying the current density plots in (b) and (c). (d) The magnitude of the current density and (e) its distribution along a line extending from the center of the spiral to the edge. Image taken from ref [5], [EMW Publishing].

However, at the outer edge, the induced magnetic field cannot cancel the incident magnetic field, thus revealing the diamagnetic response [202, 203] of the metamaterial. A circular current flow can be observed in Figs. 4.4(b) and (c). The magnitude of the current density is shown in Fig. 4.4(d). It can be seen in Fig. 4.4(e) that the current density first increases with the distance from the center of the spiral and then decreases toward the edge. The direction of the induced magnetic field is perpendicular to the current flow. This verifies that the magnetic response originates from the spiral structure.

C. Electric response

In the following we explain how we achieved the required electric response to obtain a measurable transmittance in the negative index band at an extremely sub-wavelength regime. We first point out the deficiency of commonly used straight continuous wire approach and then transform the straight wire into meandering wire for more favorable electric response.

1. Straight Continuous Wire

Initially, we used straight continuous wire on the backside of the dielectric substrate to obtain Drude-like negative permittivity. The wire length, width, and thickness were 30mm, $200\mu\text{m}$, and $35\mu\text{m}$, respectively. We kept the geometric parameters for the spiral and the dielectric slab the same as in Fig. 4.2. However, the transmittance was almost zero in the resonance frequency range as shown in Fig. 4.5. Low transmittance is due to the impedance mismatch. Around the resonance frequency, the impedance of the structure is $z = 0.02 - i0.02$, while the impedance of the background is 1. Thus, to improve the transmittance, the impedance of the structure should be as close as possible to 1. At this frequency, the effective permittivity is $\epsilon = -9111.7 - i5655.8$, and the effective permeability is $\mu = -4.7 + i6.7$. Negative imaginary part in ϵ is due to the deficiency of the HEM approximation at this wavelength (i.e., the structure is still not sufficiently sub-wavelength) [147, 148, 150, 152, 204].

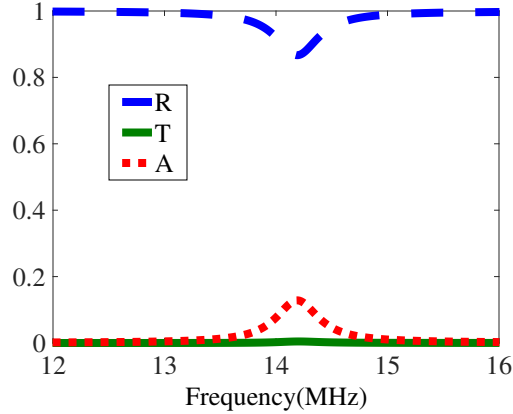


Figure 4.5: (Transmittance (T), reflectance (R), and absorbance (A) spectra for the metamaterial with straight continuous wire on the back side of the substrate. Image taken from ref [5], [EMW Publishing].

It is clear that, ideally, we need to bring the complex permittivity to the same order as the complex permeability for the impedance match. This can be achieved if the operating frequency is close to the diluted plasma frequency. Therefore, we need to red-shift the plasma frequency as much as possible toward the magnetic resonance frequency. With the straight wire on the back side, the plasma frequency is equal to 943MHz, while the magnetic resonance frequency is around 14MHz. It is worth mentioning that the resonance frequency is blue shifted in Fig. 4.5 compared to Fig. 4.2, this is due to decreased overlap (or coupling), between the straight wire and the spiral.

2. Meandering Wire

Below we show that the plasma frequency can be significantly reduced if we transform the straight wire into a meandering wire. This is the reason why we adopted

the meandering wire above to improve the transmittance of otherwise opaque metamaterial. We start with presenting the results for induced electric current density and then explain in detail how the meandering wire approach gives more desirable electric response.

The parameters of the meandering wire are shown in Fig. 4.1. In Fig. 4.2(a), we can clearly see that the transmittance in the case of the meandering wire improves in comparison with the case for the straight wire. The impedance around the magnetic resonance frequency is $z = 0.06 - i0.04$. Although the impedance is only slightly improved, the transmittance reaches from almost zero to about 5%. Because the induced non-resonant electric current on the meandering wire is much smaller than the induced resonant current on the spiral, it is difficult to clearly illustrate the non-resonant current. To address this problem, we first simulated the structure without spiral and obtained the electric current density shown in Fig. 4.6. Then, we compared the retrieved permittivity results with and without spiral and verified that the two plots are almost the same. This suggests that the current density distribution shown in Fig. 4.6 should also represent that of the negative index metamaterial structure discussed in Fig. 4.2.

Note that the induced non-resonant electric current density follows the trajectory of the meandering wire. As detailed below this is the essence of the reduced plasma frequency, hence improved transmittance.

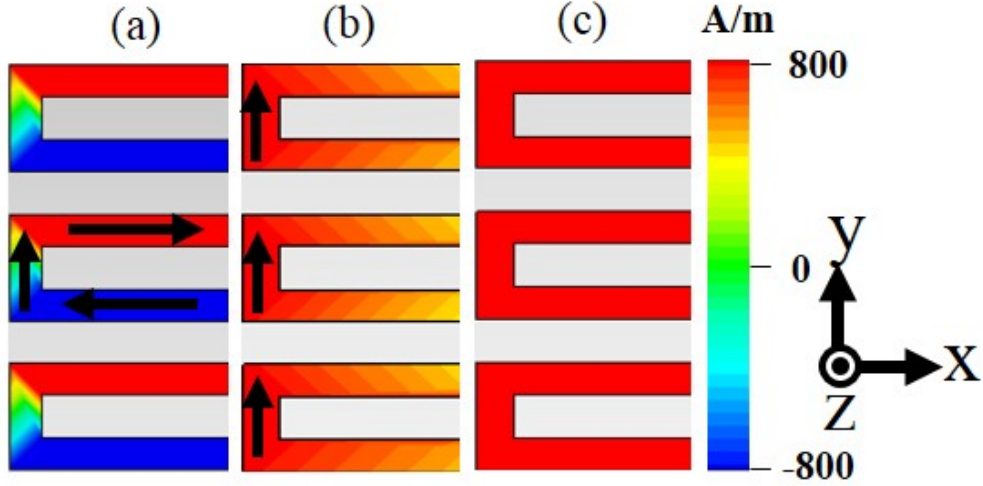


Figure 4.6: (a) Current density distribution on the meandering wire at 5.7MHz. Colors show the x-component of the current density J_x . (b) The same as (a) except that colors show the y-component of current density J_y . The arrows overlaying the surface plots in (a) and (b) indicate the non-resonant current which flows along the meandering wire. (c) The magnitude of the current density. Image taken from ref [5], [EMW Publishing].

The plasma frequency can be expressed as:

$$\omega_p = \sqrt{\frac{\rho_{eff} e^2}{\epsilon_0 m_{eff}}} \quad (4.1)$$

where ρ_{eff} is the effective electron density, m_{eff} is the effective mass of electrons, e is the elementary charge, $e = 1.602 \times 10^{-19} \text{C}$. ϵ_0 is the electric permittivity for vacuum, $\epsilon_0 = 8.854 \times 10^{-12} \text{F/m}$. We first calculate ρ_{eff} and m_{eff} for both straight and meandering wires [205]. We define the width of the wires as w_2 , the thickness as t , and the unit cell dimensions as $a \times a \times c$. For the straight wire, $\rho_{eff} = \rho w_2 t / ac$, where ρ is the electron density in the wire. $m_{eff} = e^2 N L_s$, where N is the total

electron number per unit length, $\rho N = w_2 t$. L_s is the self-inductance per unit length, $L_s = (\mu_0/2\pi) \ln(a/w_2)$. For the meandering wire, both the effective electron density and mass change. Since meandering wire contains horizontal parts, the effective electron density becomes $\rho'_{eff} = \rho_{eff}(1 + 2lm/a)$, where m is the number of periods of the meandering wire and l is the length of the horizontal parts (see Fig. 4.1). On the other hand, we obtain the electron number per unit length and the self-inductance per unit length as $N' = N(1 + 2lm/a)$, $L'_s = L_s(1 + 2lm/a)$, respectively. Then, the effective mass of the electrons becomes $m'_{eff} = m_{eff}(1 + 2lm/a)^2$. Finally, we can relate the plasma frequency of these two wires by:

$$\frac{\omega'_p}{\omega_p} = \frac{1}{\sqrt{1 + \frac{2lm}{a}}} \quad (4.2)$$

Below we compare the CST simulation results with the analytical result. To obtain the optimal design for the meandering wire structure, we began with a small number of periods and l value, then gradually increased the number of periods and l . Table 4.1 shows 17 sets of parameters enumerated by N_o . Each set corresponds to one particular plasma frequency ω_p . The numerical results for ω'_p/ω_p in Table 4.1 were obtained from the CST simulations, while the analytical results were obtained from Eq. 4.2. Both results are plotted in Fig. 4.7. The red solid line is the simulation result and black dashed line is the analytical result. We find an excellent agreement between both results. Thus, Eq. 4.2 and Fig. 4.7 show clearly that the plasma frequency can be

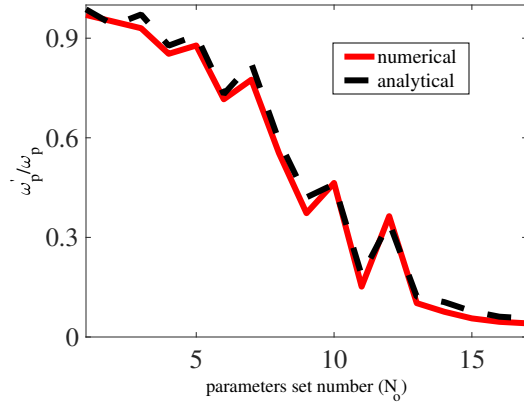


Figure 4.7: Graphical comparison of numerical and analytical results in Table 1 for ω'_p/ω_p . Image taken from ref [5], [EMW Publishing].

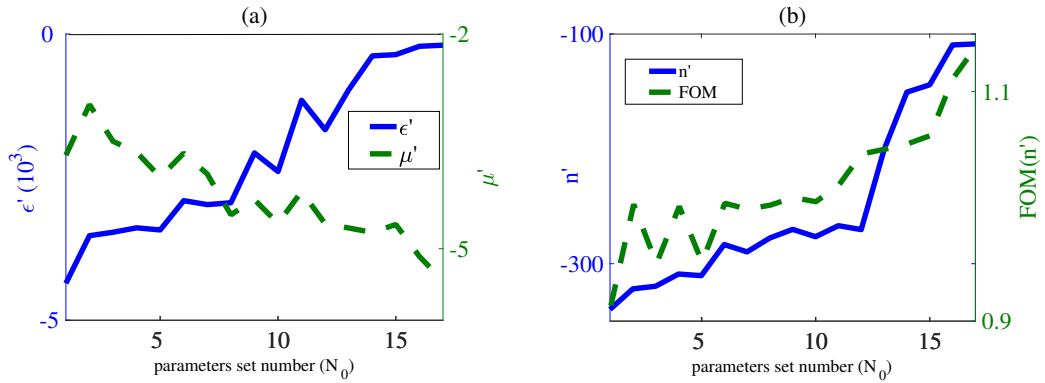


Figure 4.8: (a) Effective permittivity and permeability using the meandering wire parameters in Table 4.1. (b) The attainable most extreme refractive index and the corresponding FOM. The geometrical parameters for the spiral are the same as in Fig. 4.2. Image taken from ref [5], [EMW Publishing].

significantly reduced by replacing the straight wire with the meandering wire. For the particular designs studied here, the plasma frequency reduces from 943MHz to below 53MHz. Increasing especially the number of periods and the length of horizontal parts plays an important role in the reduced plasma frequency by increasing the effective mass of the electrons. The transmittance can be increased by further optimization of the structure.

Table 4.1

Numerical and analytical results for ω'_p/ω_p using different meandering wire parameters; N_o is used to enumerate the parameter sets, m is the number of periods and l is the length of horizontal parts in nm.

N_o	m	$l/2$	numerical	analytical
1	1	0.4	0.977	0.9869
2	1	2	0.95	0.9303
3	2	0.4	0.93	0.9714
4	2	2	0.853	0.8776
5	4	0.4	0.878	0.9084
6	4	2	0.716	0.7319
7	8	0.4	0.775	0.8237
8	8	2	0.554	0.5912
9	8	5	0.373	0.4206
10	16	2	0.464	0.4602
11	16	10	0.1517	0.1858
12	32	2	0.3639	0.3442
13	32	10	0.102	0.1217
14	64	10	0.076	0.1051
15	64	14	0.056	0.0775
16	128	14	0.0457	0.0611
17	128	14.5	0.0412	0.0561

The geometrical parameters presented in Table 4.1 are the most effective geometrical parameters to reduce the plasma frequency as can be seen from Eq. 4.2. In Fig. 4.8 we show how these geometrical parameters affect the effective constitutive parameters, the attainable most extreme refractive index, and the corresponding FOM. Because the plasma frequency does not smoothly decrease with the geometrical parameters in Table 4.1 (see also Fig. 4.7), the plots in Fig. 4.8 also do not follow a smooth pattern. However, overall trend is that as the plasma frequency decreases ϵ shifts upward, μ becomes more negative, n becomes less negative, and the FOM improves. Note that it is possible to obtain n below 300 at the expense of lower FOM and higher impedance

mismatch.

4.3 Metamaterial-based beam splitter

A beam splitter is an important optical component used to split a beam of incident light at a desired ratio into two separate beams. The beam splitter can be classified into three kinds according to the input and output polarizations: polarizing beam splitter (PBS), partially polarizing beam splitter (PPBS), and non-polarizing beam splitter (NPBS).

One can design a PBS to split light into reflected TE/TM-polarization and transmitted TM/TE-polarization. Here TE-polarized means electric field is perpendicular to the plane of incidence, and TM-polarized means electric field is parallel with the plane of incidence. PBS can split unpolarized light at a 50/50 ratio, which makes it an essential element in polarization based imaging system [206], free-space optical switching networks [207], and read-write magneto-optical data storage systems [208]. NPBS can split the light at a specific R/T ratio, at the same time, the original polarization state of the incident light is still maintained. NPBS is widely used in interferometers. Between polarizing and non-polarizing is PPBS. For example, an important application of PPBS is that it is a key component to realize the quantum controlled-NOT (CNOT) gate [209], an essential gate in the construction of a

photonic quantum computer. By using a combination of CNOT gate and single qubit rotations, we can build any quantum circuit to an arbitrary degree of accuracy [210].

So far, the three different beam splitters have been realized by different structures. Inspired by the sub-wavelength unit cell size and arbitrarily controlled electromagnetic response, metamaterial-based beam splitters are promising to form compact and functional photonic devices. Here, we proposed a scheme to realize three classes of beam splitters under different geometries of fishnet structures. These beam splitters are all designed to operate at $1.55\mu\text{m}$ since $1.55\mu\text{m}$ is the most widely used wavelength in optical communication systems, where the absorption of glass material used in fiber is small.

4.3.1 Fishnet metamaterial

We design different beam splitters based on the fishnet metamaterial in ref [142]. The unit cell as shown in Fig. 4.9 consists of three layers made by Ag-MgF₂-Ag. t_{Ag} and t_{MgF_2} represent the thickness of Ag layer and MgF₂ layer, respectively. The wire widths of the fishnet structure along the x and y directions are w_x and w_y , respectively. The periods are Λ_x and Λ_y and the structure is embedded in air. The Drude model is used to describe the permittivity of Ag,

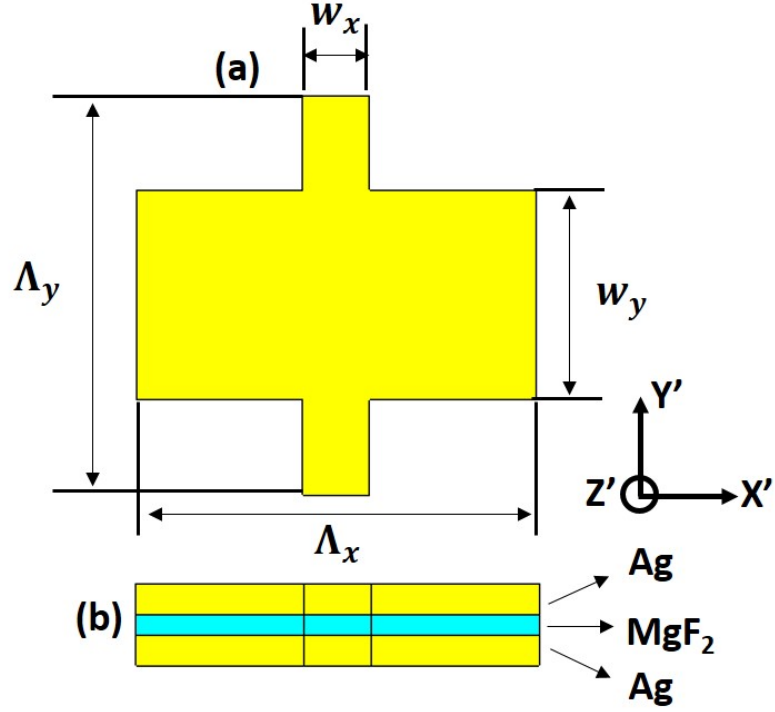


Figure 4.9: Schematic of the (a) fishnet structure with the geometric parameters indicated. (b) Side view of the structure showing material layers.

$$\epsilon_{Ag} = 1 - \frac{\omega_p^2}{\omega(\omega + i\omega_c)} \quad (4.3)$$

where the plasma frequency is $\omega_p = 1.37 \times 10^{16} s^{-1}$, and the collision frequency is $\omega_c = 8.5 \times 10^{13} s^{-1}$. The refractive index of MgF_2 is 1.38.

In the following parts, we will show different beam splitter designs by changing the geometry of the fishnet structures.

4.3.2 Polarizing beam splitter

By manipulating the transmission and reflection, PBS is obtained. The geometric parameters are $w_x = 400\text{nm}$, $w_y = 50\text{nm}$, $\Lambda_x = 600\text{nm}$, $\Lambda_y = 600\text{nm}$, $t_{Ag} = 15\text{nm}$, and $t_{MgF_2} = 30\text{nm}$. The electromagnetic wave comes to the fishnets at 45° oblique incidence. Fig. 4.10 shows the electric field distribution of the incident field, reflected field and transmitted field, respectively. TM-polarized light (E_x component) is transmitted as shown in Fig. 4.10 (a), and TE-polarized light (E_y component) is reflected as shown in Fig. 4.10 (b). The designed fishnet structure achieves the goal of polarization splitting.

To explore the performance of this PBS, extinction ratio and insertion loss are calculated by Eq. 4.4 and 4.5. Extinction ratio for TE-polarization ER_r is the ratio of TE-polarization reflectance (R_{TE}) to TM-polarization reflectance (R_{TM}). Extinction ratio for TM-polarization ER_t is the ratio of TM-polarization transmittance (T_{TM}) to TE-polarization transmittance (T_{TE}). Insertion loss for TE and TM polarized light are represented by IL_r and IL_t , respectively.

$$\begin{cases} ER_r = \frac{R_{TE}}{R_{TM}} \\ ER_t = \frac{T_{TM}}{T_{TE}} \end{cases} \quad (4.4)$$

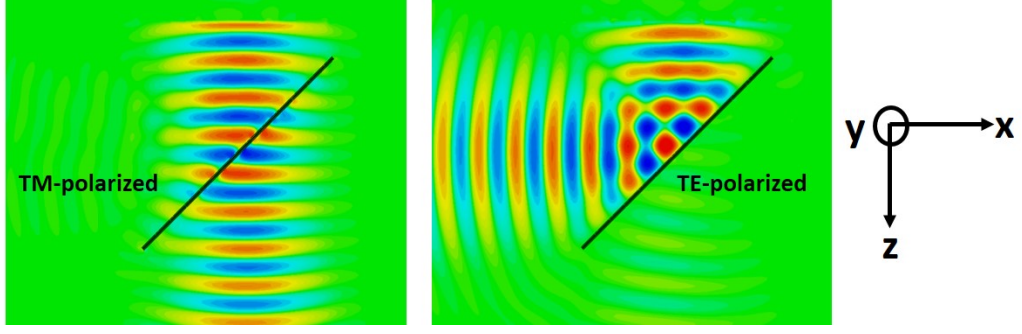


Figure 4.10: (a) x-component of Electric field E_x and (b) y-component of electric field E_y at $1.55\mu\text{m}$.

$$\begin{cases} IL_r = \frac{1}{R_{TE}} \\ IL_t = \frac{1}{T_{TM}} \end{cases} \quad (4.5)$$

And then we express them in dB, the result is $ER_r = 22.5\text{dB}$, $ER_t = 14.5\text{dB}$, $IL_r = 0.25\text{dB}$, and $IL_t = 0.26\text{dB}$. Compared with other PBS designs [211, 212, 213], these values indicate the good performance of our designed PBS.

Below we will show physics of polarizing splitting. Following the retrieval procedure described in ref [142], we can calculate the effective impedance of this beam splitter under different polarization incidence. Fig. 4.11 shows the effective impedance ($Z = Z' + iZ''$) under TE-polarized light and TM-polarized light incidence, respectively. Under TE-polarized incidence, the real part of effective impedance is almost 0 around 193THz ($1.55\mu\text{m}$), while the impedance of the background material air is 1. So the extreme impedance mismatch appears, which leads to the phenomenon that almost all the electromagnetic waves are reflected rather than transmitted. In contrast, when a

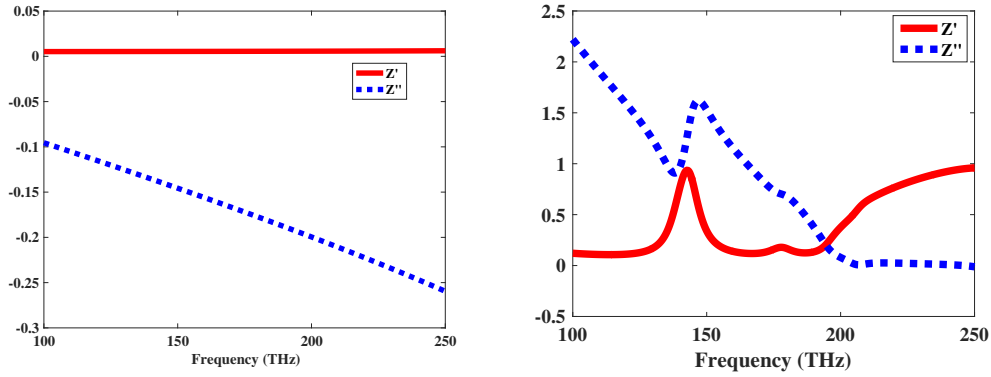


Figure 4.11: Effective impedance under (a) TE-polarized and (b) TM-polarized incident light.

TM-polarized light comes to the structure, the real part of the effective impedance is 0.2 around 193THz, which is much larger than the one under TE-polarized incidence. The impedance mismatched effect reduced, so that most of the electromagnetic waves can be transmitted. However, since the effective impedance is not equal to 1, so there are still some reflected waves. Meanwhile, we should notice that the absorption always exists in the metamaterials produced by metal components, so it is impossible to obtain zero insertion loss.

4.3.3 Partially polarizing beam splitter

The desired splitting ratio of PPBS that can be used to realize CNOT gate is the following: 100% reflection of TE-polarized light, 1/3 reflection of TM-polarized light, and 2/3 transmission of TM-polarized light. We begin with the geometry of PBS, and then optimize the structure to satisfy the requirement. The geometric parameters to

obtain the required PPBS are $w_x = 260\text{nm}$, $w_y = 140\text{nm}$, $\Lambda_x = 600\text{nm}$, $\Lambda_y = 560\text{nm}$, $t_{Ag} = 15\text{nm}$, and $t_{MgF_2} = 30\text{nm}$. The reflectance and transmittance calculated through simulations are $R = 0.75$, $T = 0.02$ for TE-polarized light, and $R = 0.25$, $T = 0.5$ for TM-polarized light. Since there is always absorbance inside the structure, we cannot obtain the ideal transmittance and reflectance. However, we need to point out that in order to achieve the same probability output under different polarization, the transmittance and reflectance for TE and TM polarization should scale down with the same scale factor from the ideal case, respectively.

4.3.4 Non-polarizing beam splitter

NPBS is achieved by the same length of wires along the x and y directions (i.e., $w_x = w_y$), and the same period (i.e., $\Lambda_x = \Lambda_y$). We can obtain arbitrary splitting ratio by changing w_x and Λ_x . Fig. 4.12 shows the reflectance (R), transmittance (T), and absorbance (A) plot as a function of different geometric parameters at $1.55\mu\text{m}$. Fig. 4.12 (a) shows the results by changing w_x at $\Lambda_x = 600\text{nm}$ and (b) shows the results by changing Λ_x at $w_x = 100\text{nm}$. The thickness of Ag and MgF_2 are $t_{Ag} = 45\text{nm}$, and $t_{MgF_2} = 30\text{nm}$, respectively. We should notice that the absorbance is always small, around 0.05 under different geometries, which indicates a good efficiency. The large range of reflectance and transmittance provides the opportunity to use this NPBS under different application requirements.

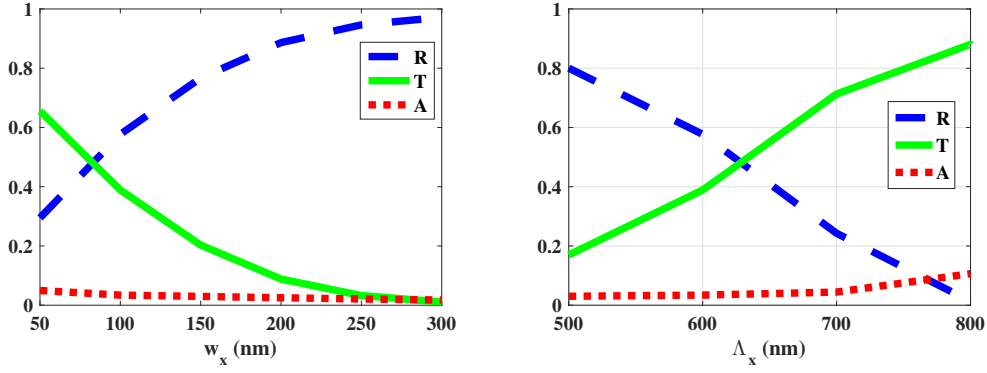


Figure 4.12: Reflectance (R), transmittance (T), and absorbance (A) spectra versus (a) w_x , and (b) Λ_x .

4.4 Conclusion

In summary, we propose an extremely sub-wavelength NIM operating at radio frequencies and a metamaterial-based beam splitter operating at optical frequencies. The $\lambda/a = 1733$ is obtained around the resonance frequency for extremely sub-wavelength NIM. Furthermore, the refractive index reaches down to -109. The extreme refractive index can be useful in transformation optics, high-resolution imaging, and enhanced light-matter interaction. For beam splitter, three classes of beam splitters are achieved by changing the geometric parameters, and the $\lambda/a = 25.8$ for PBS and PPBS, $\lambda/a = 13$ for NPBS are obtained at $1.55\mu\text{m}$. The designed NIM and beam splitter can be used to integrate with other components for a compact device.

Chapter 5

Summary and future work

5.1 Summary

In Chapter 1, we first introduced the definition, basic properties, and applications of metamaterials. Moreover, we reviewed the critical challenges that prevent the broader impact of metamaterials, which leads to two research objectives: towards truly 3D bulk photonic metamaterials and compensation of losses. In addition, metamaterials can be considered as the potential solution to address the challenges in other device level applications, which leads to the third research objective: miniaturization of RF and optical components with metamaterials.

DLW technique has the potential to fabricate 3D and large-scale metamaterials. In

chapter 2, we briefly introduced the DLW technique, and then proposed a hyperbolic metamaterial and an air waveguide with negative index cladding that have the potential to be fabricated with STED-DLW. In the hyperbolic metamaterial section, we studied three different magnetic dipoles which can contribute to hyperbolic dispersion. In addition, we showed the preliminary fabrication results provided by Dr. Martin Wegener's research group. In the waveguide section, we studied the effect of the absorption loss on the dispersion relations of the lossy waveguide. Under three different loss cases, we analytically calculated the dispersion relations and numerically analyzed the field distributions. A practical negative index metamaterial was chosen as an optical parameters guidance, and we concluded that it is difficult to trap the light in the waveguide with realistic losses. Since DLW is unable to fabricate vertical disconnected structure, we finally showed that direct laser metal writing technique has the potential to fabricate disconnected metal features.

In chapter 3, we addressed the problem about the resolution limitation of the diffraction unlimited lens due to the losses during the imaging process. The plasmon injection (II) scheme loss compensation technique was briefly introduced. We extended this II scheme to the hyperlens and magnifying superlens. In addition, we analytically described the entire process of the inverse filter technique emulating the II scheme and demonstrated the equivalence of the II scheme and the inverse filter. Three major loss mechanisms including absorption loss, discretization loss, and impedance mismatch loss were identified and studied separately, and we found that II scheme can

compensate all of these loss mechanisms responsible for the deterioration of the image resolution. By compensating the losses in the experimental hyperlens, the resolution enhanced from $\lambda/3$ to $\lambda/7$. For magnifying superlens, FWHM is reduced from 70nm down to 61nm by Π scheme.

Due to the sub-wavelength property of metamaterials, they are envisioned as the next-generation materials for compact circuits. We proposed an extremely sub-wavelength NIM working at RF and a metamaterial-based beam splitter working at optical frequencies in Chapter 4. We explored the idea of achieving magnetic resonance at radio frequencies and addressed the impedance mismatch problem. We analytically described the change of the plasma frequency from the meandering wire to the straight wire. We reported a record negative refractive index -109 at the extremely large λ_0/a ratio. In the beam splitter section, by manipulating the transmittance and reflectance of the fishnet structure through changing the geometry, three kinds of beam splitters including PBS, PPBS and NPBS are accomplished. The extinction ratio for reflection and transmission of PBS is 22.5dB and 14.5dB, respectively, and the insertion loss for reflection and transmission is 0.25dB and 0.26dB, respectively, which indicates good performance. PPBS designed in chapter 4 can be used to integrate with other optical devices to realize a CNOT gate. The desired transmittance and reflectance for different polarizations are obtained. NPBS with the arbitrary splitting ratio is achieved, and the absorbance is 0.05 at a designed working wavelength of $1.55\mu\text{m}$.

5.2 Future work

5.2.1 Far-field hyperlens imaging enhanced by incoherent active convolved illumination

Inspired by the plasmon injection loss compensation technique, our group members developed new research directions. Wyatt Adams and Anindya Ghoshroy are working on an active plasmon injection scheme with both coherent and incoherent light excitation [214, 215, 216, 217].

The plasmon injection scheme studied in Chapter 3 is under coherent light excitation. For hyperlenses and plasmonic superlenses, both the amplitude and phase information are needed to compensate the loss. However, it becomes difficult to detect the phase information, especially at visible frequencies. Adams et al. showed that by illuminating with incoherent light, real-valued intensity data rather than complex field information is sufficient to reconstruct an image from a silver plasmonic superlens [214]. In addition, although the passive inverse filter mentioned in chapter 3 compensates the loss in the image, it also amplifies the noise. If the high spatial frequency features are not distinguishable under noise, the compensated image will lose the high spatial frequency information. Ghoshroy et al. applied a physical auxiliary object to recover high spatial frequency components buried under the noise. With a convolved

auxiliary object, the object spectrum in the frequency domain was selectively amplified. They successfully applied this active plasmon injection scheme to imperfect negative index flat lens [215].

By combining these two directions, the resolution of the near-field silver superlens can achieve $\lambda/15$ or better under incoherent active convolved illumination [218]. Future work would be extending this incoherent active convolved illumination to experimental hyperlens and magnifying superlens to obtain ultra-high resolution image without using phase information and far beyond the previous passive implementation in Chapter 3. Exploring the possibility of applying this active plasmon injection scheme to other applications beyond the imaging is also an important avenue.

5.2.2 Toolbox for compact photonic integrated circuits

At present, great attention is paid to make high-density integration and high-level functionality PIC. Metadevices have the potential to achieve this goal since they are compact, advanced and can be multi-functional. The metamaterial-based beam splitter is an example to show that metamaterials can be potentially more favorable than conventional materials for high-density integration and high-level functionality PIC. So that metamaterials can be envisioned as the next-generation materials, and future work would be the design of metadevices for substituting conventional optical devices in the fields of optical communication, sensing and quantum computing.

References

- [1] Zhang, X.; Debnath, S.; Güney, D. Ö. *JOSA B* **2015**, *32*(6), 1013–1021.
- [2] Lee, H.; Liu, Z.; Xiong, Y.; Sun, C.; Zhang, X. *Optics express* **2007**, *15*(24), 15886–15891.
- [3] Zhang, X.; Adams, W.; Sadatgol, M.; Güney, D. Ö. *Progress In Electromagnetics Research C* **2016**, *70*, 1–7.
- [4] Zhang, X.; Adams, W.; Güney, D. Ö. *JOSA B* **2017**, *34*(6), 1310–1318.
- [5] Zhang, X.; Usi, E.; Khan, S. K.; Sadatgol, M.; Güney, D. O. *Progress In Electromagnetics Research* **2015**, *152*, 95–104.
- [6] Hapgood, F.; Grant, A. *Discover*, <http://discovermagazine.com/2009/apr/10-metamaterial-revolutionnew-science-making-anything-disappear> (accessed 4/21/2009) **2009**.
- [7] Shelby, R. A.; Smith, D. R.; Schultz, S. *science* **2001**, *292*(5514), 77–79.

- [8] Smith, D.; Schurig, D. *Physical Review Letters* **2003**, *90*(7), 077405.
- [9] Pendry, J. B. *Physical review letters* **2000**, *85*(18), 3966.
- [10] Hyperlens, O. *Optics express* **2006**, *14*(18), 8247–56.
- [11] Liu, Z.; Lee, H.; Xiong, Y.; Sun, C.; Zhang, X. *science* **2007**, *315*(5819), 1686–1686.
- [12] Landy, N. I.; Sajuyigbe, S.; Mock, J.; Smith, D.; Padilla, W. *Physical review letters* **2008**, *100*(20), 207402.
- [13] Aydin, K.; Ferry, V. E.; Briggs, R. M.; Atwater, H. A. *Nature communications* **2011**, *2*, ncomms1528.
- [14] Bulu, I.; Caglayan, H.; Aydin, K.; Ozbay, E. *New Journal of Physics* **2005**, *7*(1), 223.
- [15] Odabasi, H.; Teixeira, F.; Guney, D. *Journal of Applied Physics* **2013**, *113*(8), 084903.
- [16] Pendry, J. B.; Schurig, D.; Smith, D. R. *science* **2006**, *312*(5781), 1780–1782.
- [17] Leonhardt, U. *Science* **2006**, *312*(5781), 1777–1780.
- [18] Schurig, D.; Mock, J.; Justice, B.; Cummer, S. A.; Pendry, J. B.; Starr, A.; Smith, D. *Science* **2006**, *314*(5801), 977–980.

- [19] Vora, A.; Gwamuri, J.; Pala, N.; Kulkarni, A.; Pearce, J. M.; Güney, D. Ö. *Scientific reports* **2014**, *4*.
- [20] Liu, N.; Fu, L.; Kaiser, S.; Schweizer, H.; Giessen, H. *Advanced Materials* **2008**, *20*(20), 3859–3865.
- [21] García-Meca, C.; Hurtado, J.; Martí, J.; Martínez, A.; Dickson, W.; Zayats, A. V. *Physical review letters* **2011**, *106*(6), 067402.
- [22] Zhang, S.; Fan, W.; Panoiu, N.; Malloy, K.; Osgood, R.; Brueck, S. *Physical review letters* **2005**, *95*(13), 137404.
- [23] Zhou, Y.; Chen, X.; Fu, Y.; Vienne, G.; Kuznetsov, A.; Luk?Yanchuk, B. *Applied Physics Letters* **2013**, *103*(12), 123116.
- [24] Kehagias, N.; Reboud, V.; Chansin, G.; Zelsmann, M.; Jeppesen, C.; Schuster, C.; Kubenz, M.; Reuther, F.; Gruetzner, G.; Torres, C. S. *Nanotechnology* **2007**, *18*(17), 175303.
- [25] Wu, W.; Yu, Z.; Wang, S.-Y.; Williams, R. S.; Liu, Y.; Sun, C.; Zhang, X.; Kim, E.; Shen, Y. R.; Fang, N. X. *Applied physics letters* **2007**, *90*(6), 063107.
- [26] Soukoulis, C. M.; Wegener, M. *nature photonics* **2011**, *5*(9), 523.
- [27] Tanaka, T.; Ishikawa, A. *Nano Convergence* **2017**, *4*(1), 34.

- [28] Sydoruk, O.; Radkovskaya, A.; Zhuromskyy, O.; Shamonina, E.; Shamonin, M.; Stevens, C.; Faulkner, G.; Edwards, D.; Solymar, L. *Physical Review B* **2006**, *73*(22), 224406.
- [29] Kaschke, J.; Wegener, M. *Nanophotonics* **2016**, *5*(4), 510–523.
- [30] Aieta, F.; Genevet, P.; Kats, M. A.; Yu, N.; Blanchard, R.; Gaburro, Z.; Capasso, F. *Nano letters* **2012**, *12*(9), 4932–4936.
- [31] Smith, D. R.; Yurduseven, O.; Mancera, L. P.; Bowen, P.; Kundtz, N. B. *Physical Review Applied* **2017**, *8*(5), 054048.
- [32] Chang, Y.-C.; Kildishev, A. V.; Narimanov, E. E.; Norris, T. B. *Physical Review B* **2016**, *94*(15), 155430.
- [33] Zheng, Y.; Zhou, Y.; Gao, J.; Cao, X.; Yang, H.; Li, S.; Xu, L.; Lan, J.; Jidi, L. *Scientific reports* **2017**, *7*(1), 16137.
- [34] Smith, D. R.; Schurig, D.; Rosenbluth, M.; Schultz, S.; Ramakrishna, S. A.; Pendry, J. B. *Applied Physics Letters* **2003**, *82*(10), 1506–1508.
- [35] Agarwal, K.; Liu, C.; Joung, D.; Park, H.-R.; Oh, S.-H.; Cho, J.-H. *Scientific Reports* **2017**, *7*(1), 2680.
- [36] Miyamaru, F.; Hangyo, M. *Applied physics letters* **2006**, *89*(21), 211105.
- [37] Oh, S. S.; Hess, O. *Nano Convergence* **2015**, *2*(1), 24.

- [38] Cao, T.; Wei, C.-w.; Li, Y. *Optical Materials Express* **2016**, *6*(2), 303–311.
- [39] Plum, E.; Fedotov, V.; Zheludev, N. *Applied physics letters* **2008**, *93*(19), 191911.
- [40] Urbas, A. M.; Jacob, Z.; Dal Negro, L.; Engheta, N.; Boardman, A.; Egan, P.; Khanikaev, A. B.; Menon, V.; Ferrera, M.; Kinsey, N.; others. *Journal of Optics* **2016**, *18*(9), 093005.
- [41] Kaschke, J.; Blume, L.; Wu, L.; Thiel, M.; Bade, K.; Yang, Z.; Wegener, M. *Advanced Optical Materials* **2015**, *3*(10), 1411–1417.
- [42] Bagheri, S.; Zgrabik, C. M.; Gissibl, T.; Tittl, A.; Sterl, F.; Walter, R.; De Zuani, S.; Berrier, A.; Stauden, T.; Richter, G.; others. *Optical Materials Express* **2015**, *5*(11), 2625–2633.
- [43] Faniayeu, I.; Mizeikis, V. *Optical Materials Express* **2017**, *7*(5), 1453–1462.
- [44] Mizeikis, V.; Chatterjee, S.; Faniayeu, I. In *Advanced Fabrication Technologies for Micro/Nano Optics and Photonics XI*, Vol. 10544, page 105440X. International Society for Optics and Photonics, 2018.
- [45] Cheng, Y.; Nie, Y.; Gong, R. *The European Physical Journal B* **2012**, *85*(2), 62.
- [46] Fang, F.; Cheng, Y.; Liao, H. *Physica Scripta* **2014**, *89*(2), 025501.

- [47] Vier, D.; Schultz, S.; Gregor, R.; Parazzoli, C.; Nielsen, J.; Tanielian, M. *IET microwaves, antennas & propagation* **2009**, *3*(5), 723–727.
- [48] Rudolph, S. M.; Grbic, A. *IEEE Transactions on Antennas and Propagation* **2012**, *60*(8), 3661–3669.
- [49] Güney, D. Ö.; Koschny, T.; Soukoulis, C. M. *Optics express* **2010**, *18*(12), 12348–12353.
- [50] Burckel, D. B.; Wendt, J. R.; Ten Eyck, G. A.; Ginn, J. C.; Ellis, A. R.; Brener, I.; Sinclair, M. B. *Advanced Materials* **2010**, *22*(44), 5053–5057.
- [51] Verhagen, E.; de Waele, R.; Kuipers, L.; Polman, A. *Physical review letters* **2010**, *105*(22), 223901.
- [52] Yang, S.; Ni, X.; Kante, B.; Zhu, J.; O’Brien, K.; Wang, Y.; Zhang, X. In *Lasers and Electro-Optics (CLEO), 2016 Conference on*, pages 1–2. IEEE, 2016.
- [53] Zheng, X.; Smith, W.; Jackson, J.; Moran, B.; Cui, H.; Chen, D.; Ye, J.; Fang, N.; Rodriguez, N.; Weisgraber, T.; others. *Nature materials* **2016**, *15*(10), 1100.
- [54] Reza, A.; Dignam, M.; Hughes, S. *Nature* **2008**, *455*(7216), E10–E11.
- [55] Lee, D. A.; Vedral, L. J.; Smith, D. A.; Musselman, R. L.; Pinchuk, A. O. *AIP Advances* **2015**, *5*(4), 047119.
- [56] Jahani, S.; Jacob, Z. *Nature nanotechnology* **2016**, *11*(1), 23.

- [57] Staude, I.; Miroshnichenko, A. E.; Decker, M.; Fofang, N. T.; Liu, S.; Gonzales, E.; Dominguez, J.; Luk, T. S.; Neshev, D. N.; Brener, I.; others. *ACS nano* **2013**, *7*(9), 7824–7832.
- [58] Evlyukhin, A. B.; Novikov, S. M.; Zywiets, U.; Eriksen, R. L.; Reinhardt, C.; Bozhevolnyi, S. I.; Chichkov, B. N. *Nano letters* **2012**, *12*(7), 3749–3755.
- [59] Lepetit, T.; Akmansoy, E.; Ganne, J.-P. *Applied Physics Letters* **2009**, *95*(12), 121101.
- [60] Marcellin, S.; Akmansoy, É. In *Advanced Electromagnetic Materials in Microwaves and Optics (METAMATERIALS), 2015 9th International Congress on*, pages 4–6. IEEE, 2015.
- [61] Moitra, P.; Yang, Y.; Anderson, Z.; Kravchenko, I. I.; Briggs, D. P.; Valentine, J. *Nature Photonics* **2013**, *7*(10), 791.
- [62] Kita, S.; Li, Y.; Camayd-Muñoz, P.; Reshef, O.; Vulis, D. I.; Day, R. W.; Mazur, E.; Lončar, M. *Optics Express* **2017**, *25*(7), 8326–8334.
- [63] Moitra, P.; Slovick, B. A.; Li, W.; Kravchenko, I. I.; Briggs, D. P.; Krishnamurthy, S.; Valentine, J. *ACS Photonics* **2015**, *2*(6), 692–698.
- [64] Zhao, Y.; Li, B.; Lan, C.; Bi, K.; Qu, Z. *Optics express* **2017**, *25*(18), 22158–22163.

- [65] Esfandyarpour, M.; Garnett, E. C.; Cui, Y.; McGehee, M. D.; Brongersma, M. L. *Nature nanotechnology* **2014**, *9*(7), 542.
- [66] Ma, Z.; Hanham, S. M.; Albella, P.; Ng, B.; Lu, H. T.; Gong, Y.; Maier, S. A.; Hong, M. *ACS Photonics* **2016**, *3*(6), 1010–1018.
- [67] Krasnok, A. E.; Miroshnichenko, A. E.; Belov, P. A.; Kivshar, Y. S. *JETP letters* **2011**, *94*(8), 593–598.
- [68] Decker, M.; Staude, I.; Falkner, M.; Dominguez, J.; Neshev, D. N.; Brener, I.; Pertsch, T.; Kivshar, Y. S. *Advanced Optical Materials* **2015**, *3*(6), 813–820.
- [69] Arbabi, A.; Horie, Y.; Bagheri, M.; Faraon, A. *Nature nanotechnology* **2015**, *10*(11), 937–943.
- [70] Fattal, D.; Li, J.; Peng, Z.; Fiorentino, M.; Beausoleil, R. G. *Nature Photonics* **2010**, *4*(7), 466.
- [71] West, P. R.; Stewart, J. L.; Kildishev, A. V.; Shalaev, V. M.; Shkunov, V. V.; Strohkendl, F.; Zakharenkov, Y. A.; Dodds, R. K.; Byren, R. *Optics express* **2014**, *22*(21), 26212–26221.
- [72] Shalaev, M. I.; Sun, J.; Tsukernik, A.; Pandey, A.; Nikolskiy, K.; Litchinitser, N. M. *Nano letters* **2015**, *15*(9), 6261–6266.
- [73] Desiatov, B.; Mazurski, N.; Fainman, Y.; Levy, U. *Optics Express* **2015**, *23*(17), 22611–22618.

- [74] Baranov, D. G.; Zuev, D. A.; Lepeshov, S. I.; Kotov, O. V.; Krasnok, A. E.; Evlyukhin, A. B.; Chichkov, B. N. *Optica* **2017**, *4*(7), 814–825.
- [75] Rhee, J.; Yoo, Y.; Kim, K.; Kim, Y.; Lee, Y. *Journal of Electromagnetic Waves and Applications* **2014**, *28*(13), 1541–1580.
- [76] Chen, H.-T.; Palit, S.; Tyler, T.; Bingham, C. M.; Zide, J. M.; O'Hara, J. F.; Smith, D. R.; Gossard, A. C.; Averitt, R. D.; Padilla, W. J.; others. *Applied Physics Letters* **2008**, *93*(9), 091117.
- [77] Chen, H.-T.; Padilla, W. J.; Zide, J. M.; Bank, S. R.; Gossard, A. C.; Taylor, A. J.; Averitt, R. D. *Optics letters* **2007**, *32*(12), 1620–1622.
- [78] Chen, H.-T.; Padilla, W. J.; Cich, M. J.; Azad, A. K.; Averitt, R. D.; Taylor, A. J. *Nature photonics* **2009**, *3*(3), 148–151.
- [79] Chen, H.-T.; Padilla, W. J.; Zide, J. M.; Gossard, A. C.; Taylor, A. J.; Averitt, R. D. *Nature* **2006**, *444*(7119), 597.
- [80] Larsen, K.; Austin, D.; Sandall, I.; Davies, D.; Revin, D.; Cockburn, J.; Adawi, A.; Airey, R.; Fry, P.; Hopkinson, M.; others. *Applied Physics Letters* **2012**, *101*(25), 251109.
- [81] Zhao, Q.; Kang, L.; Du, B.; Li, B.; Zhou, J.; Tang, H.; Liang, X.; Zhang, B. *Applied physics letters* **2007**, *90*(1), 011112.

- [82] Shrekenhamer, D.; Chen, W.-C.; Padilla, W. J. *Physical review letters* **2013**, *110*(17), 177403.
- [83] He, X. *Carbon* **2015**, *82*, 229–237.
- [84] Mousavi, S. H.; Khanikaev, A. B.; Shvets, G. *SPIE Newsroom* **2013**.
- [85] Huang, H.; Xia, H.; Xie, W.; Guo, Z.; Li, H.; Xie, D. *Scientific Reports* **2018**, *8*(1), 4183.
- [86] Chen, W.-C.; Bingham, C. M.; Mak, K. M.; Caira, N. W.; Padilla, W. J. *Physical Review B* **2012**, *85*(20), 201104.
- [87] Costa, F.; Genovesi, S.; Monorchio, A. *IEEE Antennas and Wireless Propagation Letters* **2009**, *8*, 1341–1344.
- [88] Rajagopalan, A.; RamRakhyani, A. K.; Schurig, D.; Lazzi, G. *IEEE Transactions on Microwave Theory and Techniques* **2014**, *62*(4), 947–955.
- [89] Orlandi, P.; Morichetti, F.; Strain, M. J.; Sorel, M.; Bassi, P.; Melloni, A. *Journal of Lightwave Technology* **2014**, *32*(5), 897–907.
- [90] Coldren, L. A.; Corzine, S. W.; Mashanovitch, M. L. *Diode lasers and photonic integrated circuits*, Vol. 218; John Wiley & Sons, 2012.
- [91] Liu, N.; Guo, H.; Fu, L.; Kaiser, S.; Schweizer, H.; Giessen, H. *Nature materials* **2008**, *7*(1), 31.

- [92] Chanda, D.; Shigeta, K.; Gupta, S.; Cain, T.; Carlson, A.; Mihi, A.; Baca, A. J.; Bogart, G. R.; Braun, P.; Rogers, J. A. *Nature nanotechnology* **2011**, *6*(7), 402.
- [93] Kwon, B.; Kim, J. H. *Journal of Nanoscience* **2016**, *2016*.
- [94] Koo, N.; Bender, M.; Plachetka, U.; Fuchs, A.; Wahlbrink, T.; Bolten, J.; Kurz, H. *Microelectronic Engineering* **2007**, *84*(5-8), 904–908.
- [95] Lodewijks, K.; Verellen, N.; Van Roy, W.; Moshchalkov, V.; Borghs, G.; Van Dorpe, P. *Applied Physics Letters* **2011**, *98*(9), 091101.
- [96] Burckel, D. B.; Wendt, J. R.; Ten Eyck, G. A.; Ellis, A. R.; Brener, I.; Sinclair, M. B. *Advanced Materials* **2010**, *22*(29), 3171–3175.
- [97] Aoki, K.; Furusawa, K.; Tanaka, T. *Applied Physics Letters* **2012**, *100*(18), 181106.
- [98] Yoon, G.; Kim, I.; Rho, J. *Microelectronic Engineering* **2016**, *163*, 7–20.
- [99] Yao, J.; Liu, Z.; Liu, Y.; Wang, Y.; Sun, C.; Bartal, G.; Stacy, A. M.; Zhang, X. *Science* **2008**, *321*(5891), 930–930.
- [100] Hong, Y. K.; Kim, B. H.; Kim, D. I.; Park, D. H.; Joo, J. *RSC Advances* **2015**, *5*(34), 26872–26877.
- [101] Arnold, C. B.; Piqué, A. *MRS bulletin* **2007**, *32*(1), 9–15.

- [102] Wang, B.; Zhou, J.; Koschny, T.; Soukoulis, C. M. *Applied Physics Letters* **2009**, *94*(15), 151112.
- [103] Wu, C.; Li, H.; Yu, X.; Li, F.; Chen, H.; Chan, C. T. *Physical Review Letters* **2011**, *107*(17), 177401.
- [104] Gansel, J. K.; Thiel, M.; Rill, M. S.; Decker, M.; Bade, K.; Saile, V.; von Freymann, G.; Linden, S.; Wegener, M. *Science* **2009**, *325*(5947), 1513–1515.
- [105] Wuestner, S.; Pusch, A.; Tsakmakidis, K. L.; Hamm, J. M.; Hess, O. *Physical review letters* **2010**, *105*(12), 127401.
- [106] Plum, E.; Fedotov, V.; Kuo, P.; Tsai, D.; Zheludev, N. *Optics express* **2009**, *17*(10), 8548–8551.
- [107] Sadatgol, M.; Özdemir, Ş. K.; Yang, L.; Güney, D. Ö. *Physical review letters* **2015**, *115*(3), 035502.
- [108] Adams, W.; Sadatgol, M.; Zhang, X.; Güney, D. Ö. *New Journal of Physics* **2016**, *18*(12), 125004.
- [109] Kolb, P.; Salter, T.; McGee, J.; Drew, H.; Padilla, W. *Journal of Applied Physics* **2011**, *110*(5), 054906.
- [110] He, P.; Gao, J.; Marinis, C.; Parimi, P.; Vittoria, C.; Harris, V. *Applied Physics Letters* **2008**, *93*(19), 193505.

- [111] Wiltshire, M.; Pendry, J.; Hajnal, J. *Journal of Physics: Condensed Matter* **2006**, *18*(22), L315.
- [112] Erentok, A.; Ziolkowski, R. W.; Nielsen, J.; Greigor, R.; Parazzoli, C.; Tanielian, M.; Cummer, S. A.; Popa, B.-I.; Hand, T.; Vier, D.; others. *Journal of Applied Physics* **2008**, *104*(3), 034901.
- [113] Zheludev, N. I.; Kivshar, Y. S. *Nature materials* **2012**, *11*(11), 917–924.
- [114] Amemiya, T.; Kanazawa, T.; Yamasaki, S.; Arai, S. *Materials* **2017**, *10*(9), 1037.
- [115] Rill, M. S.; Plet, C.; Thiel, M.; Staude, I.; Von Freymann, G.; Linden, S.; Wegener, M. *Nature materials* **2008**, *7*(7).
- [116] Kawata, S.; Sun, H.-B.; Tanaka, T.; Takada, K. *Nature* **2001**, *412*(6848), 697–698.
- [117] Formanek, F.; Takeyasu, N.; Tanaka, T.; Chiyoda, K.; Ishikawa, A.; Kawata, S. *Optics express* **2006**, *14*(2), 800–809.
- [118] Hell, S. W.; Wichmann, J. *Optics letters* **1994**, *19*(11), 780–782.
- [119] Klar, T. A.; Jakobs, S.; Dyba, M.; Egner, A.; Hell, S. W. *Proceedings of the National Academy of Sciences* **2000**, *97*(15), 8206–8210.
- [120] Hell, S. W. *Physics Letters A* **2004**, *326*(1), 140–145.

- [121] Fischer, J.; Ergin, T.; Wegener, M. *Optics letters* **2011**, *36*(11), 2059–2061.
- [122] Thiel, M.; Ott, J.; Radke, A.; Kaschke, J.; Wegener, M. *Optics letters* **2013**, *38*(20), 4252–4255.
- [123] Fischer, J.; Thiel, M.; Wegener, M. *IEEE Spectrum* **2014**, *51*(2), 34–58.
- [124] Cortes, C.; Newman, W.; Molesky, S.; Jacob, Z. *Journal of Optics* **2012**, *14*(6), 063001.
- [125] Poddubny, A.; Iorsh, I.; Belov, P.; Kivshar, Y. *Nature Photonics* **2013**, *7*(12), 948–957.
- [126] Wood, B.; Pendry, J.; Tsai, D. *Physical Review B* **2006**, *74*(11), 115116.
- [127] Rho, J.; Ye, Z.; Xiong, Y.; Yin, X.; Liu, Z.; Choi, H.; Bartal, G.; Zhang, X. *Nature communications* **2010**, *1*, 143.
- [128] Lu, D.; Liu, Z. *Nature communications* **2012**, *3*, 1205.
- [129] Sun, J.; Shalaev, M. I.; Litchinitser, N. M. *Nature communications* **2015**, *6*.
- [130] Noginov, M.; Li, H.; Barnakov, Y. A.; Dryden, D.; Nataraj, G.; Zhu, G.; Bonner, C.; Mayy, M.; Jacob, Z.; Narimanov, E. *Optics letters* **2010**, *35*(11), 1863–1865.
- [131] Shalaginov, M. Y.; Ishii, S.; Liu, J.; Liu, J.; Irudayaraj, J.; Lagutchev, A.; Kildishev, A.; Shalaev, V. *Applied Physics Letters* **2013**, *102*(17), 173114.

- [132] Ferrari, L.; Lu, D.; Lepage, D.; Liu, Z. *Optics express* **2014**, *22*(4), 4301–4306.
- [133] Guo, Y.; Cortes, C. L.; Molesky, S.; Jacob, Z. *Applied Physics Letters* **2012**, *101*(13), 131106.
- [134] Narimanov, E. E.; Li, H.; Barnakov, Y. A.; Tumkur, T.; Noginov, M. *Optics express* **2013**, *21*(12), 14956–14961.
- [135] Valentine, J.; Zhang, S.; Zentgraf, T.; Ulin-Avila, E.; Genov, D. A.; Bartal, G.; Zhang, X. *nature* **2008**, *455*(7211), 376–379.
- [136] Kruk, S. S.; Powell, D. A.; Minovich, A.; Neshev, D. N.; Kivshar, Y. S. *Optics express* **2012**, *20*(14), 15100–15105.
- [137] Andryieuski, A.; Lavrinenko, A. V.; Chigrin, D. N. *Physical Review B* **2012**, *86*(12), 121108.
- [138] Smith, D.; Schultz, S.; Markoš, P.; Soukoulis, C. *Physical Review B* **2002**, *65*(19), 195104.
- [139] Güney, D. Ö.; Koschny, T.; Soukoulis, C. M. *Physical Review B* **2011**, *83*(4), 045107.
- [140] Güney, D. Ö.; Koschny, T.; Soukoulis, C. M. *Physical Review B* **2009**, *80*(12), 125129.
- [141] Zhang, S.; Fan, W.; Malloy, K.; Brueck, S.; Panoiu, N.; Osgood, R. *Optics Express* **2005**, *13*(13), 4922–4930.

- [142] Menzel, C.; Rockstuhl, C.; Paul, T.; Lederer, F.; Pertsch, T. *Physical Review B* **2008**, *77*(19), 195328.
- [143] Xiong, X.; Jiang, S.-C.; Hu, Y.-H.; Peng, R.-W.; Wang, M. *Advanced Materials* **2013**, *25*(29), 3994–4000.
- [144] Vora, K.; Kang, S.; Shukla, S.; Mazur, E. *Applied Physics Letters* **2012**, *100*(6), 063120.
- [145] Kang, S.; Vora, K.; Mazur, E. *Nanotechnology* **2015**, *26*(12), 121001.
- [146] Zhou, J.; Koschny, T.; Kafesaki, M.; Economou, E.; Pendry, J.; Soukoulis, C. *Physical review letters* **2005**, *95*(22), 223902.
- [147] Koschny, T.; Markoš, P.; Economou, E. N.; Smith, D.; Vier, D.; Soukoulis, C. *Physical Review B* **2005**, *71*(24), 245105.
- [148] Zhen, L.; Jiang, J.; Shao, W.; Xu, C. *Applied physics letters* **2007**, *90*(14), 142907.
- [149] Koschny, T.; Markoš, P.; Smith, D.; Soukoulis, C. *Physical Review E* **2003**, *68*(6), 065602.
- [150] Ludwig, A.; Webb, K. J. *Physical Review B* **2010**, *81*(11), 113103.
- [151] Alù, A. *Physical Review B* **2011**, *83*(8), 081102.
- [152] Alù, A. *Physical Review B* **2011**, *84*(7), 075153.

- [153] Khoo, I. C. *Progress in Quantum Electronics* **2014**, *38*(2), 77–117.
- [154] Ptasinski, J.; Khoo, I.-C.; Fainman, Y. *Optics letters* **2014**, *39*(18), 5435–5438.
- [155] Kaschke, J.; Wegener, M. *Optics letters* **2015**, *40*(17), 3986–3989.
- [156] Optical networks: A practical perspective (2010). Ramaswami, R.; Sivarajan, K.; Sasaki, G.
- [157] Lukin, M.; Imamoglu, A. *Physical Review Letters* **2000**, *84*(7), 1419.
- [158] Leuenberger, M. N.; Flatté, M. E.; Awschalom, D. D. *Physical review letters* **2005**, *94*(10), 107401.
- [159] al Farooqui, M. A.; Breeland, J.; Aslam, M. I.; Sadatgol, M.; Özdemir, Ş. K.; Tame, M.; Yang, L.; Güney, D. Ö. *Optics express* **2015**, *23*(14), 17941–17954.
- [160] Asano, M.; Bechu, M.; Tame, M.; Özdemir, Ş. K.; Ikuta, R.; Güney, D. Ö.; Yamamoto, T.; Yang, L.; Wegener, M.; Imoto, N. *Scientific reports* **2015**, *5*, 18313.
- [161] Uriri, S.; Tashima, T.; Zhang, X.; Asano, M.; Bechu, M.; Güney, D.; Yamamoto, T.; Özdemir, Ş.; Wegener, M.; Tame, M. *Physical Review A* **2018**, *97*(5), 053810.
- [162] Kasapi, A.; Jain, M.; Yin, G.; Harris, S. E. *Physical review letters* **1995**, *74*(13), 2447.

- [163] Lukin, M.; Imamoglu, A. *Nature* **2001**, *413*(6853), 273.
- [164] Yanik, M. F.; Fan, S. *Physical review letters* **2004**, *92*(8), 083901.
- [165] Vlasov, Y. A.; O'boyle, M.; Hamann, H. F.; McNab, S. J. *Nature* **2005**, *438*(7064), 65–69.
- [166] Bigelow, M. S.; Lepeshkin, N. N.; Boyd, R. W. *Science* **2003**, *301*(5630), 200–202.
- [167] Camacho, R. M.; Pack, M. V.; Howell, J. C.; Schweinsberg, A.; Boyd, R. W. *Physical review letters* **2007**, *98*(15), 153601.
- [168] Okawachi, Y.; Bigelow, M. S.; Sharping, J. E.; Zhu, Z.; Schweinsberg, A.; Gauthier, D. J.; Boyd, R. W.; Gaeta, A. L. *Physical review letters* **2005**, *94*(15), 153902.
- [169] Woodley, J.; Mojahedi, M. *Physical Review E* **2004**, *70*(4), 046603.
- [170] Dolling, G.; Enkrich, C.; Wegener, M.; Soukoulis, C. M.; Linden, S. *Science* **2006**, *312*(5775), 892–894.
- [171] Aslam, M. I.; Güney, D. Ö. *arXiv preprint arXiv:1212.6681* **2012**.
- [172] Shadrivov, I. V.; Sukhorukov, A. A.; Kivshar, Y. S. *Physical Review E* **2003**, *67*(5), 057602.
- [173] Tsakmakidis, K. L.; Klaedtke, A.; Aryal, D. P.; Jamois, C.; Hess, O. *Applied physics letters* **2006**, *89*(20), 201103.

- [174] Tsakmakidis, K. L.; Boardman, A. D.; Hess, O. *Nature* **2007**, *450*(7168), 397–401.
- [175] Kim, K.-Y. *Japanese Journal of Applied Physics* **2008**, *47*(6R), 4843.
- [176] Jiang, T.; Zhao, J.; Feng, Y. *Optics express* **2009**, *17*(1), 170–177.
- [177] Berman, P. *Physical Review E* **2002**, *66*(6), 067603.
- [178] SHEN, L.; JIA-CHENG, Q.; WANG, Z. In *Progress in Electromagnetics Research Symposium Proceedings, Suzhou, China*, pages 1043–1048, 2011.
- [179] He, S.; He, Y.; Jin, Y. *Scientific reports* **2012**, *2*, 583.
- [180] Huang, T.-Y.; Yang, T.-C.; Yen, T.-J. *Applied Physics Letters* **2013**, *102*(11), 111102.
- [181] Hu, H.; Ji, D.; Zeng, X.; Liu, K.; Gan, Q. In *CLEO: QELS-Fundamental Science*, pages QTu2A–4. Optical Society of America, 2013.
- [182] Güney, D. Ö.; Koschny, T.; Kafesaki, M.; Soukoulis, C. M. *Optics letters* **2009**, *34*(4), 506–508.
- [183] Ruppin, R. *Journal of Physics: Condensed Matter* **2001**, *13*(9), 1811.
- [184] Grigorenko, A. *Optics letters* **2006**, *31*(16), 2483–2485.
- [185] Shalaev, V. M.; Cai, W.; Chettiar, U. K.; Yuan, H.-K.; Sarychev, A. K.; Drachev, V. P.; Kildishev, A. V. *Optics letters* **2005**, *30*(24), 3356–3358.

- [186] Vora, K. L. *Three-dimensional nanofabrication of silver structures in polymer with direct laser writing*; Harvard University, 2014.
- [187] Abbe, E. *Archiv für mikroskopische Anatomie* **1873**, *9*(1), 413–418.
- [188] Fang, N.; Lee, H.; Sun, C.; Zhang, X. *Science* **2005**, *308*(5721), 534–537.
- [189] Taubner, T.; Korobkin, D.; Urzhumov, Y.; Shvets, G.; Hillenbrand, R. *Science* **2006**, *313*(5793), 1595–1595.
- [190] Zhang, X.; Liu, Z. *Nature materials* **2008**, *7*(6), 435–441.
- [191] Xu, T.; Agrawal, A.; Abashin, M.; Chau, K. J.; Lezec, H. J. *Nature* **2013**, *497*(7450), 470–474.
- [192] Maas, R.; van de Groep, J.; Polman, A. *Optica* **2016**, *3*(6), 592–596.
- [193] Smolyaninov, I. I.; Hung, Y.-J.; Davis, C. C. *science* **2007**, *315*(5819), 1699–1701.
- [194] Smolyaninov, I. I.; Hung, Y.-J.; Davis, C. C. *Physical Review B* **2007**, *76*(20), 205424.
- [195] Yan, B.; Wang, Z.; Parker, A. L.; Lai, Y.-k.; Thomas, P. J.; Yue, L.; Monks, J. N. *Applied Optics* **2017**, *56*(11), 3142–3147.
- [196] Wang, Z. *Nanoscience* **2016**, *3*, 193–210.
- [197] Kildishev, A. V.; Narimanov, E. E. *Optics letters* **2007**, *32*(23), 3432–3434.

- [198] Balanis, C. A. *Advanced engineering electromagnetics*; John Wiley & Sons, 1999.
- [199] Johnson, P. B.; Christy, R.-W. *Physical review B* **1972**, *6*(12), 4370.
- [200] Palik, E. D. *Handbook of optical constants of solids*, Vol. 3; Academic press, 1998.
- [201] Choi, M.; Lee, S. H.; Kim, Y.; Kang, S. B.; Shin, J.; Kwak, M. H.; Kang, K.-Y.; Lee, Y.-H.; Park, N.; Min, B. *Nature* **2011**, *470*(7334), 369–373.
- [202] Economou, E.; Koschny, T.; Soukoulis, C. *Physical Review B* **2008**, *77*(9), 092401.
- [203] Penciu, R.; Aydin, K.; Kafesaki, M.; Koschny, T.; Ozbay, E.; Economou, E.; Soukoulis, C. *Optics express* **2008**, *16*(22), 18131–18144.
- [204] Śmigaj, W.; Gralak, B. *Physical Review B* **2008**, *77*(23), 235445.
- [205] Gang, Q.; Jia-Fu, W.; Ming-Bao, Y.; Wei, C.; Hong-Ya, C.; Yong-Feng, L. *Chinese Physics B* **2013**, *22*(8), 087302.
- [206] Wolff, L. B. *JOSA A* **1994**, *11*(11), 2935–2945.
- [207] McCormick, F. B.; Tooley, F.; Cloonan, T. J.; Brubaker, J.; Lentine, A. L.; Morrison, R. L.; Hinterlong, S.; Herron, M.; Walker, S.; Sasian, J. *Applied Optics* **1992**, *31*(26), 5431–5446.

- [208] Ojima, M.; Saito, A.; Kaku, T.; Ito, M.; Tsunoda, Y.; Takayama, S.; Sugita, Y. *Applied optics* **1986**, *25*(4), 483–489.
- [209] Chen, J.; Altepeter, J. B.; Medic, M.; Lee, K. F.; Gokden, B.; Hadfield, R. H.; Nam, S. W.; Kumar, P. *Physical review letters* **2008**, *100*(13), 133603.
- [210] Quantum computation and quantum information. Nielsen, M. A.; Chuang, I. **2002**.
- [211] Zheng, J.; Zhou, C.; Feng, J.; Cao, H.; Lu, P. *Journal of Optics A: Pure and Applied Optics* **2008**, *11*(1), 015710.
- [212] Liu, T.; Zakharian, A. R.; Fallahi, M.; Moloney, J. V.; Mansuripur, M. *IEEE photonics technology letters* **2005**, *17*(7), 1435–1437.
- [213] Lalanne, P.; Hazart, J.; Chavel, P.; Cambril, E.; Launois, H. *Journal of Optics A: Pure and Applied Optics* **1999**, *1*(2), 215.
- [214] Adams, W.; Ghoshroy, A.; Güney, D. Ö. *JOSA B* **2017**, *34*(10), 2161–2168.
- [215] Ghoshroy, A.; Adams, W.; Zhang, X.; Güney, D. Ö. *JOSA B* **2017**, *34*(7), 1478–1488.
- [216] Ghoshroy, A.; Zhang, X.; Adams, W.; Guney, D. O. *arXiv preprint arXiv:1710.07166* **2017**.
- [217] Ghoshroy, A.; Adams, W.; Zhang, X.; Güney, D. Ö. *Optics letters* **2018**, *43*(8), 1810–1813.

[218] Adams, W.; Ghoshroy, A.; Güney, D. *ACS Photonics* **2018**.

Appendix A

Letters of permission

PIER

Progress In Electromagnetics Research

ISSN: 1070-4698, E-ISSN: 1559-8985

SITE UNDER CONSTRUCTION. PIER IS IN THE MIDDLE OF MOVING TO A NEW SERVER

[Home](#) | [Search](#) | [Notification](#) | [Authors](#) | [Submission](#) | [PIERS Home](#) | [EM Academy](#)

Quick Article Search:

PIER Journals
[PIER](#) [PIER B](#)
[PIER C](#) [PIER M](#)
[PIER Letters](#)

PIER Online
[PIER 163 \[2018\]](#)
[PIER 162 \[2018\]](#)
[PIER 161 \[2018\]](#)
[PIER 160 \[2017\]](#)
[PIER 159 \[2017\]](#)
[PIER 158 \[2017\]](#)
[PIER 157 \[2016\]](#)
[PIER 156 \[2016\]](#)
[PIER 155 \[2016\]](#)
[PIER 154 \[2015\]](#)
[PIER 153 \[2015\]](#)
[PIER 152 \[2015\]](#)
[PIER 151 \[2015\]](#)
[PIER 150 \[2015\]](#)
[PIER 149 \[2014\]](#)

Founding Editor in Chief: [Jin Au Kong](#)

Progress In Electromagnetics Research (PIER) publishes peer-reviewed original and comprehensive articles on all aspects of electromagnetic theory and applications. This is an open access, on-line journal PIER (E-ISSN 1559-8985). It has been first published as a monograph series on Electromagnetic Waves (ISSN 1070-4698) in 1989. It is freely available to all readers via the Internet.

PIER is a non-profit organization.

WWW.JPIER.ORG
Contact Email: work@jpieer.org

Authors are strongly advised to visit [Author Guidelines and Publication Fee](#) before submission to understand the PIER Journals process.

Authors are solely responsible for the factual accuracy and originality of their articles, and all articles are understood to have received clearance(s) for publication. Manuscripts submitted to PIER Journals must not have been submitted simultaneously to other journals. Authors found submitting manuscripts simultaneously to other journals will be suspended for 1 year from further submission.

how to get permission to reprint the published papers in JOSA B

3 messages

Xu Zhang [REDACTED]
To: copyright@osa.org

Fri, Oct 6, 2017 at 2:52 PM

Dear officer,

I am a PhD student in Michigan Technological University, and I published 2 papers on JOSA B during my PhD study. These two papers are

1. Xu Zhang, Wyatt Adams, and Durdu Ö. Güney, "Analytical description of inverse filter emulating the plasmon injection loss compensation scheme and implementation for ultrahigh-resolution hyperlens," J. Opt. Soc. Am. B 34, 1310-1318 (2017)
2. Xu Zhang, Sanjoy Debnath, and Durdu Ö. Güney, "Hyperbolic metamaterial feasible for fabrication with direct laser writing processes," J. Opt. Soc. Am. B 32, 1013-1021 (2015)

Now I plan to graduate and prepare my dissertation. I wonder if I could reprint these two papers as two chapters in my dissertation, and could you please tell me the way to get permissions?

Thank you for your help and I am looking forward to your reply.

Best,
Xu Zhang

pubscopyright <copyright@osa.org>
To: Xu Zhang [REDACTED] pubscopyright <copyright@osa.org>

Mon, Oct 9, 2017 at 4:48 PM

Dear Xu Zhang,

Thank you for contacting The Optical Society.

For the use of [1] Xu Zhang, Wyatt Adams, and Durdu Ö. Güney, "Analytical description of inverse filter emulating the plasmon injection loss compensation scheme and implementation for ultrahigh-resolution hyperlens," J. Opt. Soc. Am. B 34, 1310-1318 (2017) and [2] Xu Zhang, Sanjoy Debnath, and Durdu Ö. Güney, "Hyperbolic metamaterial feasible for fabrication with direct laser writing processes," J. Opt. Soc. Am. B 32, 1013-1021 (2015):

As long as the copyrighted material is included within the body, section or chapter, of the thesis, and is not posted separate from the thesis, OSA considers your requested use of its copyrighted materials to be permissible within the author rights granted in the Copyright Transfer Agreement submitted by the requester on acceptance for publication of his/her manuscript. It is requested that the **Author Accepted (or preprint)** version be the version included within the thesis and that a complete citation of the original material be included in any publication. This permission assumes that the material was not reproduced from another source when published in the original publication.

The **Author Accepted** version is the preprint version of the article that was accepted for publication but not yet prepared and/or formatted by The Optical Society or its vendors.

While your publisher should be able to provide additional guidance, OSA prefers the below citation formats:

For citations in figure captions:

[Reprinted/Adapted] with permission from ref [x], [Publisher]. (with full citation in reference list)

For images without captions:

Journal Vol. #, first page (year published)

An example: J. Opt. Soc. Am. B 34, 1310 (2017)

Let me know if you have any questions.

Best Wishes,

██████████

██████████

October 9, 2017

Authorized Agent, The Optical Society

get permission to reprint the figure (metamaterial ring structure) in your dissertation

3 messages

Xu Zhang ██████████
To: ██████████

Mon, Dec 18, 2017 at 12:04 PM

Dear Dr. Kevin Vora,

Sorry to bother you. I am a PhD student working with Dr. Durdu Guney in Michigan Technological University. We collaborated on design and fabrication of the metamaterial ring structure around 2013. Dr. Guney and I provided the designed structure and you fabricated them. The work was shown in your PhD dissertation, Chapter 6, section 6.3.

Now I am preparing my dissertation. I wonder if I can reprint figure 54 and 55 in section 6.3 of your dissertation to use it in my dissertation.

Thanks for your help and I am looking forward to your reply.

Best,
Xu Zhang

Kevin ██████████
To: Xu Zhang ██████████

Mon, Dec 18, 2017 at 8:06 PM

Hi Xu,

Sure!

Best,
Kevin

Appendix B

MATLAB code

B.1 Extending inverse filter loss compensation technique to hyperlens

```
%%This code is for inverse filter loss compensation ←  
    technique in cylindrical coordinate system  
  
close all  
  
clear all  
  
clc
```

```

c=2.99792458e8; % speed of light
freq=c/(365e-9); % working frequency
r_object=240e-9; % radius of object plane
r_image=800e-9; % radius of image plane
phi_step=pi/1000;
phi=-0.5*pi:phi_step:1.5*pi; % FFT requires 2*pi*r arc ←
    length. In the simulation, we can only define phi from←
    0 to pi.

%% make large object and image planes
image_plane=xlsread('image plane.csv'); % complex ←
    magnetic field obtained in image plane
real_i_1=image_plane(:,3)'; % real part of obtained ←
    magnetic field
real_i_2=zeros(1,length(phi_i_2));
real_i_3=zeros(1,length(phi_i_3));
real_i=[real_i_2,real_i_1,real_i_3]; % final real part ←
    of magnetic field after image plane extension
imag_i_1=image_plane(:,4)'; % imaginary part of obtained←
    magnetic field
imag_i_2=zeros(1,length(phi_i_2));

```

```

imag_i_3=zeros(1,length(phi_i_3));
imag_i=[imag_i_2,imag_i_1,imag_i_3]; % final imaginary ←
    part of magnetic field after image plane extension

object_plane=xlsread('object plane.csv'); % real ←
    magnetic field defined in object plane
real_o_1=object_plane(:,3)'; % real part of defined ←
    magnetic field
real_o_2=zeros(1,length(phi_o_2));
real_o_3=zeros(1,length(phi_o_3));
real_o=[real_o_2,real_o_1,real_o_3]; % final defined ←
    magnetic field after object plane extension

object_H=real_o;
image_H=real_i-j*imag_i; % minus sign comes from Comsol

figure(1); % plot extended object and raw image
hold on;
plot(phi,abs(image_H),'r','linewidth',4);
plot(phi,abs(object_H),'b','linewidth',4);
xlabel('\phi','fontsize',20);

```

```

ylabel('H','fontsize',20);
legend('raw image','original object',1);

%% transfer function calculation
tff=xlsread('transfer function H field.csv'); % obtained←
    from different modes of cylindrical waves
m=tff(:,1); % m is cylindrical wave mode number
object_real=tff(:,3); % exp(im(phi)) defined at object ←
    plane
object_imag=tff(:,4); % imaginary part is 0
image_real=tff(:,5);
image_imag=tff(:,6);
object_m=object_real-j*object_imag;
image_m=image_real-j*image_imag;
tf=image_m./object_m; % transfer function
filter=1./tf; % inverse filter

figure(2); % corresponding to Figure 3.3 (a) in Chapter ←
    3
hold on;
plot(m,abs(tf),'b','linewidth',2);

```

```

plot(m,abs(filter),'g','linewidth',2);
xlabel('m','fontsize',20);
ylabel('T_{amplitude}','fontsize',20);
legend('tf','filter',1);
set(gca,'YScale','log');
figure(3); %corresponding to Figure 3.3 (b) in Chapter 3
hold on;
plot(m,angle(tf),'B','linewidth',2);
plot(m,angle(filter),'g','linewidth',2);
xlabel('m','fontsize',20);
ylabel('T_{phase}','fontsize',20);
legend('tf','filter',1);

%% loss compensation procedure
N_fft=length(image_H);
m=0:(N_fft-1);
fft_image_H=fft(image_H,N_fft); % Fourier transform of ↔
    raw image
fft_object_H=fft(object_H,N_fft); % Fourier transform of ↔
    original object
m_max=36; % cut off spatial frequency

```

```

m_int=m(1:m_max+1);

filter_truncated=filter(1:m_max+1);

fft_object_H_truncated=fft_object_H(1:m_max+1);

fft_image_H_truncated=fft_image_H(1:m_max+1);

fft_image_H_compensated=fft_image_H_truncated.*↵
    filter_truncated;

figure(4); % corresponding to Figure 3.4 (a) in Chapter ↵
    3

hold on;

plot(m_int,abs(fft_object_H_truncated),'b');

plot(m_int,abs(fft_image_H_truncated),'r');

plot(m_int,abs(fft_image_H_compensated),'g');

legend('truncated object','raw image','compensated image↵
    ',1);

set(gca,'fontsize',18,'fontWeight','bold','linewidth',2)↵
    ;

xlabel('m','fontsize',24,'fontWeight','bold');

ylabel('Amplitude','fontsize',24,'fontWeight','bold');

set(gca,'YScale','log');

```

```

figure(5); % corresponding to Figure 3.4 (b) in Chapter ←
    3

hold on;

plot(m_int, angle(fft_object_H_truncated), 'b');
plot(m_int, angle(fft_image_H_truncated), 'r');
plot(m_int, angle(fft_image_H_compensated), 'g');

legend('truncated object', 'raw image', 'compensated image←
    ', 1);

set(gca, 'fontsize', 18, 'fontWeight', 'bold', 'linewidth', 2)←
    ;

xlabel('m', 'fontsize', 24, 'fontWeight', 'bold');
ylabel('Phase', 'fontsize', 24, 'fontWeight', 'bold');

%% inverse Fourier transform to spatial domain

image_H_compensated=ifft(fft_image_H_compensated, N_fft);
object_H_truncated_recovered=ifft(fft_object_H_truncated←
    , N_fft);

object_H_full_recovered=ifft(fft_object_H, N_fft);
image_H_full_recovered=ifft(fft_image_H, N_fft);

```

```

figure(6); % corresponding to Figure 3.4 (c) in Chapter ←
    3

hold on;

plot(phi,abs(object_H_truncated_recovered),'k');

plot(phi,abs(image_H_full_recovered),'r');

plot(phi,abs(image_H_compensated),'g');

plot(phi,abs(object_H_full_recovered),'b');

legend('truncated object','raw image','compensated image←
    ','original object',1);

set(gca,'fontsize',18,'linewidth',1);

xlabel('\theta (rad)','fontsize',20);

ylabel('amplitude','fontsize',20);

```

B.2 Equifrequency plot

```

%%This code is for calculating Equifrequency contour

clear all

close all

clc

```

```

c=2.99792458e8; % speed of light

d=2400e-9; % unit cell size

f=xlsread('.xls'); % The excel file contains the s ←
    parameter data (s11 & s21) obtained from the incident ←
    waves under special angle.

s11_mag=f(:,2);
s11_arg=f(:,3);
s21_mag=f(:,4);
s21_arg=f(:,5);

s11=s11_mag.*exp(-i.*s11_arg.*pi./180); % reflection ←
    coefficient

s21=s21_mag.*exp(-i.*s21_arg.*pi./180); % transmission ←
    coefficient

%% calculating kz at particular frequency

r=s11(609);

t=s21(609);

f=132.16e+12;

k0=(2*pi/c)*f;

theta=1*pi/180;

```

```

phi=p*pi/180;
kx=k0*sin(theta)*cos(phi);
ky=k0*sin(phi);

h=(1/cos(phi))*d/cos(theta); % h is the length of the ←
    metamaterial in the propagation direction.

for m=-1:1 % m is determined by continuity of Re(k)
    k=(1/h)*acos((1-r^2+t^2)/(2*t))+2*pi*m*(1/h);
    if imag(k)<0;
        kz=-k;
    else
        kz=k;
    end
end

figure(1); % corresponding to Figure 2.6 in Chapter 2, 2↔
    D calculation, phi=0.
plot(real(kz)/k0,kx/k0,-real(kz)/k0,-kx/k0,real(kz)/k0,-↔
    kx/k0,-real(kz)/k0,kx/k0);
xlabel('k_z/k_0','fontsize',20);

```

```

ylabel('k_x/k_0','fontsize',20);

set(gca,'fontsize',20,'linewidth',1);

%% plot 3D surface

data=xlsread('30nm 3d surface plot'); % This excel is kx↔
    , ky and kz data calculating from above

x=data(:,1);
y=data(:,2);
z=data(:,4);
a=data(:,6);
b=data(:,7);
c=data(:,9);

[qx,qy] = meshgrid(linspace(min(x),max(x)),linspace(min(↔
    y),max(y)));

qz= griddata(x,y,z,qx,qy,'linear');

for i=1:100

    for j=1:100

        if 0.95<qx(i,j)^2+qy(i,j)^2 && qx(i,j)^2+qy(i,j)↔
            ^2<1.05 && isnan(qz(i,j))==1

```

```

        qz(i,j)=0;
    end
end
end

end

surf(qx,qy,qz,'Facecolor','red','EdgeColor','none')

hold on

[qa,qb] = meshgrid(linspace(min(a),max(a)),linspace(min(↵
    b),max(b)));
qc= griddata(a,b,c,qa,qb,'linear');
for i=1:100
    for j=1:100
        if 0.95<qa(i,j)^2+qb(i,j)^2 && qa(i,j)^2+qb(i,j)↵
            ^2<1.05 && isnan(qc(i,j))==1
            qc(i,j)=0;
        end
    end
end
end

surf(qa,qb,qc,'FaceColor','red','EdgeColor','none')

```

```
hold on

%% plot one sphere to compare with the 3D surface

[X,Y,Z]=sphere;

mesh(X,Y,Z);

line(X(:,,:),Y(:,,:),Z(:,:),'Color','k','LineWidth',1);

hidden off

set(gcf,'colormap',[0 0 0])
```